DIRECT COMPARISON OF THE MAGNETIC PROPERTIES OF $Gd_{0.7}Sr_{0.3}MnO_3$ NANOPARTICLES WITH BULK COUNTERPARTS

A Dissertation Submitted to the Department of Physics, Bangladesh University of Engineering & Technology, Dhaka in Partial Fulfillment of Requirement for the Degree of Master of Philosophy in Physics
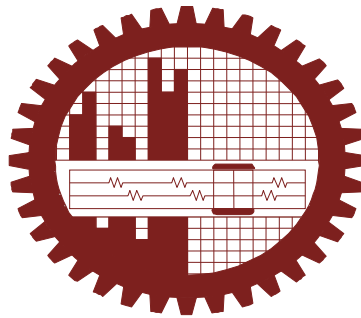
SUBMITTED

By

MOHAMMAD ASHRAFUL ISLAM

EXAMINATION ROLL NO. : 0412143021F

SESSION   : April 2012

DEPARTMENT OF PHYSICS

BANGLADESH UNIVERSITY OF ENGINEERING & TECHNOLOGY

DHAKA 1000, BANGLADESH

CANDIDATE'S DECLARATION

It is hereby declared that this thesis or any part of it has not been submitted elsewhere for the award of any degree or diploma.

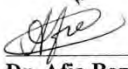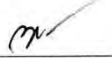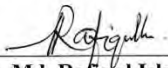————————————————

MOHAMMAD ASHRAFUL ISLAM

BANGLADESH UNIVERSITY OF ENGINEERING & TECHNOLOGY (BUET), DHAKA
DEPARTMENT OF PHYSICS

CERTIFICATION OF THESIS

The thesis titled **"DIRECT COMPARISON OF THE MAGNETIC PROPERTIES OF $Gd_{0.7}Sr_{0.3}MnO_3$ NANOPARTICLES WITH BULK COUNTERPARTS"** submitted by **Mohammad Ashraful Islam**, Roll No-0412143021F, Registration No-0412143021F, Session: April-2012, has been accepted as satisfactory in partial fulfillment of the requirement for the degree of **Master of Philosophy** (M. Phil.) in Physics on 21 November, **2015**.

BOARD OF EXAMINERS

1.

Dr. Mohammed Abdul Basith
Associate Professor
Department of Physics, BUET, Dhaka.

Chairman
(Supervisor)

2.

Dr. Afia Begum
Professor & Head
Department of Physics, BUET, Dhaka.

Member
(Ex-Officio)

3.

Dr. Md. Abu Hashan Bhuiyan
Professor
Department of Physics, BUET, Dhaka.

Member

4. **Dr. Md. Rafiqul Islam**
Professor
Department of Physics
University of Chittagong, Chittagong.

Member
(External)

DEDICATED TO
MY
BELOVED PARENTS

ACKNOWLEDGEMENTS

ABSTRACT

A simple route to prepare $Gd_{0.7}Sr_{0.3}MnO_3$ nanoparticles by ultrasonication of their bulk powder materials was presented. The $Gd_{0.7}Sr_{0.3}MnO_3$ nanoparticles were also prepared by high energy ball milling technique. The transmission electron microscopic imaging demonstrated the formation of nanoparticles with average size varied from 20-40 nm and 100-150 nm, respectively by using ultrasonication and ball milling techniques. The bulk materials as well as nanoparticles synthesized by ultrasonication technique exhibited a paramagnetic to spin-glass transition at 35-40 K. On the contrary, nanoparticles synthesized by ball milling technique did not show any phase transition, however, an upturn of magnetization was observed at low temperature. A drastic change in the magnetic properties of ball milled $Gd_{0.7}Sr_{0.3}MnO_3$ nanoparticles than that of ultrasonically prepared nanoparticles and their corresponding bulk materials was observed. The degradation of the magnetic properties in ball milled nanoparticles may be associated with the contamination, amorphization and formation of a nonmagnetic layer around the surface of the these nanoparticles. The outcome of this investigation demonstrated the potentially of ultrasonication technique as a physical route to prepare rare-earth based manganite nanoparticles.

CONTENTS

CHAPTER 1

INTRODUCTION

CHAPTER 2

BACKGROUND

CHAPTER 3

SAMPLE PREPARATION AND EXPERIMENTAL TECHNIQUES

CHAPTER 4
RESULTS AND DISCUSSION

CHAPTER 5
CONCLUSIONS

LIST OF FIGURES

LIST OF TABLES

CHAPTER 1

INTRODUCTION

1.1 Introduction

Magnetic properties of mixed valence perovskite manganites $R_{1-x}A_xMnO_3$ (R = La, Gd, Pr, Nd, Sm etc and A = Sr, Ba and Ca) at the nanometer scale are currently the focus of intense investigations due to their interesting physical properties as well as potential technological applications [1-4]. When the size of the magnetic particles is reduced to a few tens of nanometer, they exhibit fascinating magnetic and electronic properties that are significantly different from their bulk counterparts [1, 5-8]. In these manganite systems, the novel magnetic properties like Colossal Magnetoresistance (CMR) phenomenon [9] are obtained around transition temperatures e.g. ferromagnetic to paramagnetic transition (T_c) [10]. However, the transition temperatures e.g. T_c values for the same material system were found to vary with particle size by different research groups [10-12]. The conflicting results might be due to the influence of fabrication process as well as different oxygen content of manganites [1]. The fabrication techniques used for the preparation of manganites can influence the intrinsic properties of the sample due to very small variations resulting in the stoichiometry, the Mn-O-Mn bond angle and Mn-O bond length [1, 9]. Notably, the available chemical methods have had limited success in the synthesis of hard magnetic nanoparticles [4, 13] with reduced particle size(<100 nm) and a narrow size distribution. Therefore, the perovskite manganite nanoparticles of various compositions were synthesized directly from bulk powder using ball milling technique [12, 14]. The longer milling time produced successfully nanoparticles from a few nanometers to several ten nanometers [12], however the magnetic properties of the fine particles were found to degrade. Due to the high energy ball milling the defects and surface roughness of $La_{0.8}Sr_{0.2}MnO_{3-\delta}$ nanoparticles were also found to increase [14].

Recently, Basith *et. al.* have synthesized Bi based multiferroic $Bi_{0.9}Gd_{0.1}Fe_{1-x}Ti_xO_3$ nanoparticles by ultrasonication of their micro-meter size bulk powder materials [15]. The variation of the size of $Bi_{0.9}Gd_{0.1}Fe_{1-x}Ti_xO_3$ nanoparticles as a function of

sonication time for a fixed power of the ultrasonic bath was reported [15]. The transmission electron microscopy imaging confirmed the formation of single crystalline nanoparticles with a mean size of 11-13 nm for 60 minutes sonication. In the present investigation, we have synthesized nanoparticles of rare-earth based $Gd_{0.7}Sr_{0.3}MnO_3$ by ultrasonication of their bulk powder materials [15] to compare the magnetic properties between nanoparticles and their bulk counterparts. This compound was chosen due to the fact that $Gd_{0.7}Sr_{0.3}MnO_3$ contain significant amount of heavy rare earth Gd and the magnetic properties of rare-earth based manganites are quite different than that of Bi based nanostructures as reported in Ref. [16]. Moreover, a number of Gd-Sr manganites [17] are well studied in the bulk form as a single crystal [18] and polycrystalline samples [9]. This ultimately allowed us to compare extensively the magnetic properties of $Gd_{0.7}Sr_{0.3}MnO_3$ nanoparticles and their bulk counterparts.

1.2 Objectives with specific aims

The main objectives of the present research are as follows:

(a) Preparation of composition of $Gd_{0.7}Sr_{0.3}MnO_3$ bulk perovskite manganites by using solid state reaction method [19].

(b) Preparation of nanoparticlesk from bulk perovskite powder using ultrasonication method [15] and ball milling technique.

(c) Investigation of the crystal structure of the bulk perovskite and nanoparticles of $Gd_{0.7}Sr_{0.3}MnO_3$ using X-ray diffraction (XRD) technique.

(d) Investigation of the surface morphology of the as prepared sample using scanning electron microscopy (SEM). Investigation of the particle size distribution of the synthesized nanoparticles using Transmission Electron Microscopy (TEM) imaging.

(e) Investigation of the existence of oxygen vacancies of $Gd_{0.7}Sr_{0.3}MnO_3$ nanoparticle and their bulk ceramic using X-ray photoelectron spectroscopy (XPS) technique.

(f) Measurements of the magnetic properties such as saturation magnetization (M_s), remanent magnetization (M_r) and coercivity (H_c) of $Gd_{0.7}Sr_{0.3}MnO_3$ bulk powder

and nanoparticles from hysteresis loops by using Superconducting Quantum Interference Device (SQUID).

(g) Investigation of the phase transition temperature of the bulk materials as well as nanoparticles from temperature dependent magnetization measurements using (SQUID) magnetometer.

1.3 Summary of the Thesis

The summary of the thesis is as follows:

Chapter 1 of this thesis deals with the introduction and importance of perovskite manganite nanoparticles and objectives of the present work.

Chapter 2 gives a brief overview of the materials, theoretical background as well as crystal structure of the perovskite manganites.

Chapter 3 gives the detailed description of the sample preparation and different measurement techniques that have been used in this research work.

Chapter 4 is devoted to the results of various investigations of the study and explanation of results in the light of existing theories.

The conclusions drawn from the overall experimental results and discussion are presented in Chapter 5.

References:

[1]   Zhang, T., Wang, X. P., Fang, Q. F. and Li, X. G., "Magnetic and charge ordering in nanosized manganites", Applied Physics Reviews, 1, 031302, 2014.

[2]   Dolgin, B , Puzniak, R , Mogilyansky, D, Wisniewski, A, Markovich, V and Jung, G J., "Magnetic dynamic properties of electron-doped $La_{0.23}Ca_{0.77}MnO_3$ nanoparticles", Phys.: Condens. Matter 25, 076004, 2013.

[3]   Debnath, J. C., Zeng, R., Strydom, A. M., Wang, J. Q., Dou, S. X., "Ideal Ericsson cycle magnetocaloric effect in $(La_{0.9}Gd_{0.1})_{0.67}Sr_{0.33}MnO_3$ single crystalline nanoparticles", Journal of Alloys and Compounds, 555, 33–38, 2013.

[4]   Vladimir Markovich, Ivan Fita, Andrzej Wisniewski, Roman Puzniak, Dmitrii Mogilyansky, Przemyslaw Iwanowski, Piotr Dluzewski and Gad Gorodetsky, "Nanometer Size Effect on Magnetic Properties of $Sm_{0.8}Ca_{0.2}MnO_3$ Nanoparticles", J. Phys. Chem. C, 116, 435–447, 2012.

[5]   Zhu, T., Shen, B. G., Sun, J. R, Zhao, H. W. and Zhan, W. S., "Surface spin-glass behavior in $La_{2/3}Sr_{1/3}MnO_3$ nanoparticles", J. Appl. Phys. Lett., 78, 3863, 2001.

[6]   Hehn, M., Punadjela, K., Bucher, J., Roussseausx, F., Decanini, D., Bartenlian, B. and Chappert, C., "Nanoscale Magnetic Domains in Mesoscopic Magnets", Science, 272, 1782, 1996.

[7]   Katiyar, P., Kumar, D., Nath, T. K., Kvit, A. V., Narayan, J. and Singh, R., K., "Magnetic properties of self-assembled nanoscale $La_{2/3}Ca_{1/3}MnO_3$ particles in an alumina matrix", J. Appl. Phys. Lett., 79, 1327, 2001.

[8]   Gupta, A., Gong, G. Q., Xiao, G., Duncombe, P. R., Lecoeur, P., Trouilloud, P., Wang, Y. Y., Dravid, V. P. and Sun, J. Z., "Grain-boundary effects on the magnetoresistance properties of perovskite manganite films", Phys. Rev. B, 54, 22, R15629-32, 1996.

[9]   Garca-Landa, B., De Teresa, J. M. and Ibarra, M. R., Ritter, C., Drost, R., Lees, M. R., "Colossal magnetoresistance in $Gd_{1/2}Sr_{1/2}MnO_3$", J. App. Phys., 83, 7664, 1998.

[10]   Shantha Shankar, K., Sohini Kar, Subbanna, G. N., Ray-chaudhuri, A. K., "Enhanced ferromagnetic transition temperature in nanocrystalline lanthanum

calcium manganese oxide ($La_{0.67}Ca_{0.33}MnO_3$)", Solid State Communications, 129, 7, 479-483, 2004.

[11] Muroi, M., Street, R., and McCormick, P. G., "Enhancement of critical temperature in fine $La_{0.7}Ca_{0.3}MnO_3$ particles prepared by mechanochemical processing", J. App.Phys., 87, 3424, 2000.

[12] Phan, T.-L. , "An Effective Route to Prepare $La_{0.7}Ca_{0.3}MnO_3$ Nanoparticles: Structural Characterization and Magnetic Properties", New Phys.: Sae Mulli, 63, 557–561, 2013.

[13] Ono, K., Kakefuda, Y., Okuda, R., Ishii, Y., Kamimura, S., Kitamura, A. and Oshima, M. J., "Organometallic synthesis and magnetic properties of ferromagnetic Sm–Co nanoclusters", J. Appl. Phys., 91, 8480, 2002.

[14] Roy, S., Dubenko, I., Edorh, D. D. and Ali, N. J., "Size induced variations in structural and magnetic properties of double exchange $La_{0.8}Sr_{0.2}MnO_{3-\delta}$ nano-ferromagnet", J. Appl. Phys., 96, 1202, 2004.

[15] Basith, M. A., Ngo, D. –T., Quader, A., Rahman, M. A., Sinha, B. L., Bashir Ahmmad, Fumihiko Hirose and Molhave, K., "Simple top-down preparation of magnetic $Bi_{0.9}Gd_{0.1}Fe_{1-x}TixO_3$ nanoparticles by ultrasonication of multiferroic bulk material", Nanoscale, 6, 14336, 2014.

[16] Rao, S. S. and Bhat, S. V., "Preparation, Characterization, and Magnetic Studies of $Bi_{0.5}X_{0.5}$(X = Ca, Sr)MnO_3 Nanoparticles", J. Nanosci. Nanotechnol., 7, 2025–2028, 2007.

[17] Sagar, S., Ganesan, V., Joy, P. A., Senoy Thomas, Liebig, A., Albrecht, M. and Anantharaman, M. R., "Investigations on the Multiferroic and Thermoelectric properties of Low and Intermediate band width Manganites", EPL, 91, 17008, 2010.

[18] Aditya, A. Wagh, Anil Kumar, P. S., Bhat, H. L. and Suja Elizabeth, "An investigation of first-order transition across charge ordered and ferromagnetic phases in $Gd_{0.5}Sr_{0.5}MnO_3$ single crystals by magnetic and magnetotransport studies", J. Phys.: Condens. Matter, 22, 2, 026005, 2010.

[19]   Basith, M. A., Kurni, O., Alam, M. S., Sinha, B. L., Ahmmad, B., "Room temperature dielectric and magnetic properties of Gd and Ti co-doped $BiFeO_3$ ceramics", J. Appl. Phys.,115, 024102, 2014.

CHAPTER 2
BACKGROUND

2.1 Introduction

Magnetism is a physical phenomenon first recorded around 600 BC by Greek philosophers studying ferrite rocks (lodestone). Today it is one of the most important properties of nature and is used in a multitude of technological devices from power plants to computer chips. This is largely due to the interaction of magnets with electricity, which is used to make electric motors. Magnetic materials are also found to be used in computers as hard disk drives, due to huge capacity for storing digital information securely. This, however, has been the result of years" worth of investment in the research and development of magnetic materials for hard disk recording. This investment has paid off since the storage capacity of typical hard drives has effectively doubled every few years since the 1980s. However, a point will soon be reached where there will be fundamental physical limitations on data storage density [1]. In order to fulfill the demand for high storage density a deeper understanding of the underlying physics relating to the nanoscale is required.

2.2 Origin of Magnetism

The origin of magnetism lies in the orbital and spin motions of electrons and how the electrons interact with one another. The best way to introduce the different types of magnetism is to describe how materials respond to magnetic fields. It is just that some materials are much more magnetic than others. The main distinction is that in some materials there is no collective interaction of atomic magnetic moments, whereas in other materials there is a very strong interaction between atomic moments. The magnetic moment of an electron in orbit is given by

$$\mu = \pi r^2 \, (ev/2\pi r) = evr/2 \tag{2.1}$$

Where r is the radius of orbit, e is charge and v is the velocity

The angular momentum of an electron must be an integral multiple of Plank"s const.

$$Mvr = nh/2\pi \tag{2.2}$$

Where m is the mass and h is the Planck's const.

If the electron revolves in the first orbit then n=1

Therefore orbital magnetic moment of an electron is given by from (2.1) and (2.2)

$$\mu = eh/4\pi m \tag{2.3}$$

This is known as Bohr magneton, the smallest possible orbital magnetic moment.

A simple electromagnet can be produced by wrapping copper wire into the form of a coil and connecting the wire to a battery. A magnetic field is created in the coil but it remains there only while electricity flows through the wire. The field created by the magnet is associated with the motions and interactions of its electrons, the minute charged particles which orbit the nucleus of each atom. Electricity is the movement of electrons, whether in a wire or in an atom, so each atom represents a tiny permanent magnet in its own right. The circulating electron produces its own orbital magnetic moment, measured in Bohr magnetons (μ_B), and there is also a spin magnetic moment associated with it due to the electron itself spinning, like the earth, on its own axis (illustrated in Figure 2.1). In most materials there is resultant magnetic moment, due to the electrons being grouped in pairs causing the magnetic moment to be cancelled by its neighbor.
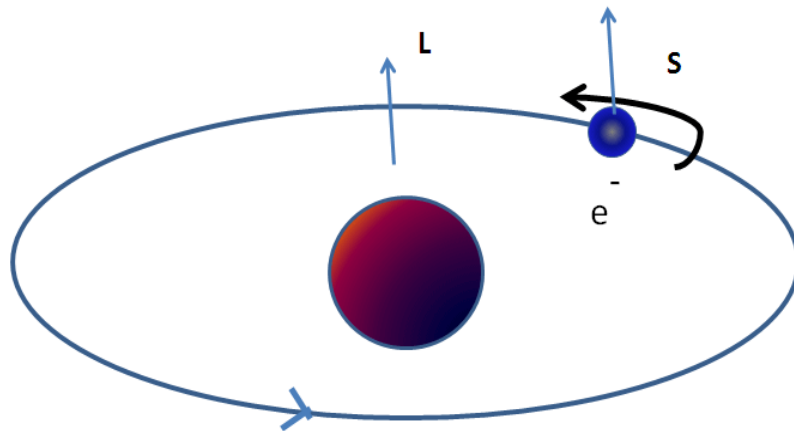
Figure 2.1. A spin magnetic moment associated with it due to the electron itself like the earth on its own axis.

In certain magnetic materials the magnetic moments of a large proportion of the electrons align, producing a unified magnetic field. The field produced in the material (or by an electromagnet) has a direction of flow and any magnet will experience a force

trying to align it with an externally applied field. The smallest possible magnetic moment due to spin of the electron is μ =eh/4πm. According to quantum theory the spin of electrons have only two possibilities +1/2 or -1/2. Similar to eqn. (2.3) we can write in the form

$$\mu = (e/2m)\ S \tag{2.4}$$

Where S is the spin quantum number.

In short,

$$\mu = g.(e/2m).S \tag{2.5}$$

Here g is the term known as g- factor. When g=2, the spin contribution arises and when g=1 the orbital contribution arises. The mass of the nucleus is so large that the magnetic moment contribution can be neglected compared to the electronic magnetic moment. The gyromagnetic ratio is proportional to the g-factor and 'g' arises due to the precession of the electrons similar to the precession of a top in a gravitational force. The value of g tells us whether the origin of magnetic moment is spin or orbital motion of electrons.

2.3 Magnetic moment of atoms

The strength of a magnetic dipole, called the magnetic dipole moment, may be thought of as a measure of a dipole's ability to turn itself into alignment with a given external magnetic field. In a uniform magnetic field, the magnitude of the dipole moment is proportional to the maximum amount of torque on the dipole, which occurs when the dipole is at right angles to the magnetic field [2].

The magnetic moment or magnetic dipole moment is a measure of the strength of a magnetic source. In the simplest case of a current loop, the magnetic moment is defined as:

$$\mu_m = I \int da \tag{2.6}$$

Where *a* is the vector area of the current loop, and the current, *I* is constant. By convention, the direction of the vector area is given by the right hand rule (moving one's right hand in the current direction around the loop, when the palm of the hand is „touching" the loop's surface, and the straight thumb indicate the direction).

In the more complicated case of a spinning charged solid, the magnetic moment can be found by the following equation:

$$\overrightarrow{\mu_m} = \frac{1}{2}\int \vec{r} \times \vec{J}\, d\tau \qquad (2.7)$$

where, $d\tau = r^2 sin\theta\, dr\, d\theta\, d\varphi$, J is the current density.

Magnetic moment can be explained by a bar magnet which has magnetic poles of equal magnitude but opposite polarity. Each pole is the source of magnetic force which weakens with distance. Since magnetic poles come in pairs, their forces interfere with each other because while one pole pulls, the other repels. This interference is greatest when the poles are close to each other i.e. when the bar magnet is short. The magnetic force produced by a bar magnet, at a given point in space, therefore depends on two factors: on both the strength P of its poles and on the distance d separating them. The force is proportional to the product, $\mu= PR$, where, μ describes the „magnetic moment" or „dipole moment" of the magnet along a distance R and its direction as the angle between R and the axis of the bar magnet. Magnetism can be created by electric current in loops and coils so any current circulating in a planar loop produces a magnetic moment whose magnitude is equal to the product of the current and the area of the loop. When any charged particle is rotating, it behaves like a current loop with a magnetic moment.

The equation for magnetic moment in the current-carrying loop, carrying current I and of area vector a for which the magnitude is given by:

$$\vec{\mu}_m = Ia \qquad (2.8)$$

where, μ_m is the magnetic moment, a vector measured in ampere-square meters, or equivalent joules per tesla, I is the current, a scalar measured in amperes, and is the loop area vector, having as x, y and z coordinates the area in square meters of the projection of the loop into the yz-, zx- and xy-planes.

2.4 Magnetic moment of electrons

The electron is a negatively charged particle with angular momentum. A rotating electrically charged body in classical electrodynamics causes a magnetic dipole effect creating magnetic poles of equal magnitude but opposite polarity like a bar magnet. For magnetic dipoles, the dipole moment points from the magnetic south to the magnetic

north pole. The electron exists in a magnetic field which exerts a torque opposing its alignment creating a potential energy that depends on its orientation with respect to the field. The magnetic energy of an electron is approximately twice what it should be in classical mechanics. The factor of two multiplying the electron spin angular momentum comes from the fact that it is twice as effective in producing magnetic moment. This factor is called the electronic spin g-factor. The persistent early spectroscopists, such as Alfred Lande, worked out a way to calculate the effect of the various directions of angular momenta. The resulting geometric factor is called the Lande *g*-factor.

The intrinsic magnetic moment of a particle with charge *q*, mass *m*, and spin *s*, is *s*

$$\vec{\mu}_m = g \frac{q}{2m} \vec{s} \tag{2.9}$$

where, the dimensionless quantity *g* is called the g-factor. The g-factor is an essential value related to the magnetic moment of the subatomic particles and corrects for the precession of the angular momentum. One of the triumphs of the theory of quantum electrodynamics is its accurate prediction of the electron *g* factor, which has been experimentally determined to have the value 2.002319. The value of 2 arises from the Dirac equation, a fundamental equation connecting the electron's spin with its electromagnetic properties, and the correction of 0.002319, called the anomalous magnetic dipole moment of the electron, arises from the electron's interaction with virtual photons in quantum electrodynamics. Reduction of the Dirac equation for an electron in a magnetic field to its non-relativistic limit yields the Schrödinger equation with a correction term which takes account of the interaction of the electron's intrinsic magnetic moment with the magnetic field giving the correct energy [2]. The total spin magnetic moment of the electron is

$$\vec{\mu}_s = -g_s \mu_B (\vec{s} / \hbar) \tag{2.10}$$

where $g_s = 2$ in Dirac mechanics, but is slightly larger due to Quantum Electrodynamics effects, μ_B is the Bohr magneton and *s* is the electron spin. The *z* component of the electron magnetic moment is

$$\vec{\mu}_Z = -g_s \mu_B m_s \tag{2.11}$$

where, m_s is the spin quantum number. The total magnetic dipole moment due to orbital angular momentum is given by

$$\vec{\mu}_s = -\frac{e}{2m_e}L = -\mu_B\sqrt{l(l+1)} \tag{2.12}$$

where, μ_B is the Bohr magneton. The z-component of the orbital magnetic dipole moment for an electron with a magnetic quantum number m_l is given by

$$\vec{\mu}_Z = -\mu_B m_l \tag{2.13}$$

2.5 Magnetic Behavior

The magnetic properties of a matter are fundamentally the result of the electrons of the atom, which have a magnetic moment by means of the electron motion. There are two types of electronic motion, spin and orbital, and each has a magnetic moment associated with it. Since the response of a material to a magnetic field (H) is characteristic of the magnetic induction or the flux density (B) and the effect that a material has upon the magnetic induction in a magnetic field is represented by the magnetization (M). Thus a universal equation can be established, relating these three magnetic quantities, by

$$B = \mu_0(H+M) \tag{2.14}$$
$$B = \mu H \tag{2.15}$$

where, μ_0 is a universal constant of permeability in a free space and μ is the permeability of a material. In equation (2.14), one can see that $\mu_0 H$ is the magnetic induction generated by the field alone and $\mu_0 M$ is the additional magnetic induction contributed by a material. The magnetic susceptibility (χ) is defined as the ratio of magnetization to magnetic field

$$\chi = \frac{M}{H} \tag{2.16}$$

The permeability and susceptibility of a material is correlated with respect to each other by

$$\mu = \mu_0(1+\chi) \tag{2.17}$$

The magnetic behavior of materials can be classified into the following five major groups:

1. Diamagnetism

2. Paramagnetism

3. Ferromagnetism

4. Antiferromagnetism

5. Ferrimagnetism

2.5.1 Diamagnetism
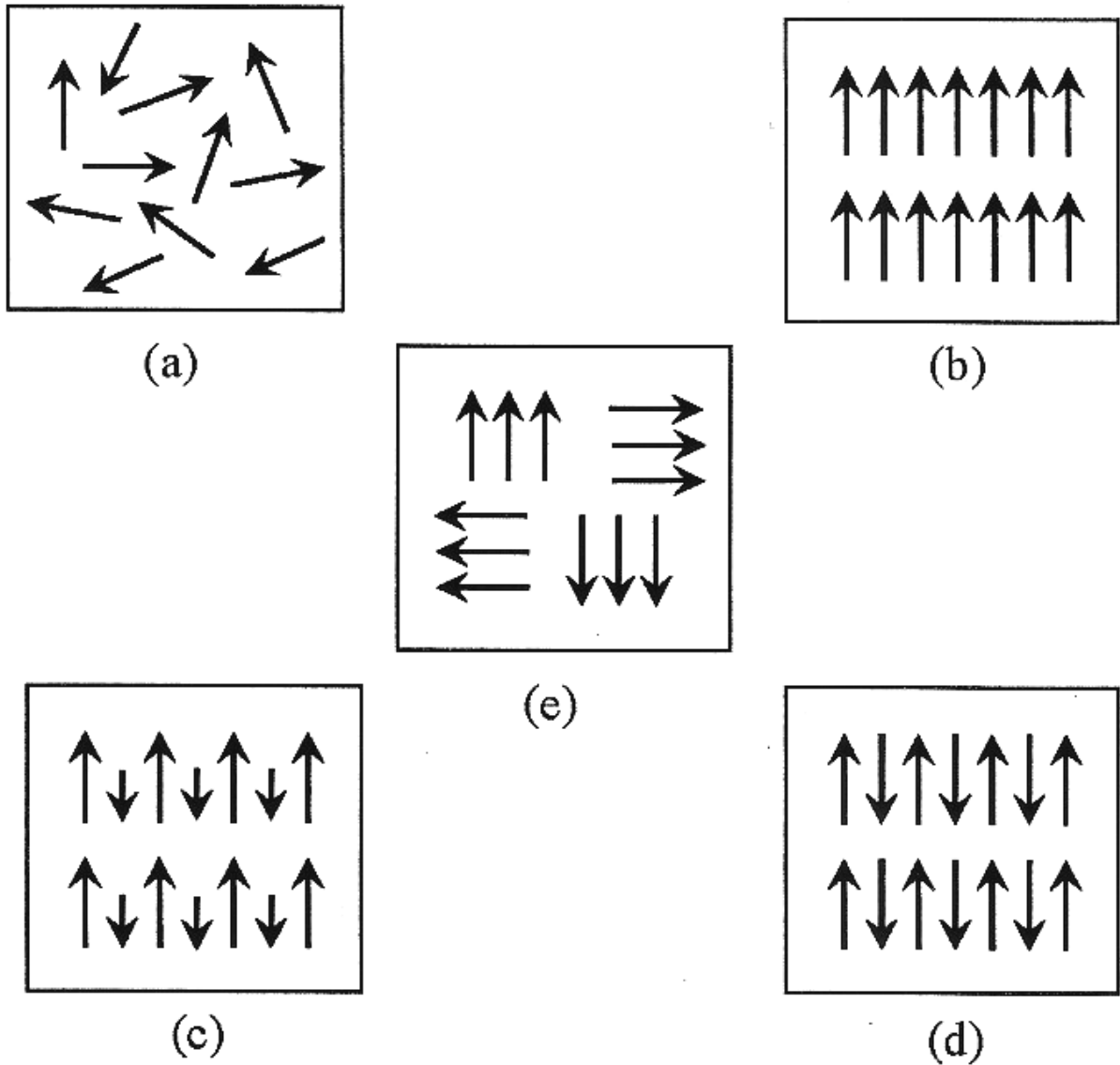
Figure 2.2: Varieties of magnetic orderings (a) paramagnetic, (b) ferromagnetic, (c) ferrimagnetic, (d) antiferromagnetic and (e) superparamagnetic.

Diamagnetism is a fundamental property of all matter, although it is usually very weak. It is due to the non-cooperative behavior of orbiting electrons when exposed to an applied magnetic field. Diamagnetic substances are composed of atoms which have no net magnetic moments (i.e., all the orbital shells are filled and there are no unpaired electrons). However, when exposed to a field, a negative magnetization is produced and thus the susceptibility is negative. It obeys Lenz's law. The other characteristic behavior of diamagnetic materials is that the susceptibility is temperature independent. The typical values of susceptibility on the order of 10^{-5} to 10^{-6}. Most of the materials are diamagnetic, including Cu, B, S, N2 and most organic compounds.

2.5.2 Paramagnetism

Paramagnetic materials possess a permanent dipole moment due to incomplete cancellation of electron spin and/or orbital magnetic moments (unpaired electrons). In the absence of an applied magnetic field the dipole moments are randomly oriented; therefore the material has no net macroscopic magnetization. When a field is applied these moments tend to align by rotation towards the direction of the applied field and the material acquires a net magnetization [4]. The magnetic moment can be oriented along an applied field to give rise to a positive susceptibility and the values of susceptibility are very small with the order of 10^{-5} to 10^{-3}. O_2, NO, Mn and Cr are just a few examples of the paramagnetic materials. The susceptibility of a paramagnetic material is inversely dependent on temperature, which is known as Curie law (Figure 2.3a)

$$\chi = \frac{C}{T} \tag{2.18}$$

where C is the Curie constant.

2.5.3 Ferromagnetism

Ferromagnetic material differs from diamagnetic and paramagnetic materials in many different ways. In a ferromagnetic material, the exchange coupling between neighboring moments leads the moments to align parallel with each other. In ferromagnetic materials, this permanent magnetic moment is the result of the cooperative interaction of large numbers of atomic spins in what are called domains regions where all

spins are aligned in the same direction. The exchange force is a quantum mechanical phenomenon due to the relative orientation of the spins of two electrons.

Therefore, the ferromagnetic materials generally can acquire a large magnetization even in absence of a magnetic field, since all magnetic moments are easily aligned together. The susceptibility of a ferromagnetic material does not follow the Curie law, but displayed a modified behavior defined by Curie-Weiss law (Figure 2.3b).

$$\chi = \frac{C}{T-\theta} \tag{2.19}$$

C is a constant and θ is called Weiss constant. For ferromagnetic materials, the Weiss - constant is almost identical to the Curie temperature (T_c). At temperature below Tc, the magnetic moments are ordered whereas above T_c, material losses magnetic ordering and show paramagnetic character. The elements Fe, Ni, and Co and many of their alloys are typical ferromagnetic materials.
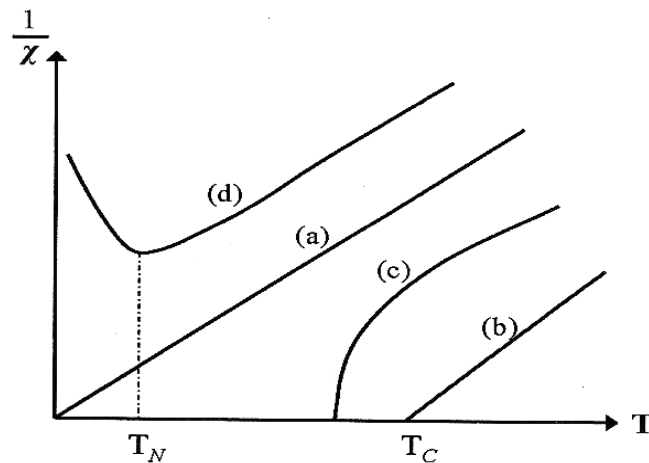
Figure 2.3. The inverse susceptibility varies with temperature T for (a) paramagnetic, b) ferromagnetic, (c) ferrimagnetic, (d) antiferromagnetic materials. T_N and T_c are Néel temperature and Curie temperature, respectively.

Two distinct characteristics of ferromagnetic materials are:

> ➤ Spontaneous magnetization and

> ➤ The existence of magnetic ordering temperature (Curie temperature)

The spontaneous magnetization is the net magnetization that exists inside a uniformly magnetized microscopic volume in the absence of a field. The magnitude of this magnetization, 0K, is dependent on the spin magnetic moments of electrons. The

saturation magnetization is the maximum induced magnetic moment that can be obtained in a magnetic field (Heat); beyond this field no further increase in magnetization occurs. Saturation magnetization is an intrinsic property, independent of particle size but dependent on temperature.

Even though electronic exchange forces in ferromagnets are very large, thermal energy eventually overcomes the exchange and produces a randomizing effect. This occurs at a particular temperature called the Curie temperature (T_c). Bellow the Curie temperature, the ferromagnet is ordered and above it, disordered. The saturation magnetization goes to zero at the Curie temperature. The Curie temperature is also an intrinsic property.

2.5.4 Antiferromagnetism

Antiferromagnetic material aligns the magnetic moments in a way that all moments are anti-parallel to each other, the net moment is zero. The anti-ferromagnetic susceptibility is followed the Curie-Weiss law with a negative θ as in equation (2.19). The inverse susceptibility as a function of temperature is shown in figure 2.3(d). Common examples of materials with antiferromagnetic ordering include MnO, FeO, CoO and NiO.

2.5.5 Ferrimagnetism

Ferrimagnetic material has the same anti-parallel alignment of magnetic moments as an antiferromagnetic material does. However, the magnitude of magnetic moment in one direction differs from that of the opposite direction. As a result, a net magnetic moment remains in the absence of external magnetic field. The behavior of susceptibility of a ferrimagnetic material also obeys Curie-Weiss law and has a negative θ as well in Fig. 2.3(c). In ionic compounds, such as oxides, more complex forms of magnetic ordering can occur as a result of the crystal structure. The magnetic structure is composed of two magnetic sublattices (called *A* and *B*) separated by oxygens. The exchange interactions are mediated by the oxygen anions. When this happens, the interactions are called indirect or superexchange interactions. The strongest superexchange interactions

result in an antiparallel alignment of spins between the *A* and *B* sublattice. In ferrimagnets, the magnetic moments of the *A* and *B* sublattices are not equal and result in a net magnetic moment. Ferrimagnetisrn is therefore similar to ferromagnetism. It exhibits all the hallmarks of ferromagnetic behavior like spontaneous magnetization, Curie temperature, hysteresis, and remanence. However, ferro- and ferrimagnets have very different magnetic ordering.

2.6 Hysteresis Loop

In addition to the Curie temperature and saturation magnetization, ferromagnets and ferrimagnets can retain a memory of an applied field once it is removed. This behavior is called hystresis and a plot of the variation of magnetization with magnetic field is called a hysteresis loop. Another hysteresis property is the coercivity of remanence (H_r) as in Fig. 2.4. This is the reverse field which, when applied and then removed, reduces the saturation remanence to zero is always larger than the coercive force. The initial susceptibility (χ_0) is the magnetization in low fields, on the order of the earth˝s field (50-100 μT). The various hysteresis parameters are not solely intrinsic properties but are dependent on grain size, domain state, stresses, and temperature. Because hysteresis parameters are dependent on grain size, they are useful for magnetic grain sizing of natural samples.
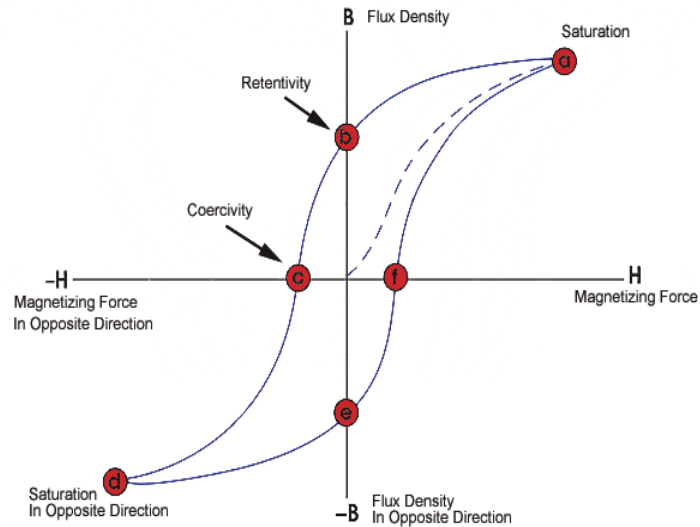
Figure 2.4: M-H loop for ferromagnetic material.

2.7 Micromagnetic energy terms

A number of different competitive micromagnetic energy terms contribute to the total energy of a ferromagnetic specimen. A stable state is reached when the micromagnetic energy is locally minimized. These energy terms are discussed in the following sections.

2.7.1 Exchange energy

The exchange energy suggests a uniform magnetization and is at the origin of ferromagnetic order. It is a consequence of the Pauli Exclusion Principle, which forbids electrons with the same spins from having the same spatial wave function. To understand ex-change energy in terms of the Pauli Exclusion Principle, let us consider that two atoms with unpaired electrons approach each other. If the spins of these two electrons are antiparallel to each other, the electrons will share a common orbit. Therefore, the electrostatic Coulomb energy is increase. If, however, the spins of these two electrons are parallel, they cannot share a common orbit because of the Pauli Exclusion Principle. They form separate orbits and thus reduce the Coulomb interaction [5]. The exchange energy between two interacting electrons is given by:

$$e_{ex} = -2J_{12}s_1s_2 \qquad (2.20)$$

where J_{12} is the exchange integral between the two electrons, which can be negative or positive, and s_1, s_2 their spin vectors. The total exchange energy for a solid is found by summing the exchange over all electrons which contribute. In most cases this summation need only be carried out for nearest neighbours. Thus, the total exchange energy for the solid from all nearest neighbour spins is:

$$E_{ex} = -2JS^2 \sum_{ij} cos\psi_{ij} \qquad (2.21)$$

where S is the magnitude of the spin vector, ψ_{ij} is the angle between spins i and j. The exchange integral for ferromagnetic materials is positive. The negative sign in the expression then implies that a minimum exchange energy results from spins aligned parallel. For antiferromagnetic coupling this exchange integral is negative, giving the result that antiparallel alignment is preferred.

2.7.2 Magnetostatic energy

Inside a magnetic specimen, the magnetic induction B is expressed as

$$B = \mu_0 (H + M) \tag{2.22}$$

where μ_0 is the permeability of free space, H is the magnetic field strength and M is the magnetisation of the uniformly magnetised specimen. Using this relationship, the divergence of M can be expressed as

$$\nabla . M = \frac{\nabla . B}{\mu_0} \tag{2.23}$$

From Maxwell's equation,

$$\nabla . B = 0 \tag{2.24}$$

Therefore,

$$\nabla . H = -\nabla . M \tag{2.25}$$

This none zero divergence of magnetization at the sample surface and also from within volume of the material give rise to field H that ensures the continuity of lines of B. This field is known as the demagnetizing field or magnetostatic field or stray field H_d.

Therefore, we can write

$$\nabla . H_d = -\nabla . M \tag{2.26}$$

The energy associated with this stray field H_d is given by:

$$E_d = -\frac{\mu_0}{2} \int M . H_d dV \tag{2.27}$$

E_d can be minimised by reducing the amount of magnetic charge that builds up at the edges, surfaces and volume charges within the material.

2.7.3 Anisotropy energy

Magnetic anisotropy is related to the variations in the magnetic energy with the spatial orientation of the magnetisation. A variety of anisotropy contributions are possible such as intrinsic magnetocrystalline anisotropy, the magnetoelastic anisotropy, surface anisotropy, field induced anisotropy etc. originated microscopically from the spin-orbit coupling. Here we will describe magnetocrystalline and shape anisotropy which are described in the following sections.

2.7.3.1 Magnetocrystalline anisotropy

Weiss [6] suggested that in a demagnetised single crystal the domain magnetisations could lie in all directions. This would imply that measured magnetisation curves for the crystal would be indistinguishable whatever the direction of the applied field relative to the crystal axes. But experimental magnetisation curves revealed that much smaller applied fields are required to induce a given magnetisation in some directions of some materials, termed the easy directions, than in others. A deviation of the magnetization from an easy axis leads to an increase in the anisotropy energy, which has its maximum along a "hard axis". In the case of cubic anisotropy, the energy, E_k can be described by a series expansion:

$$E_k = \int [K_1(\alpha_1^2 \alpha_2^2 + \alpha_2^2 \alpha_3^2 + \alpha_3^2 \alpha_1^2) + K_2 \alpha_3^2 \alpha_1^2] dV \qquad (2.28)$$

where α_1, α_2, α_3 are the direction cosine of the magnetisation along 1, 2, 3, the respective crystallographic axes and K_1, K_2 are first and second magnetocrystalline anisotropic constants, respectively, for the particular material. For example, for Ni, $K_1 = -0.45 \times 104 J/m^3$ so that the easy axes are along the body diagonals (111), while for Fe, $K_1 = 4.8 \times 104 J/m^3$ and the easy axes are along along (100) [7]. These descriptions are only valid for single crystal materials. In the case of the polycrystalline material, there is no overall preferred axis for as the crystallites are randomly oriented with respect to each other. Instead, the anisotropy direction varies from crystallite to crystallite, resulting in local easy axes. The magnetisation ripple arises due to a deviation of the magnetisation from uniformity and run perpendicular to the average direction of the magnetisation [8].

2.7.3.2 Shape anisotropy

The magnetic shape anisotropy is particularly important to the magnetic configurations of the thin films and objects with reduced dimensions. It refers to the magnetostatic effects of the system rather than the overlap of electron orbitals. When a magnetic specimen is uniformly magnetised, the magnetic charges or free poles are present at the surface of the specimen. This surface charge distribution is itself a source of a magnetic field, called the demagnetising field. Figure 2.5 illustrates the

magnetostatic dipole interactions in an ellipsoid specimen magnetised along the long and short axes. It can be seen that free poles are separated by relatively long and short distances in an ellipsoid. The long and short distance corresponds to the two directions of magnetisation considered in the Fig. 2.5(a) and (b). The demagnetising field will be less if the magnetisation is along the long axis rather than the short axes. This produces an easy axis of magnetisation along the long axis. A sphere, on the other hand, has no shape anisotropy. Inside a specimen with ellipsoid shape (Fig. 2.5), the demagnetising field, H_d, is aligned oppositely to the direction of the magnetisation and the shape anisotropy energy will be given by

$$E_k = \int K_{eff} sin^2 \theta dV$$
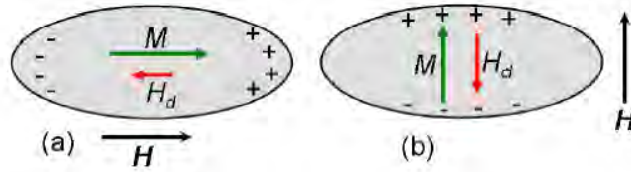
Figure 2.5: Schematically the demagnetising field that arises depending on whether the ellipsoid is magnetised along the (a) long or (b) short axis. (a) has lower demagnetizing field than (b) and was indicated by the relative sizes of the red arrow sign.

Here,

$$K_{eff} = \frac{(N_b - N_a)M^2}{2} \tag{2.29}$$

where θ is the angle between the long axis and the magnetisation direction, M is the magnetisation, and N_a, N_b are demagnetising factors in the long and the short axes, respectively. Beside magnetocrystalline and shape anisotropy, induced anisotropy can be created by certain treatment procedures e.g. magnetic annealing, in which an external magnetic field is applied during the heat treatment [9]. Another form of field induced anisotropy is possible to create in thin films, particularly in Py film [10]. In this case, the Py film is deposited on a substrate by evaporation in vacuum with a magnetic field applied in the plane of the substrate. As a result, the direction of the field is subsequently found to be an easy direction for the spontaneous magnetisation.

2.7.4 Zeeman energy

When the specimen is placed in an external field, the magnetic moments within the specimen will tend to align parallel to the applied field. The Zeeman energy takes into account the orientation of the magnetisation with respect to the applied field and is given by:

$$E_z = -\mu_0 \int \mathrm{M}.\, \mathrm{H} dV \tag{2.30}$$

Where, μ_0 is the permeability of free space.

2.7.5 Total energy

The total energy of a ferromagnetic specimen is the sum of the individual energy terms which were described in the previous sections

$$E_{total} = E_{ex} + E_k + E_z + E_d \tag{2.31}$$

and the magnetic configuration (domain structure discussed in the next section) is a direct consequence of its local or global minimisation.

2.8 Magnetic domains and domain walls

2.8.1 Magnetic domains
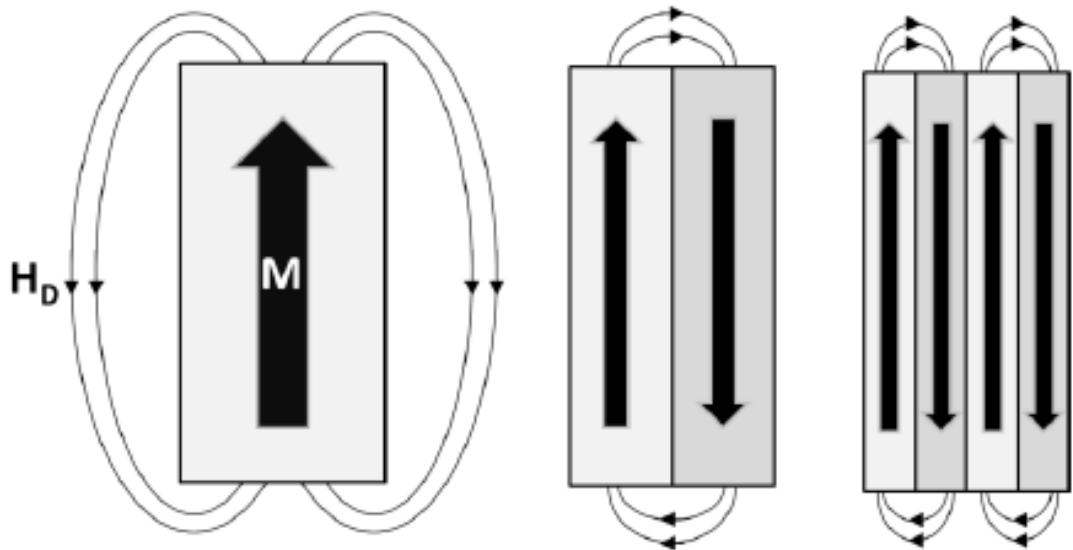
Figure 2.6: Domain structure in a uniaxial single crystal [11].

Initially proposed by *Weiss* in 1906 domain theory is now central to understanding the magnetisation processes in magnetic materials. Domains form to reduce the magnetostatic energy of a magnetic material, the energy stored in the field which attempts to demagnetise the sample. This process is shown schematically in Figure 2.6 for a material with strong uniaxial anisotropy (e.g. Co) [11].

The schematic shows that when a magnetic material is saturated in one direction an opposing field is created, this is the demagnetising field H_D which stores the magnetostatic energy Ems. The magnetostatic energy is dependent primarily on the magnitude of the magnetisation of the sample. To reduce this magnetisation, and therefore Ems, a magnetic material breaks into domains [11]. Each domain contains magnetic moments aligned parallel to each other. Their magnetic moments preferentially lie along the easy axes of the material. In the uniaxial material in Figure 2.7, the domains form with magnetisation aligned anti-parallel along the easy axis, reducing the demagnetising field and E_{ms}. It is also possible for the material to break into more than two domains to further reduce H_D. In systems with cubic anisotropy (like Heusler alloys) the domain structure is often more complex.
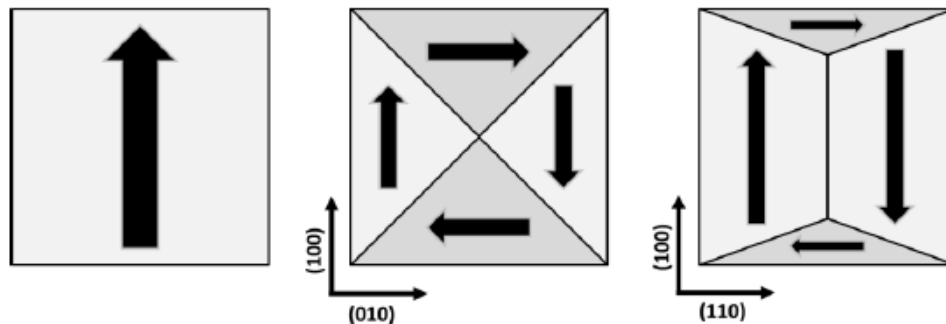
Figure 2.7: Domain structures in cubic materials [12].

In materials with cubic anisotropy it is possible to have more than one easy axis. This results in domains that can have their magnetisation aligned at 90° to one another and not just 180°. In Figure 2.7, we see the typical domain structure for a material where the anisotropy is cubic with an easy axis along the cube edge, [100], and intermediate axis along the face diagonal, [110]. If the crystal is cut so that a face is formed with [100]

and [010] edges all the domains are equal and align at 90° to one another in a „flux closure" configuration. This means that the magnetostatic energy is reduced to zero as there is no stray field. For the situation where the crystal is cut with a face with edges of [100] and [110] the domains along the easy axis become elongated relative to those at 90°. As a result a system is formed where a domain can have adjacent domains aligned simultaneously at 90° or 180°. This is important for single crystal Heusler alloy films as the induced small uniaxial anisotropy can result in a similar domain formation [13].

2.8.2 Magnetic domain walls

The interface between neighboring domains is not abrupt. The change in direction of moments occurs over some finite length, typically tens of nm. The magnetisation reverses through a series of slight rotations of the localised moments in the boundary region. These boundary regions are known as domain walls. There are two types of domain walls, Bloch walls and Néel walls, named after their respective discoverers. The difference between the two types of wall comes down to the way in which the magnetic moments rotate through the wall [14].
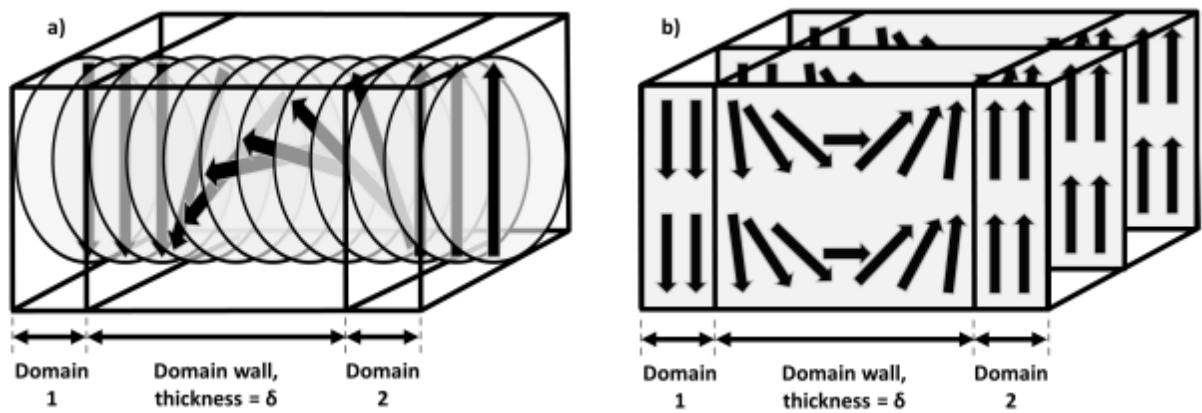
Figure 2.8: Schematic diagrams of 180° a) Bloch and b) Néel domain walls.

As shown in Figure 2.8, Bloch walls change the direction of the magnetisation through confinement of the rotation of magnetic moments to the plane parallel to the domain wall. Bloch walls occur when the magnetic moments rotate perpendicular to the

plane of the domain wall. Bloch walls occur in bulk samples. However, in thin films they create free poles at the sample surface which contribute significant magnetostatic energy to the system. To reduce this energy, Néel walls form which rotate in the plane so that free poles don"t appear at the film surface [13].

2.9 Magnetoresistance

One of the most fascinating magnetic-electrical properties of a magnetic is the magnetoresistance (MR) effect, which means the resistance of a material will change with the presence of an external magnetic field. This effect universally exists in most of the materials because of the interaction between the magnetic field and the conduction carriers. For nonmagnetic materials such as copper and gold, the MR effect is relatively inconspicuous compared to magnetic materials such as iron, nickel and cobalt.

Magnetoresistance (MR) is the change in resistance of the material under the application of externally applied magnetic field, H. The MR can be defined as

$$MR\% = \frac{\rho(H) - \rho(0)}{\rho(0)} \times 100 \tag{2.32}$$

where ρ_H and ρ_0 are the resistivities at a given temperature in the presence and absence of magnetic field, H respectively [15]. Manganites exhibit large negative MR under the application of magnetic field. In the following paragraphs a brief description about various types of MR effects in different materials is given.

2.9.1 Giant Magnetoresistance (GMR)

GMR is a very large change in electrical resistance observed in ferromagnet / paramagnet ferromagnet multilayer structures when the relative orientations of the magnetic moments in alternate ferromagnetic layers change as a function of applied field. The basis of the GMR is the dependence of the electrical resistivity of electrons in a magnetic metal on the direction of the electron spin, either parallel or antiparallel coupling to the magnetic moment of the multilayers. Electrons having parallel spins with the magnetic moment in films undergo less scattering and therefore have a lower resistance. When the moments of the magnetic layers are antiparallel, there are no

electrons which have a low scattering rate in both magnetic layers, causing an increased resistance. At applied magnetic fields where the moments of the magnetic layers are aligned, electrons with their spins parallel to these moments pass freely through the structure and hence lowering the electrical resistance. The relative huge change of resistance is giant magnetoresistance (GMR).

2.9.2 Colossal Magnetoresistance (CMR)
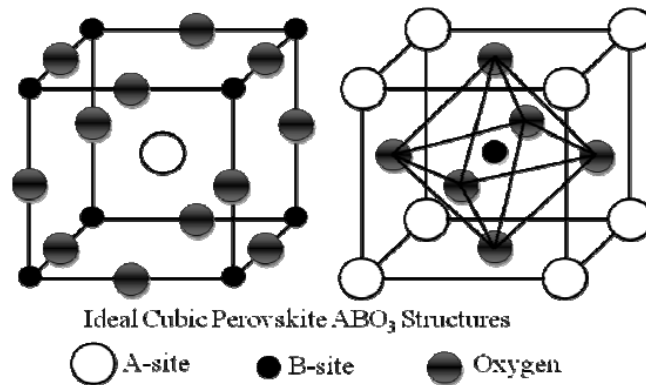
Figure 2.9: ABO_3perovskite structures.

In 1994, colossal magnetoresistance was first observed by S. Jin et al [16] in manganite perovskites drawing a renewed interest in these materials. It was known as early as 1950 that, the perovskite compound $LaMnO_3$ with the typical structure, shown in fig. 2.9, is normally an antiferromagnetic state. If approximately of the La^{3+} ions were replaced with divalent ions such as Ca^{2+}, Sr^{2+}, Pb^{2+} or Ba^{2+}, the resistance drops dramatically and the material appears to become ferromagnetic. The effect of substituting a divalent ion for a trivalent ion on the La-site was to force a nearby Mn to change from Mn^{3+} to Mn^{4+}. Whenever Mn^{3+} and Mn^{4+} are on neighboring Mn-sites, there exists the possibility of conductivity by electrons hopping from the Mn^{3+} to Mn^{4+} via the intervening oxygen anion (O^{2-}). This hopping process critically depends on the relative alignment of the neighboring Mn core spins. Consequently, the electrical resistivity is extremely sensitive to the external magnetic field, thus giving rise to CMR.

2.10 Microstructure

A polycrystal is much more than many tiny crystals bonded together. The interfaces between the crystals, or the grain boundaries which separate and bond the grains, are complex and interactive. The whole set of a given material's properties (mechanical, chemical, especially electrical and magnetic) depend strongly on the nature of the microstructure. In the simplest case, the grain boundary is the region, which accommodates the difference in crystallographic orientation between the neighboring grains. For certain simple arrangements, the grain boundary is made of an array of dislocations whose number and spacing depends on the angular deviation between the grains. The ionic nature of ferrites leads to dislocation patterns considerably more complex than in metals, since electrostatic energy accounts for a significant fraction of the total boundary energy [3]. For low-loss ferrite, Ghate [17] states that the grain boundaries influence properties by

i) creating a high resistivity intergranular layer,

ii) acting as a sink for impurities which may act as a sintering aid and grain growth modifiers,

iii) providing a path for oxygen diffusion, which may modify the oxidation state of cations near the boundaries.

In addition to grain boundaries, ceramic imperfections can impede domain wall motion and thus reduce the magnetic property. Among these are pores, cracks, inclusions, second phases, as well as residual strains. Imperfections also act as energy wells that pin the domain walls and require higher activation energy to detach. Stresses are microstructural imperfections that can result from impurities or processing problems such as too rapid a cool. They affect the domain dynamics and are responsible for a much greater share of the degradation of properties than would expect [17].

Grain growth kinetics depends strongly on the impurity content. A minor dopant can drastically change the nature and concentration of defects in the matrix, affecting grain boundary motion, pore mobility and pore removal [3]. The effect of a given dopant depends on its valence and solubility with respect to host material. If it is not soluble at the sintering temperature, the dopant becomes a second phase which usually segregates to the grain boundary.
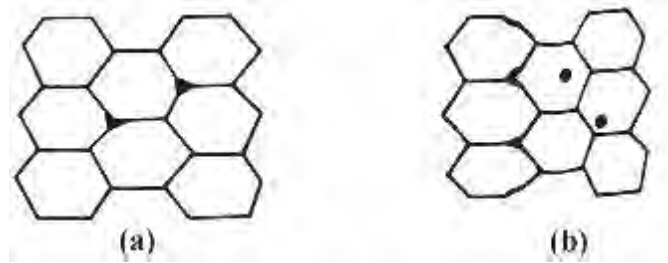
Figure 2.10: Porosity character: (a) intergranular, (b) intragranular.

The porosity of ceramic samples results from two sources, intragranular porosity and intergranular porosity, Fig. 2.10 An undesirable effect in ceramic samples is the formation of exaggerated or discontinuous grain growth which is characterized by the excessive growth of some grains at the expense of small, neighbouring ones, Fig. 2.11. When this occurs, the large grain has a high defect concentration. Discontinuous growth is believed to result from one or several of the following: powder mixtures with impurities; a very large distribution of initial particle size; sintering at excessively high temperatures; in ferrites containing Zn and /or Mn, a low O_2 partial pressure in the sintering atmosphere. When a very large grain is surrounded by smaller ones, it is called „duplex" microstructure.
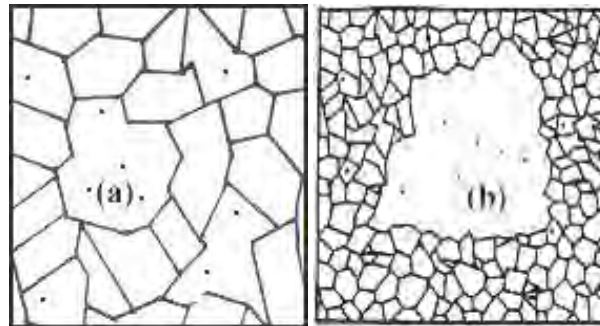
Figure 2.11: Grain growth (a) discontinuous, (b) duplex (schematic).

2.11 Nanoparticles

The term 'nanoparticle' is used to describe a particle with size in the range of 1 to 100 nm, at least in one of the three dimensions. Because of this very small size scale, they possess an immense surface area per unit volume, a high proportion of atoms in the

surface and near surface layers, and the ability to exhibit quantum effects. In this size range, the physical, chemical and biological properties of the nanoparticle change in fundamental ways from the properties of both individual atoms/molecules and of the corresponding bulk material. Nanoparticles exist with great chemical diversity in the form of metals, metal oxides, semiconductors, polymers, carbon materials, organics or biological. They also exhibit great morphological diversity with shapes such as spheres, cylinders, disks, platelets, hollow spheres and tubes, etc. Depending on the material they consist of, nanoparticles can possess a number of different properties such as high electron density and strong optical absorption (e.g. metal particles, in particular Au), photoluminescence (semiconductor quantum dots, e.g. CdSe or CdTe) or phosphorescence (doped oxide materials, e.g. Y_2O_3), or magnetic moment (e.g. iron or manganese oxide nanoparticles). The unique properties of these various types of nanoparticles give them novel electrical, catalytic, magnetic, mechanical, thermal, or imaging features that are highly desirable for applications in catalysis, biomedicines, and electronics, and environmental sectors.

2.11.1 Classification of Nanoparticles

Nanoparticles can be classified based upon their sizes, shapes, and materials, and with various chemical and surface properties. There is a constant and rapid growth in this field which adds to the basis of classification. However, the classes of nanoparticles listed below are mainly based upon their constituent materials, and some of their basic properties and current known uses are also described here.

2.11.1.1 Metal Nanoparticles

Noble metal nanoparticles, such as gold (Au), silver (Ag) and Cu nanoparticles and nanorods, exhibits unique electric, photonic and catalytic properties like local surface plasmon resonance (LSPR) [18,19], surface-enhanced Raman scattering (SERS) [20] and surface-enhanced fluorescence (SEF) [21]. The strong plasmon resonance band of the noble metal NPs in the visible region has been used in the development of biosensors for use in colorimetric detection of analytes [22-24]. The light absorption by NPs is related to the incident light interaction with the ksurface of the nanoparticle. When light of a

specific energy interacts with the surface of noble metal NP, an intense localized field is induced. The coupling of the NPs conduction band electrons with the electric field of incident light, at a resonant frequency, generates a localized plasmonic oscillation on the surface of the NPs, designated by surface plasmon resonance (SPR) or localized SPR (LSPR) [25].

2.11.1.2 Magnetic Nanoparticles

Magnetic nanoparticles are of great interest for researchers from a wide range of disciplines, including magnetic fluids [26], catalysis [27], biotechnology/biomedicine [28], magnetic resonance imaging [29], data storage [30], and environmental remediation [31]. Two key issues dominate the magnetic properties of nanoparticles: finite-size effects and surface effects which give rise to various special features. Finite-size effects result, for example, from the quantum confinement of the electrons, whereas typical surface effects are related to the symmetry breaking of the crystal structure at the boundary of each particle. Magnetic nanoparticles can be utilized in versatile ways, very similar to those of nanoparticles in general. However, the magnetic properties of these particles add a new dimension where they can be manipulated upon application of an external magnetic field. This property opens up new applications where drugs that are attached to a magnetic particle to be targeted in the body using a magnetic field. Here, we briefly introduce different kinds of magnetic nanoparticles.

2.12 Magnetism in nanostructures

In this section, we provide an overview of the fundamental aspects of magnetism in nanostructures.

2.12.1 Magnetic interactions

2.12.1.1 The single domain limit

It is well known that the occurrence of magnetic hysteresis in case of bulk FM materials can be explained by the formation of magnetic domains and by the motion of domain walls, which separate them. The formation of domains and domain walls is to

minimize the net free energy, which depends on the magnetostatic (proportional to the volume of the material) and domain wall (proportional to the surface area) energy. For a magnetic material, upon size reduction to the nanometer scale, a situation may arise where the formation of domains may become energetically unfavorable due to the domain wall energy. Such a condition can be called the single domain limit for that particular material, below which the sample consists of particles with a single uniformly magnetized domain.

2.12.1.2 Interactions between nanoparticles

In the single domain limit, the inter-particle and intra-particle interactions play a vital role in determining the magnetic responses for an ensemble of nanoparticles. The interaction strength between nanoparticles modifies the energy landscape. Hence it is essential to identify the different energy contributions, namely, anisotropy energy, Zeeman energy and dipolar interaction energy.

For nanoparticles under experimental conditions, in addition to the uniaxial crystalline anisotropy, contributions from the surface, shape and strain anisotropy have drastic effects on the magnetic properties. Also, various other interactions such as exchange interactions [32], Ruderman-Kittel-Kasuya-Yosida (RKKY) interactions [33] and superexchange interactions can factor into the magnetic response of the nanoparticles. In case of manganites, the double-exchange (DE) and superexchange (SE) interactions influence the stabilization of ferromagnetic and antiferromagnetic ordering.

2.12.1.3 Spin glass

The formation of a spin glass state below a certain temperature in nanostructures is very often seen. In this section, we briefly discuss the characteristics of a spin glass with respect to a bulk material, and how it evolves in magnetic nanoparticles. Spin glass is a metastable state which arises in a material due to randomness and frustration of spins. The magnetic frustration in a material can develop due to uncompensated spins, or from the competition between nearest neighbor and next nearest neighbor interactions.
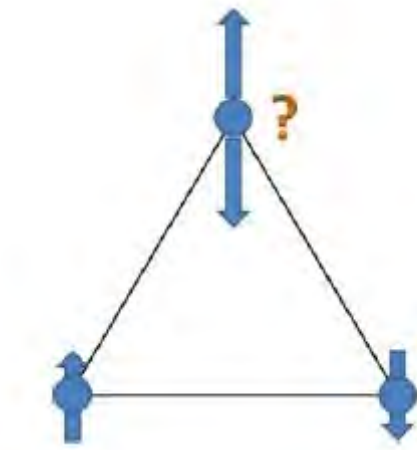
Figure 2.12: Schematic diagram of a magnetically frustrated triangular lattice.

In Figure 2.12, an antiferromagnetic triangular lattice is shown which is intrinsically frustrated. Energetically, the orientation of the third spin in the „up" or „down" direction is indistinguishable. Hence, there exists degeneracy in the energy ground state, and the system is magnetically frustrated. In another scenario, if one introduces magnetic impurities in an otherwise non-magnetic material, then as a result of the interactions with varied strengths due to the random positioning of the magnetic atoms, the system remains magnetically disordered. If the temperature of such a system is lowered, it has been observed that below a certain temperature the magnetic spins enter into an irreversible state (i.e. magnetization reversal becomes critically slow) which is associated with cooperative spin freezing. This temperature for a material is called its spin glass transition temperature. Below this temperature, the glassy nature of the material is thought to originate due to the independent slowing down of the spins, and the consequent formation of locally correlated units called droplets, clusters or domains. Several theories like the Sherrington-Kirkpatrick (SK) model [34], the Edwards-Anderson (EA) model [35], the hierarchical model, the droplet model, and the fractal-cluster model have been proposed to understand the spin glass behavior [36].

It should be mentioned that spin glasses can be of primarily three kinds, namely, (i) canonical spin glass, (ii) cluster glass, and (iii) surface spin glass. A canonical spin glass is usually formed by noble metals (Au, Ag, Pt, Cu), which are weakly doped with 3d transition metal ions such as Fe, or Mn [37]. Since the magnetic impurities are placed

within a conducting matrix, the magnetic interaction is usually RKKY type. As a result of the random placements of the spins in the host metal, some spin-spin interactions may be positive (favoring parallel alignment), while others may be negative leading to an antiparallel alignment. This leads to a magnetic frustration. For a system which exhibits phase separation, such that FM clusters grow within an AFM matrix, it may be possible that the finitely correlated small FM domains interact with one another leading to a glassy state which is called cluster glass type. The glassy dynamics in such materials is sensitive to the average FM cluster size, which in turn depends on the temperature and external magnetic field. In case of nanostructures, where the surface effects become significant, it are common to observe magnetic frustration arising due to broken symmetry of the surface spins which manifests into what is called a surface spin glass [38-40]. The exchange interaction between the surface spins and the core moments (below the glass transition temperature) of the nanostructures can trigger the exchange bias effect.

Interestingly, the concept of spin glass as understood in case of bulk materials by considering atomic spins, can be extended to magnetic nanoparticles, where the atomic spins are replaced by „superspins" which is discussed in the following section.

2.12.1.4 Supermagnetism

The last decade has witnessed a growing interest in research on the collective behavior of single domain magnetic nanoparticles giving rise to the field of „Supermagnetism" [41]. One can associate a large magnetic moment (few hundred to a few thousand μB) with each nanoparticle, which is called a „superspin". Depending on the strength of inter-particle interactions, an ensemble of superspins can exhibit three different magnetic states : (i) Superparamagnetism, (SPM) for the case of no interaction, (ii) superspin glass (SSG) for intermediate interaction strengths, and (iii) superferromagnetism for highly interacting superspins [30]. However, some recent experimental studies have revealed a crossover random field domain state (RFDS), for materials which behave as SSG at low temperatures and SFM at higher temperatures [42]. The interaction strength between nanoparticles can be controlled by various factors like size, inter-particle distance, presence or absence of surfactant layers, nature of embedding matrix, magnetic field, temperature, etc. Extensive studies based on magnetic

relaxation, ac susceptibility, and magnetic imaging have been performed to identify and characterize the above mentioned „supermagnetic" states [43].

2.13 Theory of manganites

After long attention to the field of superconductivity, the flow of research interest switched towards the studies on manganite materials owing to their potential applicability for various purposes. Manganites exhibit variety of interesting novel properties like, insulator to metal (I-M) transition, paramagnetic to ferromagnetic transition, Colossal Magnetoresistance (CMR) effect etc. Manganite is a mineral, its composition is mainly MnO. These manganese based oxide materials, known as manganite, possess unique intrinsic properties of change in electrical resistance under the application of magnetic field, known as magnetoressistance. The doped $T_{1-x}D_xMnO_3$ type or better known as ABO_3 type perovskite structure has cubic unit cell, where Ln represents the rare earth elements [44]. At the corner, Mn ions are surrounded by octahedral oxygen units known as the MnO_6 octahedral.
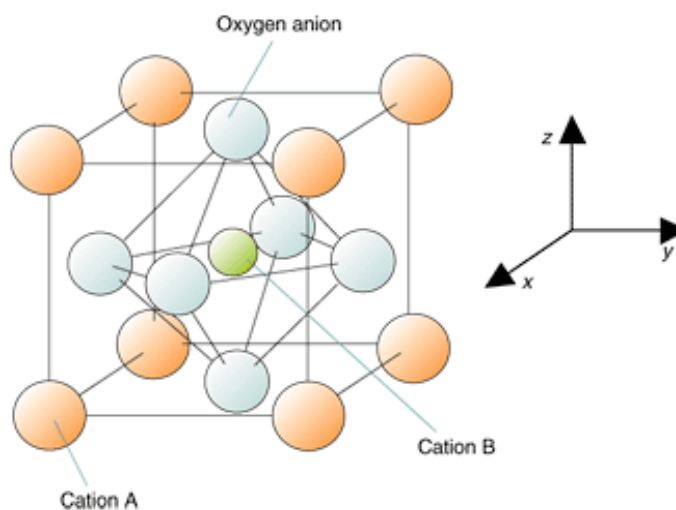
Figure 2.13: Schematic diagram of perovskite (ABO_3) type structure of manganites.

The relative ion size requirements for stability of the cubic structures are quite stringent, so slight buckling and distortion of MnO_6 octahedral can produce several low-Symmetry distorted structures, in which co-ordinate number of T cations and Mn or both is reduced. Complex perovskites structures contain two different Mn-sites cations (Mn^{3+} and Mn^{4+}) [44]. This results in possibility of ordered and disordered structures. The

orthorhombic and tetragonal phases are most commonly observed non-cubic structure for doped manganite.

2.14 History of Manganites

About half a decade ago Jonker and Santen (1950) [45-47] described the preparation of polycrystalline samples of $(La,Ca)MnO_3$, $(La,Sr)MnO_3$ and $(La,Ba)MnO_3$ manganites and reported ferromagnetism and anomalies in the conductivity at the Curie temperature with variation in lattice parameter as a function of hole doping. Few years later Volger observed a notable decrease of resistivity for $La_{0.8}Sr_{0.2}MnO_3$ in FM state, in applied magnetic fields [48]. Soon after a significant research effort have started on the studies of low temperature measurement in manganites such as specific heat, magnetization, dc and ac resistivity, magnetoresistance, magnetostriction, I-V curves, dielectric constant, Seebeck effect and Hall effect [48,49].

After those pioneering experiments, Wollan and Koehler (1955) [50] carried out extensive neutron diffraction study to characterize and draw the first magnetic structures of $La_{1-x}Ca_xMnO_3$ in the entire composition range. Wollan and Koehler (1955) were among the first to use the technique of neutron scattering to study magnetism in materials. They found that in addition to FM phase many other interesting anti-ferromagnetic phases were also present in manganites. Among them the most exotic spin arrangement is the CE-type state, which following their classification is a mixture of the C-phase with the E-phase. This CE-state was the first evidence of charge-ordering and mixed phase (phase separation) tendencies in the manganites. Further progress come somewhat later when the group at Manitoba grew a high quality mm long single crystal of another interesting manganites $(La,Pb)MnO_3$, which has a Curie temperature well above room temperature [51-53]. Jirak et al. (1979) [54] and Pollert et al. (1982) [55] studied the structure and magnetic properties of another very popular manganites $(Pr,Ca)MnO_3$ by X-ray and neutron diffraction technique. They observed charge-ordering phases which are totally different from the ferromagnetic phases of other manganites.

A burst of research activity on manganites started during 1990 because of the observation of large magnetoresistance. Work by Kusters et al. (1989) [56] on bulk

$Nd_{0.5}Pb_{0.5}MnO_3$ reveals the large MR effect. Another work by von Helmholtz et al. (1993) [57] on thin films of $La_{2/3}Ba_{1/3}MnO_3$ also revealed a large MR effect at room temperature. Thereafter similar conclusion was reached by Chahara et al. (1993) [58] using thin films of $La_{3/4}Ca_{1/4}MnO_3$ and Ju *et al*. (1994) [59] for films of $La_{1-x}Sr_xMnO_3$. They all observed MR values larger than those observed in artificially engineered multilayers (GMR) [60]. A defining moment for the field of manganites was the publication by Jin et al. (1993) [61] of results with truly Colossal Magnetoresistance (CMR). Jin et al. reported MR ((R_H-R_0)x100/R_H) close to 1500% at 200K and over 100,000% at 77K for thin films of $La_{0.67}Ca_{0.33}MnO_3$. This enormous factor corresponds to thousand-fold change in resistivity with and without the field. One year later Xiong *et al*. (1995) [62] reported MR ratio of over 100,000% using thin films of $Nd_{0.7}Sr_{0.3}MnO_3$ near 60K and in the presence of magnetic field of 8T. These studies led to the obvious conclusion that manganites were a potential alternative for „Giant" MR systems.

2.15   Origin of magnetoresistance in manganite perovskite

2.15.1 The structural and magnetic properties of $T_{1-x}A_xMnO_3$ perovskite

The physics of manganites is very rich. Manganites exhibit a variety of phases such as paramagnetic state, ferromagnetic metal or insulator, antiferromagnetism, canted antiferromagnetism and charge ordering. Several interesting phenomena including the colossal MR are related to the metal-insulator and magnetic transitions between these phases. Many properties of CMR materials can be tuned by external parameters such as temperature T, magnetic field H or by the chemical pressure. Many striking electronic properties of these systems are due to strong coupling of electrons to the dynamical lattice distortions. The lattice is the crystal cell of the perovskite type.

An undoped lanthanum manganite ($LaMnO_3$) compound corresponds to the ionic composition is $La^{+3}, Mn^{+3}, O_3^{-2}$. The electronic configuration of Mn atom is $3d^5 4s^2$, which means that the ionized Mn^{+3} has 4d-electrons, which are responsible for its electronic properties. The Jahn-Teller distortion is taking place at Mn^{+3} ion and plays significant role in the Metal-Insulator transition and ferromagnetic to paramagnetic transition. Jahn-Teller (J-T) effect has been described later in this chapter. If we substitute all trivalent

rare earth La atoms by a divalent metal such as Ca, we will obtain compound such as $Ca^{+2}Mn^{+4}O_3$ with Mn valence +4. Thus, the Mn ion in the $CaMnO_3$ compound will have 3-d electrons. This compound also has the perovskite structure. Both the perovskites, $LaMnO_3$ and $CaMnO_3$, are AFM insulator with ferromagnetic (FM) n-planes of alternating spin direction [63, 64]. For partial substitutions of La system such as $La_{1-x}A_xMnO_3$ (0<x<1), Mn ions are mixed valent and average number of d-electrons at the Mn-site is 4-x. An exciting thing is that, although pure La and pure Ca manganites are AFM insulators, the intermediate composition $La_{1-x}A_xMnO_3$ exhibits strong magnetism over a broad range of carrier concentrations and temperatures [63, 65].

2.15.2 Zener double-exchange mechanism

It has reported that the lattice distortion brings down T_c by use of hole doping at Ln-site (A-site). Hence T_c can be tuned by changing hole doping concentration and size of ionic radius of divalent cation. Below T_c, the manganites exhibit metal-type conductivity, and ferromagnetism around T_c. These behaviors are explained by Zener's double exchange mechanism [66]. The basic mechanism in this process is, the doping of a d-hole from Mn^{+4} or electron doping from d-shell of Mn^{+3} to Mn^{+4} like Mn^{+3} to Mn^{+4} via the oxygen, so that the Mn^{+3} and Mn^{+4} ions change places [66, 67].

$$Mn^{+3} \ O^{+2} \ Mn^{+4} \ ---- \ Mn^{+4} \ O^{+2} \ Mn^{+3}$$
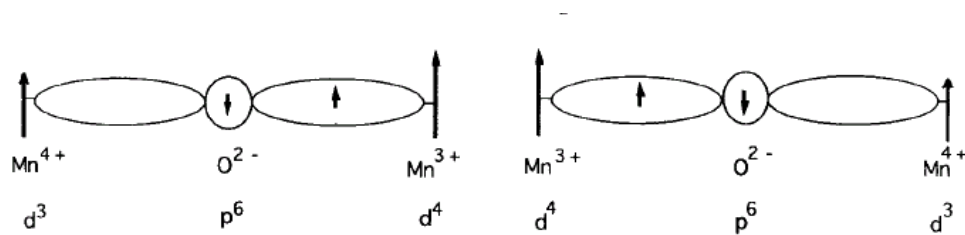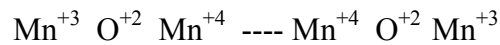
Figure 2.14: Schematic diagram of Zener Double Exchange mechanism

This creates the transfer of an electron from the Mn^{+3} site to the Central Oxide ion and simultaneously the transfer of an electron from the oxide ion to the Mn^{+4} site. Such a transfer is referred to as double-exchange (DE) [65].

2.15.3 Various mechanisms and properties of manganite perovskites

(a) Jahn-Teller (JT) effect

The rare-earth manganites such as $LaMnO_3$, $PrMnO_3$ and $NdMnO_3$, without hole doping are insulators at all temperatures as a consequence of crystal field at the cation sites in the perovskite structure. In the ideal structure, both A and B sites have cubic point symmetry 3 m [64]. However, in the real distorted structure, the point symmetry is much lower. These oxides undergo an antiferromagnetic (AFM) transition with $T_N \sim 150$ K. The AFM ordering is of A-Type [63, 65]. The Jahn-Teller distortion around Mn^{+3} ions is related to the insulating nature of the compounds and anisotropic magnetic interaction in the structure.

The structure plays a crucial role in determining the electric transport and magnetic transport properties of these oxides. Because when these parent systems are partly substituted by divalent ions at Ln site they became hole-doped. The Mn^{+4} content increase resulting into decreasing (JT) distortion.

The perovskite structure has an orthorhombic distortion (b>a>c/√2) and unit cell consisting of 4-formula units can be mapped into Pbnm or Pnma Symmetry.

(b) Tolerance factor

It has been clearly shown experimentally that for a fixed hole concentration, the properties of manganites strongly depends on a geometrical quantity known as "tolerance factor" [68, 69], defined by $t = d_{A-o}/(\sqrt{2}d_{Mn-o})$ here A-0 is the distance between A site, where the trivalent or divalent non-Mn ions are located, to the nearest oxygen. A ion is at the center of a cube with Mn in the vertices and O in between the Mn ions. d_{Mn}-o is the Mn-O shortest distance. Since for an undistorted cube with a straight Mn-O-Mn link, $d_{A-o} = \sqrt{2}$ and $d_{Mn-o} = 1$ in units of the Mn-O distance, the t=1 for the perfect system. However, sometimes the A ions are too small to fill the space in the cube centers and for this reason the oxygen tend to move toward the center, reducing d_{A-o}. In general d_{Mn-o} also changes at the same time. For this reason, the tolerance factor becomes less than unity t<1, [63,65] and Mn-O-Mn angle becomes smaller than 180°. The hopping amplitude for carriers to move from Mn to Mn naturally decreases as $\theta < 180^o$. As the tolerance factor decrease,

the charge localization increases due to the reduction in the mobility of the carriers. If the tolerance factor is reduced (t<1) then Mn-Mn distance is also reduced. Therefore, it would be expected that having closer Mn-ions result into an increase the electron hopping between them. The factors affecting most of its physical properties include $<r_A>$ = the Average A site ionic radii, t = tolerance factor is an indicator for the stability and distortion of crystal structure,

$$t = \frac{r_A + r_0}{\sqrt{2}(r_B + r_0)}$$ (2.33)

Where r_A is the radius of A cation, r_B is the radius of B cation, r_0 is the radius of anion respectively.

A detailed study on different $Ln_{0.7}A_{0.3}MnO_3$ compounds for a variety of Ln and A ions for the dependence of T_c on tolerance factor (t) shows the presence of three dominant regimes (1) a paramagnetic insulator at high-temperature, (2) a low temperature
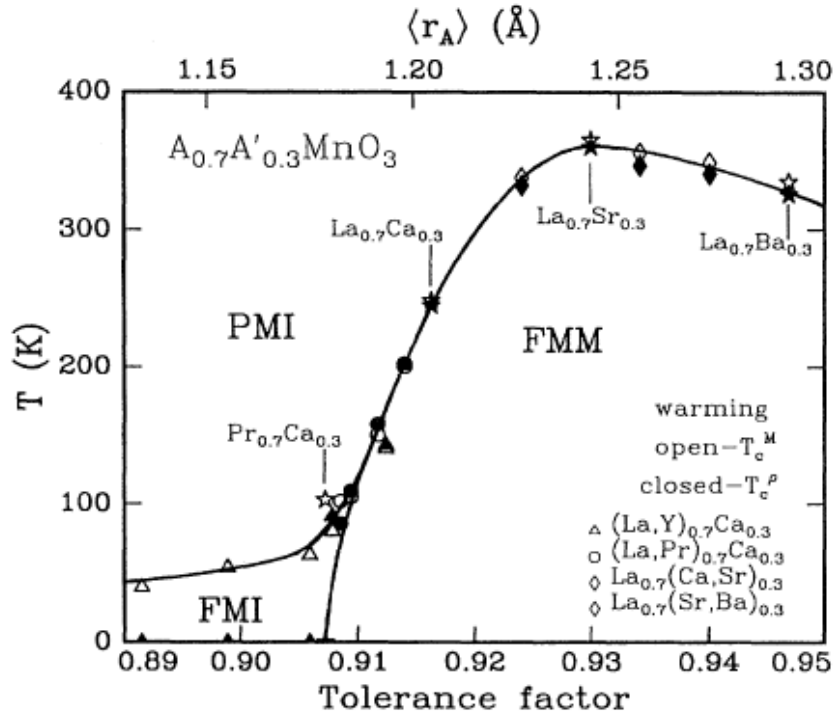
Figure 2.15: Variation of T_c with tolerance factor (t) and average cation radius $<r_A>$.

ferromagnetic metal at large tolerance factor, and (3) low –temperature charge-ordered ferromagnetic insulator at small tolerance factor fig. 2.19 [70]. The properties of doped manganites are highly dependent on the tolerance factor (t).

(c)   Electron-Lattice coupling

The structural and electronic properties of the perovskite crystal clearly have an important effect on Curie temperature and magnetoresistance. However, interaction between the charge carriers and vibrations of the crystal lattice say "phonons" also play a crucial and fundamental role in changing the resistance as the temperature falls towards the Curie temperature, of particular importance are the vibrations of lighter oxygen ions, which push electron towards vacant states in the manganese ion. This strengthens the Jahn-Teller effect and induces a local distortion of the lattice. Such a distortion is known as a "polaron" and leads to self-trapping of the (it can be a source of the high resistivity) charge carriers above the Curie temperature. Below the Curie temperature the selftrapping disappears because the bandwidth broadens and the electrons are much more mobile [71]. CMR effect is observed over a wide range of compositions of $La_{1-x}Ca_xMnO_3$(x<0.5), but the when x~0.2, a local structural distortion occurs from the strong electron-lattice polarons which arises from the strong electron-lattice coupling [64, 65]. But the significant changes in the local structure in the x~0.3 composition in the 80-300k range are observed which are attributed to the formation of small polarons due to the John-Teller distortion when T>Tc, [72, 73] these studies have shown that small polarons delocalized as the magnetization increases in the manganite which induces the IM transition.

(d) Insulator-Metal (I-M) and paramagnetic–ferromagnetic (PM-FM) transition
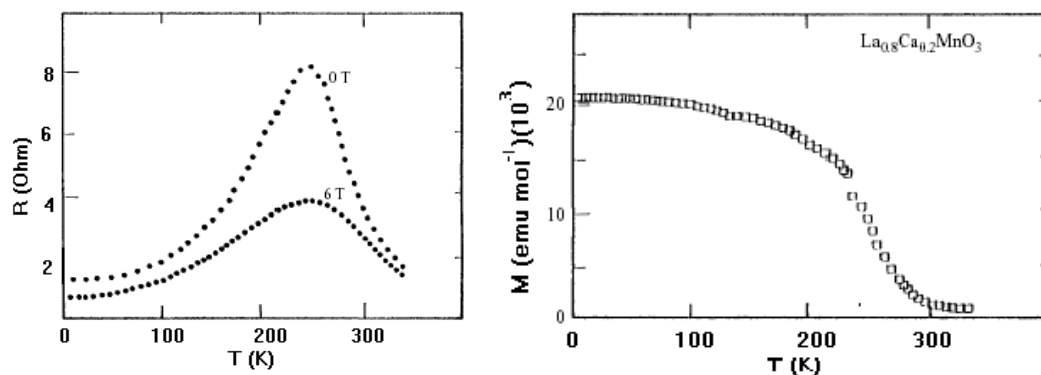
Figure 2.16: (a) & (b) Metal-insulator transition and Paramagnetic-Ferromagnetic transition,in $La_{1-x}Ca_xMnO_3$ [64].

In addition to various phenomenon described above, (M-I) the metal-insulator and paramagnetic to ferromagnetic transition (PM-FM) take place in $LaMnO_3$ perovskite with an orthorhombic structure ith small proportion of Mn^{+4} (< 5%), becoming antiferromagnetically ordered below $T_N \sim 150$ K. In $LaMnO_3$ if La^{+3} is progressively substituted by a divalent cation, the formula becomes $Ln_{1-x}A_xMnO_3$ (Ln=La,Nd,Sm,Pr and A=Ca,Sr,Ba, Pb..). Systematic investigations show that an empirical relationship exists between electrical conductivity and magnetism [64]. With increase in x (Mn^{+4} Content), the manganites become ferromagnetic, with well-defined curie temperatures T_c and around T_c, it exhibits metal-like conductivity as shown in fig. 2.16(a) & 2.16(b). The simultaneous observations of I-M and PM-FM transitions are explained by the Zener double exchange mechanism. A metal is in the ferromagnetic phase, whose resistivity decreases as the magnetization increases below T_c. So the ferromagnetism is always coupled with metallic phase in the system.

(e) Role of ionic radii at A-site

The ionic radii at A-site play an important role in modifying the electrical and magnetic transport properties of manganite.
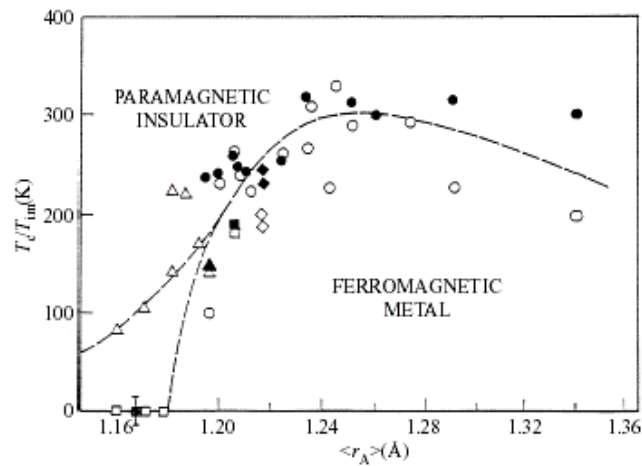
Figure 2.17: Ionic radius at A-site $<r_A>$ vs. T_c/T_{im} [74-77]

As divalent cation is introduced at A-site, the ionic radii becomes mixture of Ln= rare earth trivalent and A= divalent cation which is named as average A-site ionic radius ($<r_A>$). The modification in the tolerance factor „f" alters the transition temperature and

41

desired transport properties of manganites can be achieved. The fig. 2.17 shows the variation in transition temperature with average ionic radius $<r_A>$ of A-site . The transition temperature is highest when $<r_A> \sim 1.23$Å which corresponds to a tolerance factor of 0.93. It may be also noticed thaht increase in $<r_A>$ the e_g band with increases and MR% decreases [76, 77].

(f)   Charge and Orbital Ordering

The charge order, also known as Wigner Crystallization, is driven by inter atomic coulomb interaction. The mobile d electrons can be localized on certain manganese ions to form a regular lattice for particular occupancies of the d band, provided that inter electronic coulomb interaction is comparable with the conduction-electron bandwidth W [78]. The effect is accentuated by small displacements of the oxygen atoms to accommodate the ordered cation lattice. Charge ordering most likely occurs when the temperature is low and x is a rational fraction especially x= 1/8 or 3/4. The extra fourth d electron may then be delocalized on alternate manganese site in a plane, as shown in fig. 2.18 (a). The carriers in mixed valent manganites may be strongly coupled to local lattice distortion [79]. Orbital ordering can occur at certain carrier density when the d electrons occupy an asymmetric orbital as shown in fig. 2.18 (b). The driving source is partly direct electrostatic repulsion of the charge. Adjacent octahedral stabilize the effect. Figure 2.18 (c) displays the combined effect of charge and orbital order in mixed valent manganites when the doping concentration is x=1/2.
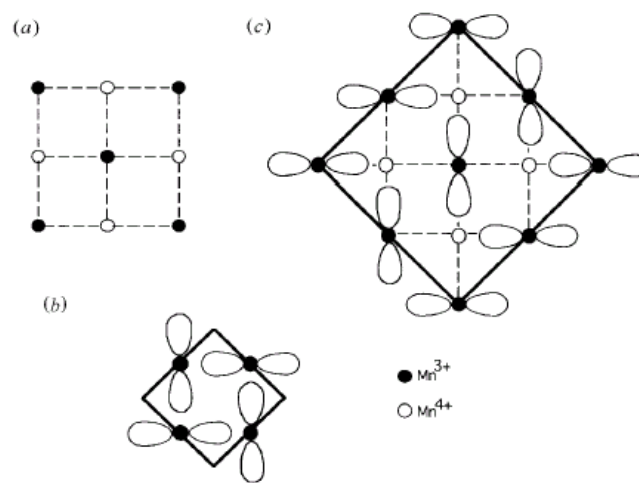
Figure 2.18: (a) charge ordering (b) orbital ordering (c) charge and orbital ordering.

2.16   Applications

The CMR materials have good potential for device applications. Several groups have attempted to explore the transport properties, specially half metallicity and transition from insulating to metallic region in the CMR materials for their applications in various devices [80-82]. In brief, the general applications of the CMR materials have been discussed as follows.

2.16.1 CMR materials as Sensor & devices

(a)   Magnetic Sensor

Using the CMR effect in thin films, numbers of efforts have been made to fabricate magnetic sensors. For magnetic field sensing applications, low field response at or above the room temperature, the researchers have used the defects or grain boundary effects in microstructure of the manganites [81,82]. The low field sensitivity is due to spin polarized tunneling between two grains [83-85]. The idea of development of heterostructure is more prominent, which show low field sensitivity at room temperature [86].

The industrial requirements of magnetic sensors using CMR materials should follow the following properties.

1) Operating at or above room temperature.

2) At least 20% response at a field of ≤ 100 Oe

3) Temperature independent MR value over 300 ± 50 K.

4) Acceptable noise values.

5) The dimensions of film approaching 1000 Å or less than that.

b) Microwave CMR Sensor

At microwave frequencies, significant CMR effect has been observed as compared to a low frequency [87]. For the microwave cavity in the anti-resonant mode, a very large CMR effect is seen ~ 50 % at very low field which suggests the possible microwave devices.

(c) Spin valve devices

The spin valve device consists of two ferromagnetic electrodes separated by a nonmagnetic conducting layer [88]. In general, the lower electrode has a large coercive field than the upper electrode. The entire device structure consists of epitaxial multilayer of CMR ferromagnetic electrodes separated by an epitaxial layer of conducting materials. However, devices made using this concept have large series resistance, which cannot be explained on the basis of the resistivity of individual layers and this reduces the observed MR. An alternate approach is the trilayer spin tunneling device, where the intermediate layer is an epitaxial insulator. This type of device shows large low-field MR, about factor of two to five, in a field around 100 Oe at 4.2 K.

(d) Field effect devices

The field effect transistor (FET) device structure consists of epitaxial multilayer of CMR ferromagnetic layers at the bottom and dielectric layers on the top. This device structure shows some interesting characteristics depending on the dielectric layer on top as to whether it is a para-electric layer such as STO, or a ferroelectric PZT [89].

(e) Bolometric Sensor

Due to the large temperature co-efficient of resistance (TCR) in CMR materials, their application as bolometer device is possible [90,91]. The CMR materials exhibits I-M transition at T_c and sharp drop of the resistance at transition temperature gives large TCR. The merit of the bolometric device is the TCR and noise volume. The commercial bolometer is based on VO_x, having TCR values around 2.5 to 4%. As compared to VO_x, the TCR values increases from 8 to 18 % in CMR materials. Ravi bathe et al showed 23% TCR in LCMO thin film with silver ion implantation [92].

f) Spin Polarized injection devices

At low temperatures <100 K, CMR materials show some interesting properties and is found to be advantageous to integrate them with HTSC. A heterostructure consisting of HTSC/CMR has been used for magnetic flux focused devices [93]. The

Meissner effect of the superconductor can be used as magnetic lens to enhance the flux coupling to a CMR detector thereby enhancing its sensitivity. And spin polarized electrons are injected from CMR layer into the superconducting channel [94, 95].

References:

[1]   Weller, D. and Moser, A., "Thermal effect limits in ultrahigh-density magnetic recording", IEEE Transactions on Magnetics, 35, 6, 4423–4439, 1999.

[2]   Cullity, B. D., Introduction to Magnetic Materials, Addison-Wisley Publishing Company, Inc., California,1972.

[3]   Valenzuela, R., Magnetic Ceramics, Cambridge University Press, Cambridge, 1994.

[4]   Callister, W., "Materials Science and Engineering an introduction", Sixth Ed. New York: JoHn Wiley & Sons, Inc, 2003.

[5]   Raghavan, V., "Materials Science and Engineering" (PHI Learning Private Limited Fifth Edition, 2010).

[6]   Goldman, A., "Modern Ferrite Technology", 1990.

[7]   Chikazumi, S., "Physics of Ferromagnetism" (Oxford Science Publications), 276, 1997.

[8]   McGrouther, D., "Effects of Focused Ion Beam Irradiation on Thin Ferromagnetic Films", PhD thesis, University of Glasgow, 2004.

[9]   Bozorth, R. M., "Ferromagnetism" (Van Nostrand Company, Princeton), 741,1951.

[10]   Takahashi, M., "Induced Magnetic Anisotropy of Evaporated Films Formed in a Magnetic Field", J. Appl. Phys., 33, 3, 1101-1106, 1962.

[11]   Jiles, D., "Introduction to magnetism and magnetic materials", 2nd ed. Chapman and Hall, 1998.

[12]   Cullity, B. D. & Graham, C. D., "Introduction to Magnetic Materials", Wiley, 2009.

[13]   Hamrle, J., Blomeier, S., Gaier, O., Hillebrands, B., Schafer, R. and Jourdan. M., "Magnetic anisotropies and magnetization reversal of the $Co_2Cr_{0.6}fe_{0.4}$ Al heusler compound", J. Appl. Phys, 100, 10, 103904, 2006.

[14]   Crangle, J., "Solid-State Magnetism", Van Nostrand Reinhold, 1991.

[15]   Basith, M. A., Manjura Hoque, Sk., Shahparan, Md., Hakim ,M. A., Huq, M., "Temperature features of magnetoresistance of layered manganite $La_2Sm_{0.4}Sr_{0.6}Mn_2O_7$", Physica B, 395, 126–129, 2007.

[16]   Jin, S., Tiefel, T. H., MeCormak, M., Fastnacht, R. A., Ramesh, R., and Chen, L. H., "Thousand fold change in resistivity in magnetoresistive La-Ca-Mn-O films", Science, 264, 413-415, 1992.

[17]   Goldman, A., Handbook of Modern Ferromagnetic Materials, Kulwer Acad. Pub, Boston, U.S.A, 1999.

[18]   Crespilho, F.N., Lima, F.C.A., da Silva, A.B.F., Oliveira Jr, O.N., Zucolotto, V., "The origin of the molecular interaction between amino acids and gold nanoparticles: A theoretical and experimental investigation", Chem. Phys. Lett., 469, 186, 2009.

[19]   Endo, T., Kerman, K., Nagatani, N., Tamiya, E., "Excitation of localized surface plasmon resonance using a core–shell structured nanoparticle layer substrate and its application for label-free detection of biomolecular interactions", J. Phys. Condens. Matter 19, 7215201, 2007.

[20]   Zhang, X., Young, M.A., Lyandres, O., Van Duyne, R.P., "Rapid detection of an anthrax biomarker by surface-enhanced raman spectroscopy", J. Am. Chem. Soc.,127, 4484, 2005.

[21]   Maxwell, D.J., Taylor, J.R., Nie, S., "Self-assembled nanoparticle probes for recognition and detection of biomolecules", J. Am. Chem. Soc., 124, 9606, 2002.

[22]   Lee, P.C., Meisel, D., "Adsorption and surface-enhanced raman of dyes on silver and gold sols", J. Phys. Chem., 86 3391, 1982.

[23]   Storhoff, J.J., Lazarides, A.A., Mucic, R.C., Mirkin, C.A., Letsinger, R.L., Schatz, G.C., "What controls the optical properties of DNA-linked gold nanoparticle assemblies?", J. Am. Chem. Soc., 122, 4640, 2000.

[24]   Taton, T.A., Mirkin, C.A., Letsinger, R.L., "Scanometric DNA array detection with nanoparticle probes", Science, 289, 1757, 2000.

[25]   Eustis, S., El-Sayed, M.A., "Why gold nanoparticles are more precious than pretty gold: Noble metal surface plasmon resonance and its enhancement of the radiative and nonradiative properties of nanocrystals of different shapes", Chem. Soc. Rev., 35, 209, 2006

[26]   Chikazumi, S., Taketomi, S., Ukita, M., Mizukami, M., Miyajima, H., Setogawa, M., Kurihara, Y., "Physics of magnetic fluids", J. Magn. Magn. Mater., 65, 245. 1987.

[27]   Lu, A.-H., Schmidt, W., Matoussevitch, N., Bönnemann, H., Spliethoff, B., Tesche, B., Bill, E., Kiefer, W., Schüth, F., "Nanoengineering of a magnetically separable hydrogenation catalyst", Angew. Chem. Int. Ed., 43, 4303, 2004.

[28]   Gupta, A.K., Gupta, M., "Synthesis and surface engineering of iron oxide nanoparticles for biomedical applications", Biomaterials, 26, 3995, 2005.

[29]   Li, Z., Wei, L., Gao, M.Y., Lei, H., "One-pot reaction to synthesize biocompatible magnetite nanoparticles", Adv. Mater., 17, 1001, 2005.

[30]   Hyeon, T., "Chemical synthesis of magnetic nanoparticles", Chem. Commun., 927, 2003.

[31]   Takafuji, M., Ide, S., Ihara, H., Xu, Z., "Preparation of poly(1-vinylimidazole)-grafted magnetic nanoparticles and their application for removal of metal ions", Chem. Mater., 16, 1977, 2004.

[32]   Scheinfein, M. R., Schmidt, K. E., Heim, K. R., and Hembree, G. G., "Magnetic Order in Two-Dimensional Arrays of Nanometer-Sized Superparamagnets", Physical Review Letters, 76, 1541, 1996.

[33]   Ruderman, M. A., and Kittel, C., "Indirect Exchange Coupling of Nuclear Magnetic Moments by Conduction Electrons", Physical Review, 96, 1 99, 1954.

[34]   Edwards, S. F. and Anderson, P. W., "Theory of spin glasses. II", Journal of Physics F: Metal Physics, 5, 965, 1975.

[35]   Parisi, G, "Infinite Number of Order Parameters for Spin-Glasses", Physical Review Letters, 43, 1754, 1979.

[36]   Binder, K., and Young, A. P., "Nonanalytic magnetic field dependence of the magnetisation in spin glasses", Reviews of Modern Physics, 58, 801, 23, 1986.

[37]   Blugel, S., "Magnetism of 4d and 5d transition metal adlayers on Ag(001): Dependence on the adlayer thickness", Physical Review B, 51, 3 2025, 1995.

[38]   Jaffari, G. H., Ali, S. R., Hasanain, S. K., Guentherodt, G., and Shah, S. I., "Stabilization of surface spin glass behavior in core-shell Fe67Co33–CoFe2O4 nanoparticles", Journal of Applied Physics, 108, 063921, 2010.

[39]   Nadeem, K., Krenn, H., Traussing, T., and Letofsky-Papst, I., "Distinguishing magnetic blocking and surface spin-glass freezing in nickel ferrite nanoparticles", Journal of Applied Physics, 109, 013912, 2011.

[40]   Xu, M., Zhong, W., Yu, J., Zang, W., Au, C., Yang, Z., Lv, L. and Du, Y., "Exchange bias-like behavior from disordered surface spins in $Li_4Mn_5O_{12}$ nanosticks", Journal of Physical Chemistry C, 114, 16143, 2010.

[41]   Bedanta, S. and Kleemann, W., 2009 "Supermagnetism", Journal of Physics D: Applied Physics, 42, 013001, 2009.

[42]   Chen, X., Sahoo, S., Kleemann, W., Cardoso, S. and Freitas, P. P., "Universal and scaled relaxation of interacting magnetic nanoparticles", Physical Review B, 70 172411, 2004.

[43]   Petracic, O., Chen, X., Bedanta, S., Kleemann, W., Sahoo, S., Cardoso, S. and Freitas, P. P., Journal of Magnetism and Magnetic Materials 300, 1, 192, 2006.

[44]   Tokura, Y., "Fundamental features of colossal magnetoresistive manganese oxides", in Colossal Magnetoresistive oxides, Gordon and Breach Science publishers, 2000.

[45]   Jonker, G. H., and Van Santen, J. H., "Ferromagnetic compounds of manganese with perovskite structure", Physica, 16, 3, 337-349, 1950.

[46]   Van Santen, J. H. and Jonker, G. H., "Electrical conductivity of ferromagnetic compounds of manganese with perovskite structure", Physica, 16, 599-600, 1950.

[47]   Jonker, G. H. and Van Santen, J. H., "Magnetic compounds wtth perovskite structure III. ferromagnetic compounds of cobalt"J., Physica, 19, 1-12, 120-130, 1953.

[48]   Volger, J., "Further experimental investigations on some ferromagnetic oxidic compounds of manganese with perovskite structure", Physica, 20, 1-6, 49-66, 1954.

[49]   Jonker, G. H., "Semiconducting properties of mixed crystal with perovskite structure", Physica, 20, 1118-1122, 1954.

[50]   Wollan, E. O. and Koehler, W. C., "Neutron Diffraction Study of the Magnetic Properties of the Series of Perovskite-Type Compounds [(1−x)La, xCa] MnO_3", Phys Rev, 100, 2, 545, 1955.

[51]   Moorish, A. H., Evans, B. J., Eaton, J. A. and Leung, L. K., "Ionic ferromagnet (La,Pb)MnO$_3$. I. Growth and characteristics of single crystals", Can. J. Phys., 47, 2691-6, 1969.

[52]   Leung, L. K., Moorish, A. H. and Searle, C. W., "Possible Evidence for a Coupling Between Elastic and Magnetic Exchange Forces", Can J Phys, 47, 2697, 1969.

[53]   Searle, C. W., and Wang, S. T., "Studies of the ionic ferromagnet (LaPb)MnO$_3$. V. Electric transport and ferromagnetic properties", Can J Phys, 48, 17, 2023-2031, 1970.

[54]   Jirak, Z., Vratislav, S. and Zajicek, J., "The Magnetic Structure of Pr$_{0.9}$Ca$_{0.1}$MnO$_3$", Phys. Stat. Sol., 52, 1, 39-43, 1979.

[55]   Pollert, E., Krupicka, S. and Kuzmicova, E., "Structural study of Pr$_{1-x}$Ca$_x$MnO$_3$ and Y$_{1-x}$Ca$_x$MnO$_3$ perovskite", J. Phys. Chem. Solids, 43, 12, 1137-1145, 1982.

[56]   Kusters, R. M., Singleton, J., Keen, D. A., McGreevy, R., and Hayes, W., "Mgnetoresistance measurements on the magnetic semiconductor NdPbMnO$_3$", Physica B, 115, 1-3, 362-365, 1989.

[57]   von Helmholtz, R., Wecker, J., Holzapfel, B., Schultz, L. and Samwer, K., "Giant negative magnetoresistance in perovskitelike La$_{2/3}$Ba$_{1/3}$MnO$_x$ ferromagnetic-films", Phys. Rev. Lett., 71, 2331, 1993.

[58]   Chahara, K., Ohno, T., Kasai, M. and Kozond, Y., "Magnetoresistance in magnetic manganese oxide with intrinsic antiferromagnetic spin structure", Appl. Phys. Lett., 63, 1990.

[59]   Ju, H. L., Kown, C., Li, Q., Green, R. L. and Venkatesan, T., "Giant magnetoresistance in La$_{1-x}$Sr$_x$MnO$_z$ films near room temperature", Appl. Phys. Lett., 65, 2108-2110, 1994.

[60]   Parkin, S. S. P., "Giant magnetoresistance in magnetic nanostructures", Annu. Rev. Mater. Sci., 25, 357-388, 1995.

[61]   Jin, S., Tiefel, T. H., McCormack, M., Fastnacht, R. A., Ramesh, R. and Chen, L. H., "Thousandfold change in resistivity in magnetoresistive La-Ca-Mn-O films", Science, 264, 5157, 413-415, 1994.

[62]   Xiong, G. C., Bhagat, S. M., Li, Q., Ju, H. L., Lofland, S. E., Greene, R. L. and Venkatesan, T., "Giant magnetomemory effect of epitaxial $Nd_{0.7}Sr_{0.3}MnO_3$ films", Appl. Phys. Lett., 67, 20, 3031-3033, 1995.

[63]   Goodenough, J. B., "Electronic and ionic transport properties and other physical aspects of perovskites", Rep. Prog. Phys., 67, 11, 1915-1993, 2004.

[64]   Coey, J. M. D., Viret, M., "Mixed-valence manganites", Advances in Physics, 48, 2, 167-293, 1999.

[65]   Rao, C. N. R., Raveau, B., Colossol Magnetoresistance, Charge Ordering and related properties of Manganese Oxides, World Scientific Publishing Co. Pte. Ltd, 1998.

[66]   Zener, C., "Interaction between the d-Shells in the Transition Metals. II. Ferromagnetic Compounds of Manganese with Perovskite Structure", Phys. Rev., 82, 403, 1951.

[67]   Solovyev, I., Hamada, N., Terakura, K., "Crucial role of the lattice distortion in the magnetism of $LaMnO_3$", Phys. Rev. Lett., 76, 25, 4825-4828, 1996.

[68]   Mahesh, R., Mahendiran, R., Raychaudhuri, A. K. and Rao, C.N.R., "Giant magnetoresistance in bulk samples of $La_{1-x}A_xMnO_3$ (A= Sr or Ca)", J. Solid State Chem., 114, 1, 297-299, 1995.

[69]   Zener, C., "Interaction between the d-Shells in the Transition Metals. II. Ferromagnetic Compounds of Manganese with Perovskite Structure", Phys. Rev., 82, 403, 1951.

[70]   Hwang, H. Y., Cheong, S. W., Radaelli, P. G., Marezio, M. and Batlogg, B., "Lattice Effects on the Magnetoresistance in Doped $LaMnO_3$", Phys. Rev. Lett., 75, 914, 1995.

[71]   Dagotto, E., Hotta, T., Moreo, A., "Colossal magnetoresistant materials: the key role of phase separation", Physics Report, 344, 1, 1-153, 2001.

[72]   Billinge, S. J. L., DiFrancesco, R. G., Kwei, G. H., Neumeier, J. J. and. Thompson, J. D., "Direct Observation of Lattice Polaron Formation in the Local Structure of $La_{1-x}Ca_xMnO_3$", Phys. Rev. Lett., 77, 715, 1996.

[73]   Tyson, T. A., Mustere de Leon, J., Conradson, S. D., Bishop, A. R., Neumeier, J. J., Roder, H. and Zang, J., "Evidence for a local lattice distortion in Ca-doped $LaMnO_3$", Phys. Rev. B., 53, 13, 985, 1996.

[74]   Reveau, B., Maignan, A. and Caignaert, V., "Spectacular GMR effects in the polycrystalline perovskite $Pr_{0.7}Sr_{0.05}Ca_{0.25}MnO_3$", J. Solid State Chem., 117, 424-426, 1995.

[75]   Fontcuberta, J., Martinez, B. Setfar, A. Pinol, S. Garcia-Munoz, J. L. and Ofraders, X., "The metal–insulator transition and ferromagnetism in the electron-doped layered manganites $La_{2.3-x}Y_xCa_{0.7}Mn_2O_7$ (x = 0, 0.3, 0.5)", Phys. Rev. Lett., 76, 1122, 1996.

[76]   Ibarra, M. R., Algarabel, P. A., Marquina, C., Blasco, J. and Garcia, J., "Large Magnetovolume Effect in Yttrium Doped La-Ca-Mn-O Perovskite", Phys. Rev. Lett., 75, 3541, 1995.

[77]   Mahendiran, R., Mahesh, R., Raychaudhuri, A. K., Rao, C. N. R., "Effect of Y substitution in La-Ca-Mn-O perovskites showing giant magnetoresistance" Phys. Rev. B., 53, 12160, 1996.

[78]   Cullen J. R. and Callan, E., "Green function theory of electron correlations above and below the Verwey transition in magnetite doped with impurities", Phys. Rev., 7, 397, 1973.

[79]   Kanamori, J., "Superexchange interaction and symmetry properties of electron orbitals", J. Phys. Chem. Solids., 10, 2-3, 87-98, 1959.

[80]   Sun, J. Z. and Gupta, A., Annu., "Spin-dependent transport and low-field magnnetoresistance in doped manganites", Rev. Mater. Sci., 28, 45-78, 1998.

[81]   Venkatesan, T., Rajeswari, M., Dong, Z. W., Ogale, S. B. and Ramesh, R., Phil, Trans, R. Soc., "Optical conductivity of manganites: Crossover from Jahn-Teller small polaron to coherent transport in the ferromagnetic state", Lond. A. 356, 1693, 1998.

[82]   Mathur, N. D., Burnell, G., Isaac, S. P., Jackson, T. J., Teo, B. S., MacManus-Dricoll, J. L., Cohen, L. F., Evetts, J. E. and Blamire, M. G., "Large low-field magnetoresistance in $La_{0.7}Ca_{0.3}MnO_3$ induced by artificial grain boundaries", Nature, 387, 266, 1997.

[83]   Sun, J. Z., Krusin - Elbaum, L., Duncombe, P. R., Gupta, A. and Laibowitwitzpal, R. B., "Temperature dependent, non-ohmic magnetoresistance in doped perovskite manganite trilayer junctions", Appl. Phys. Lett., 70, 1769-1771, 1997.

[84]   Hwang, H. Y., Cheong, S. W., Ong, N. P. and Batlog, B., "Spin-polarized intergrain tunneling in $La_{2/3}Sr_{1/3}MnO_3$", Phys. Rev. Lett., 77, 10, 2041, 1996.

[85]   Gupta, A., Gong, G. Q., Xiao, G., Duncombe, P. R., Leoeur, P., Trouilloud, P., Wang, Y. Y., Dravid, V. P. and Sun, J. Z., "Grain-boundary effects on the magnetoresistance properties of perovskite manganite films", Phys. Rev. B., 54, 46, 15629-15632, 1996.

[86]   Tokura, Y., "Colossal Magnetoresistive Oxides", Gordon and Breach Science Publishers, 2000.

[87]   Dominguez, M., Bhagat, S. M., Lofland, S. E., Ramchandran, J. S., Xiong, G. C., Ju, H. L., Venkatesan, T., and Greene, R. L., "Studies on the Magneto- Studies on the Magneto-transport properties of transport properties of perovskite based Colossal Magneto Resistance (CMR) materials", Euophys. Lett., 32, 349, 1995.

[88]   Diney, V., Sperious, V. S., Metin, S., Parkin, S. S., Gurney, B. A., Baumgart, H., and Wilhoit, D. R., "Magnetotransport properties of magnetically soft spin-valve structures" Appl. Phys. Lett., 69, 4774-4779, 1991.

[89]   Mathews, S., Ramesh, R., Venkatesan, T. and Benedetto, J., "Ferroelectric Field Effect Transistor Based on Epitaxial Perovskite Heterostructures", Science, 276, 5310, 238-240, 1997.

[90]   Goyal, A., Rajeswari, M., Shreekala, R., Lofland, S. E., Bhagat, S. M., Boettcher, T., Kwon, C., Ramesh, R. and Venkatesan, T., "Material characteristics of perovskite manganese oxide thin films for bolometric applications" Appl. Phys. Lett., 71, 17, 2535, 1997.

[91]   Rajeswari, M., Chen, C. H., Goyal, A., Kwon, C., Robson, M. C., Ramesh, R., Venkatesan, T. and Lakeou, S., "Low-frequency optical response in epitaxial thin films of $La_{0.67}Ca_{0.33}MnO_3$ exhibiting colossal magnetoresistance", Appl. Phys. Lett., 68, 25, 3555, 1996.

[92]   Bathe, R., Adhi, K. P., Patil, S. I., Marest, G., Honneyer, B. and Ogale, S. B., "Silver ion implantation in epitaxial $La_{2/3}Ca_{1/3}MnO_3$ thin films: Large temperature

coefficient of resistance (TCR) for bolometric applications", Appl. Phys. Lett., 76, 2104, 2000.

[93]   Dong. Z. W., Boehcher, T., Chen. C. H., Takeuchi, Rajeswari, M. and Venkatesan, T. T., "Enhanced magnetoresistance in $YBa_2Cu_3O_7/Nd_{0.7}Sr_{0.3}MnO_3$ heterostructures using magnetic flux focusing", Appl. Phys. Lett., 69, 3432, 1996.

[94]   Dong, Z. W., Ramesh, R., Venkatesan, T., Jackson, M., chen, Z. Y., Pai, S. P., Shreekala, R., Sharma, R. P., Lobb, C. J., And Grceen, R. L., "Spin-polarized quasiparticle injection devices using $Au/YBa_2Cu_3O_7/LaAlO_3/Nd_{0.7}Sr_{0.3}MnO_3$ heterostructures" Appl. Phys. Lett. 71, 1718, 1997.

[95]   Vasko, V. A., Larkin, V. A., Kraus, P. A., Nikolaev, K. R., Grupp, D. E., Nordman, C. A. and Goldman, A. M., "Critical Current Suppression in a Superconductor by Injection of Spin-Polarized Carriers from a Ferromagnet", Phys. Rev. Lett., 78, 1134, 1997.

CHAPTER 3
SAMPLE PREPARATION AND EXPERIMENTAL TECHNIQUES

3.1 Preparation of bulk polycrystalline sample

3.1.1 Solid state reaction technique:

There exist a wide variety of methods for the synthesis of polycrystalline materials. Out of them, the solid-state reaction method is the broadly used technique for the preparation of polycrystalline solids. In this method reactants are mixed together in a powder form and heated for extended periods at high temperature. High temperature provides a considerable amount of energy to accelerate the reaction rate. Hence, the final product obtained from this method is thermodynamically stable. The major benefit of this method is the formation of structurally single phase product with desired properties which depends on final sintering temperature. Flow chart of sample preparation is given bellow:

```
┌─────────────────────────────┐
│   Oxides of raw materials    │
└─────────────────────────────┘
              ↓
┌─────────────────────────────┐
│  Weighing of different mole  │
│          percentage          │
└─────────────────────────────┘
              ↓
┌─────────────────────────────┐
│   Dry mixing by agate mortar │
└─────────────────────────────┘
              ↓
┌─────────────────────────────┐
│ Weight mixing by hand milling│
└─────────────────────────────┘
              ↓
┌─────────────────────────────┐
│           Drying             │
└─────────────────────────────┘
              ↓
┌─────────────────────────────┐
│         Calcination          │
└─────────────────────────────┘
              ↓
┌─────────────────────────────┐
│         Hand Milling         │
└─────────────────────────────┘
              ↓
┌─────────────────────────────┐
│     Pressing to desired      │
│           pellets            │
└─────────────────────────────┘
              ↓
┌─────────────────────────────┐
│          Sintering           │
└─────────────────────────────┘
              ↓
┌─────────────────────────────┐
│        Final products        │
└─────────────────────────────┘
```
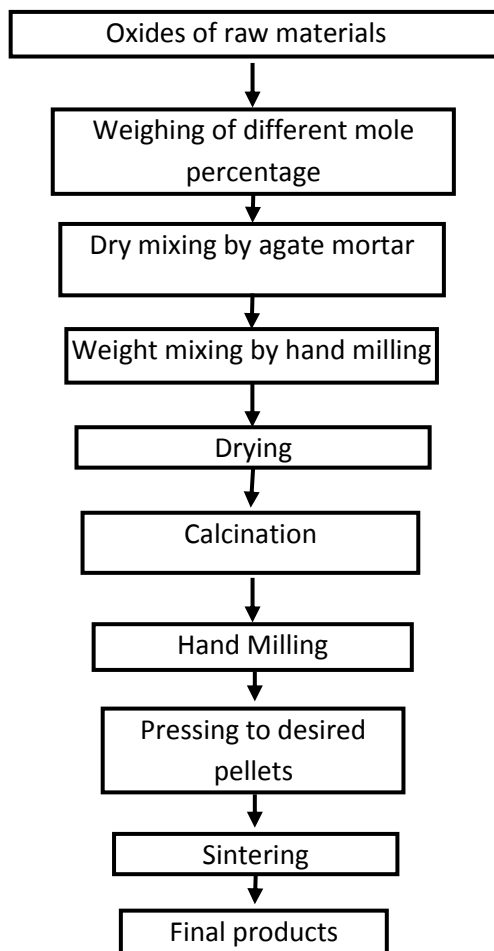
The detail process of Calcination, Pelletization and Sintering are given bellow

3.1.1.1 Calcination

Calcination is a thermal treatment process in presence of air applied to ores and other solid materials to bring about a thermal decomposition phase transition or removal of a volatile fraction. The calcination processes normally take place below the melting point of the product materials. Calcination is to be distinguished from roasting, in which more complex gas solid reaction take place between the furnace atmospheres of the solid.

The calcination reaction usually takes place at or above the thermal decomposition or transition temperature. This temperature is usually defined as the temperature at which the standard Gibbs free energy for a particular calcination reaction is zero [1].

The calcining process can be repeated several times to obtain a high degree of homogeneity. The calcined powders are crushed into fine powders. The ideal characteristics of fine powders are [2]:

1) small particle size (sub-micron)
2) narrow distribution in particle size
3) dispersed particles
4) equiaxed shape of particles
5) high purity
6) homogeneous composition.

A small particle size of the reactant powders provides a high contact surface area for initiation of the solid state reaction; diffusion paths are shorted, leading to more efficient completion of the reaction. Porosity is easily eliminated if the initial pores are very small. A narrow size distribution of spherical particles as well as a dispersed state is important for compaction of the powder during green-body formation. Grain growth during sintering can be better controlled if the initial size is small and uniform.

3.1.1.2 Pelletization

It is a process of pressing the powder in uni-axial hydraulic press at room temperature by applying a force on to accelerate the reaction rate. Here we have to increase the area of contact between the particles, this can be achieved by pressing the

reaction powder into pellets but even at high pressure the pellets are usually porous and the crystal contacts are not maximized. Typically cold pressed pellets are 20% to 40% porous. Depending upon requirement of our sample formation, sometimes hot press is required. So that the combined effect of temperature and pressing may cause the particle to fit together better but densification process is usually slow and may require several hours [3].

3.1.1.3 Sintering

Sintering is defined as the process of obtaining a dense, tough body by heating a compacted powder for a certain time at a temperature high enough to significantly promote diffusion, but clearly lower than the melting point of the main component. The driving force for sintering is the reduction in surface free energy of the powder. Part of this energy is transferred into interfacial energy (grain boundaries) in the resulting polycrystalline body [2, 4]. The sintering time, temperature and the furnace atmosphere play very important role on the dielectric, electric and magnetic properties of magnetic materials. The purposes of sintering process are:

1) to bind the particles together so as to impart sufficient strength to the product,

2) to densify the material by eliminating the pores and

3) to homogenize the materials by completing the reactions left unfinished in the calcining step.

Sintering of crystalline solids is dealt by Coble and Burke [5] who found the following empirical relationship regarding rate of grain growth:

$$\bar{d} = kt^n \tag{3.1}$$

where $\bar{d}$ is the mean grain diameter, n is about 1/3, t is sintering time and k is a temperature dependent parameter. Sintering is divided into three stages shown in fig. 3.1 [2, 6].

Stage 1. Contact area between particles increases,

Stage 2. Porosity changes from open to closed porosity,

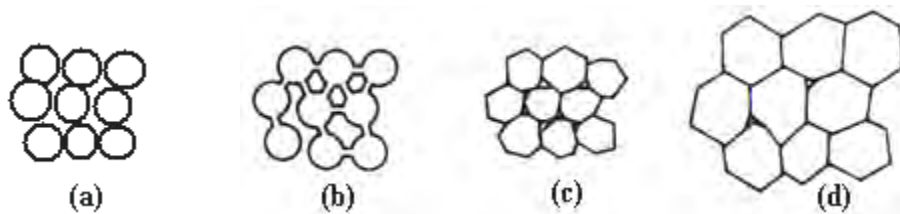Stage 3. Pore volume decreases; grains grow.

Figure 3.1: Schematic representation of sintering stages: (a) green body, (b) initial stage, (c) intermediate stage, and (d) final stage.

In the initial stage, neighboring particles form a neck by surface diffusion and presumably also at high temperatures by an evaporation-condensation mechanism. Grain growth begins during the intermediate stage of sintering. Since grain boundaries are the sinks for vacancies, grain growth tends to decrease the pore elimination rate due to the increase in distance between pores and grain boundaries, and by decreasing the total grain boundary surface area. In the final stage, the grain growth is considerably enhanced and the remaining pores may become isolated.

3.1.2 Preparation of $Gd_{0.7}Sr_{0.3}MnO_3$ bulk materials

Polycrystalline sample of $Gd_{0.7}Sr_{0.3}MnO_3$ were synthesized by standard solid state reaction technique. The high purity oxides of Gd_2O_3, $SrCO_3$ and $MnCO_3$ powders were mixed and ground in an agate mortar till a homogeneous mixture is formed. This mixture was calcined at around 1100 °C for 12 hours in a programmable furnace. The calcined powders were ground again for 6 hours to get more homogeneous mixture. This mixture was calcined again at around 1100 °C for 12 hours in a programmable furnace. The calcined powder was ground again for 30 minutes to get more homogeneous mixture. The powder were pressed into pellets of thickness 1 mm and diameter 10 mm by using a uni-axial hand presser and were sintered at around 1300 °C for 6 hours [7]. The ceramic pellets were ground again into powder by manual grinding to obtain powder materials. The sintered pellets and powders were used to measure the required structural, morphological and magnetic properties.

3.2   Synthesis of nanoparticles

3.2.1 Ultrasonication method

Ultrasonication refers to the application of sound energy at frequencies largely inaudible to the human ear (higher than » 20 kHz), in order to facilitate the disruption of particle agglomerates through a process known as cavitation. Ultrasound disruption is more energy efficient and can achieve a higher degree of powder fragmentation, at constant specific energy, than other conventional dispersion techniques. Sonication is a convenient, relatively inexpensive tool that is simple to operate and maintain. Ultrasonic waves can be generated in a liquid by introducing the sample container into a liquid that is propagating ultrasonic waves. In a sonication bath, the sound waves must travel through both the bath or cup liquid (typically water) and the wall of the sample container before reaching the suspension. The total amount of energy (E) delivered to a suspension not only depends on the applied power (P) but also on the total amount of time (t) that the suspension is subject to the ultrasonic treatment:

$$E = P \times t \tag{3.2}$$

Consequently, two suspensions treated at the same power for different times can show significantly different dispersion states.

3.2.2 Preparation of $Gd_{0.7}Sr_{0.3}MnO_3$ nanoparticles

A pellet of mutiferroics with the nominal compositions of $Gd_{0.7}Sr_{0.3}MnO_3$ was prepared by a conventional solid state reaction technique. Details of the preparation process were described in section 3.1.1. The pellets were then ground into powder by performing manual grinding for approximately 15 minutes. The obtained powders were subsequently mixed with isopropanol with a ratio of 50 mg powder and 10 ml isopropanol with a mass percentage of ~0.5%. Then, the mixtures of isopropanol and powder were put into an ultrasonic bath and sonicated for 60 minutes. After 6 hours, ~70% of the mass had precipitated and the ~30% supernatant was collected from the solution to obtain nanoparticles [8]. The supernatant was dried naturally and the collected nanoparticles was used to measure the required properties.

3.2.3 Ball Milling

The weighted powders are mixed mechanically by either ball milling or attrition milling. Milling is carried out to reduce the particle size of the powders to the nano range for the ease of solid phase reactions to occur by atomic diffusion.
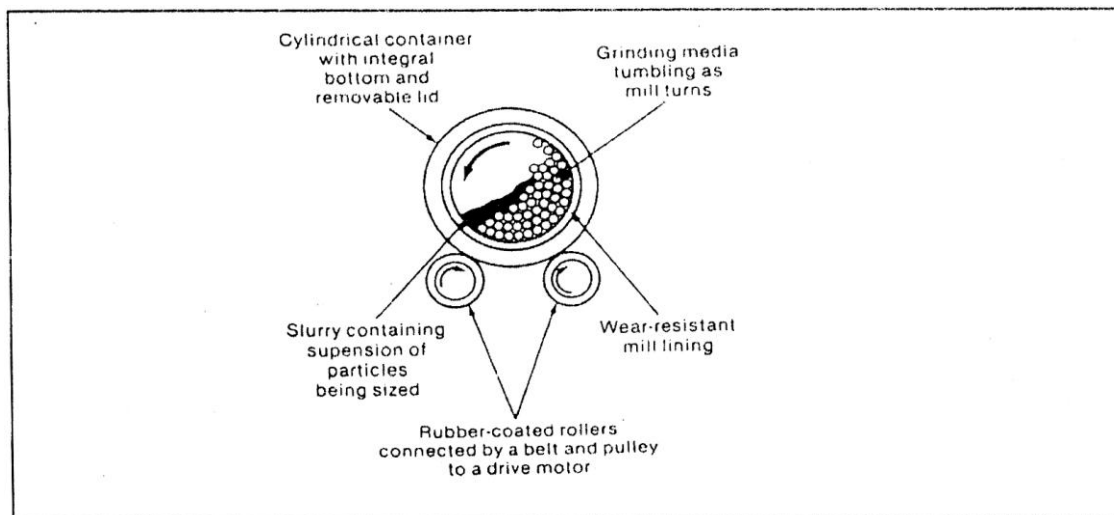
Figure 3.2: Schematic of a Ball Mill

The schematic of a ball mill is illustrated in Fig 3.2. Size and distribution of the ball is an important factor determining the product quality. Particle size is reduced by the action of impact and friction of balls with the powder. Thumb rule is, smaller the size of ball finer the particle but it takes longer time to break down big particles, hence use mix of different size balls. Motion of ball is controlled by the rotation speed of the mill. At higher speed balls cling at the inner side of the mill due to centrifugal force, too low speed would set the balls almost stationary at the bottom. In both case insufficient friction between balls and particle would not break down the particle. Optimum speed is achieved when balls are in circular monition and roll back to bottom from about three quarter way to the top as shown in Fig 3.2.

The bulk polycrystalline $Gd_{0.7}Sr_{0.3}MnO_3$ powder was ball milled for 12 hours by conventional planetary ball mill (MTI corporation, Model: QM-3SP2) with stainless steel vials and zirconia balls. The ratio of the ball and powder weight was 10:1 and the rotating speed was set to 300 rpm.

3.3 Structural Characterization techniques

3.3.1 Crystal structure

The particle size is one of the most important parameter that give the characterization properties of the materials. Investigations of materials with nanosized grains show that there is a critical crystallite size below which a dramatic change of magnetic properties occurs. Physical parameters such as the size of magnetic domains, the mean-free-path of the electron, the de-Broglie wavelength, the coherence length in superconductors, the wavelength of elastic oscillations, and the size of the excitons in semiconductors have all been to evaluate the threshold transition to the nanocrystalline state [3].

The most widely used and direct method to determine sub-micrometer sized particles is the electron microscopy, structural characteristics of specimens under investigation may be examined down to the atomic scale in resolution

3.3.1.1 X-ray Diffraction

The texture can strongly affect the properties and behavior of materials. Tensor properties of the material such as magnetic susceptibility, magneto-anisotropy, elastic coefficients and electro-optic coefficient are especially dependent on texture. Indeed, bulk materials, thin film and even the powder used in electronic applications have been fabricated to carry preferred crystallographic orientation or texture. Various analytical methods have been used to fulfill the requirement for the accurate crystallographic characterization. Among them, X-ray diffraction (XRD) is a well-developed and widely used technique [9].

X-ray diffraction (XRD) is a standard structural characterization technique for bulk materials. A straight forward application of XRD technique is the determination of the crystalline phase of a material. This is done by comparing the diffraction spectrum peak positions and intensities with those in database. This is especially informative for nanocrystalline materials that may contain several crystallographic phases, including highly disordered or amorphous phases, and for nanocrystals whose crystal structural may be different from that of the corresponding bulk due to surface effects.

Conventional XRD methods (Bragg Brentano, grazing incidence) can provide information regarding crystallinity, phase identification and qualitative assessment of planar orientation. We have Philips X"pert system which uses K_α radiation of Cu at wavelength of 0.154 nm. The K_β emission was filtered out by Ni filter. The crystalline structures of our sample were characterized by XRD operating in four circle mode.

3.3.1.2 General mechanism of X-ray diffraction

Now considering an X-ray beam incident on a single crystal, a small fraction of the incident beam will be scattered by the regular arrangement of atoms. To simplify the case, the crystal as treated as a pair of parallel planes, P_1 and P_2, separated by an interplanar spacing d.
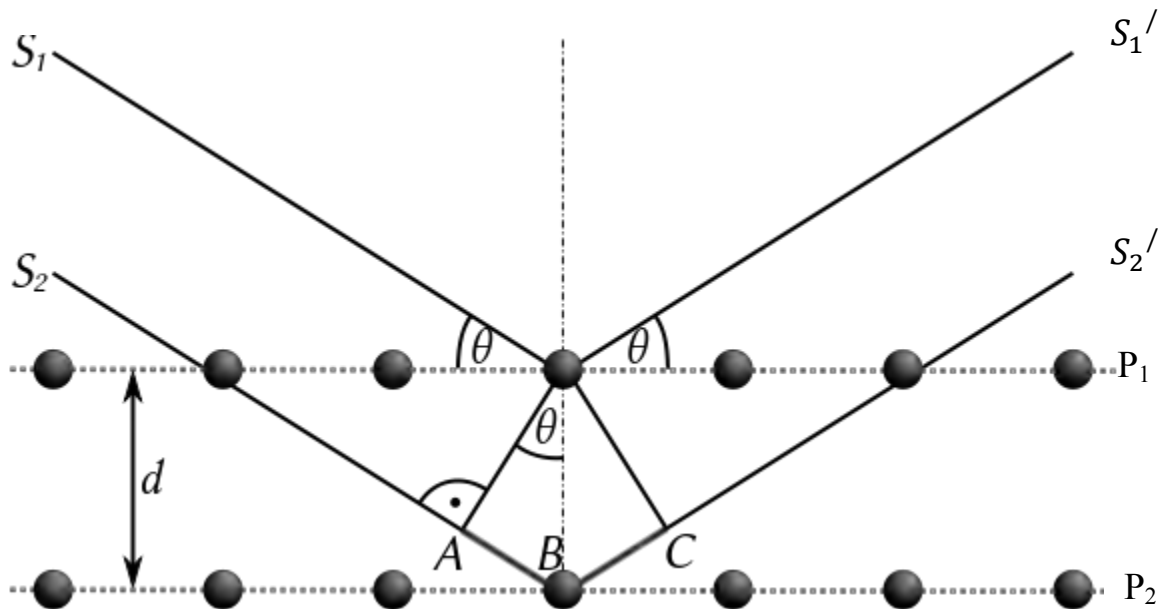
Figure 3.3: Bragg diffraction of X-rays from successive planes of atoms. Constructive interference occurs for ABC equal to an integral number of wavelengths.

In figure 3.3, the two parallel incident rays S_1 and S_2 make an angle θ with these planes. A reflected beam of maximum intensity will result if the waves represented by $S_1{}'$ and $S_2{}'$ are in phase. The path difference between S_1 to $S_1{}'$ and S_2 to $S_2{}'$ (AB+BC) must be an integral number of wavelength λ to satisfy the constructive interference. Then we can express this relationship mathematically in Bragg"s law:

$$AB + BC = 2\ d\ \sin\theta = n\ \lambda, \qquad \text{where } n=1,2,3\ldots \qquad (3.3)$$

The interplanar spacing *d,* the distance between adjacent planes in the set (*h k l*) of a material with a cubic structure and lattice parameter a, can be obtained from the equation:

$$\frac{1}{d^2} = \frac{h^2+k^2+l^2}{a^2} \tag{3.4}$$

Combined these two equations, we can obtain:

$$\frac{1}{d^2} = \frac{h^2+k^2+l^2}{a^2} = \frac{4sin^2\theta}{n^2\lambda^2} \tag{3.5}$$

Hence, it can yield:

$$2d\ sin\theta = \lambda \tag{3.6}$$

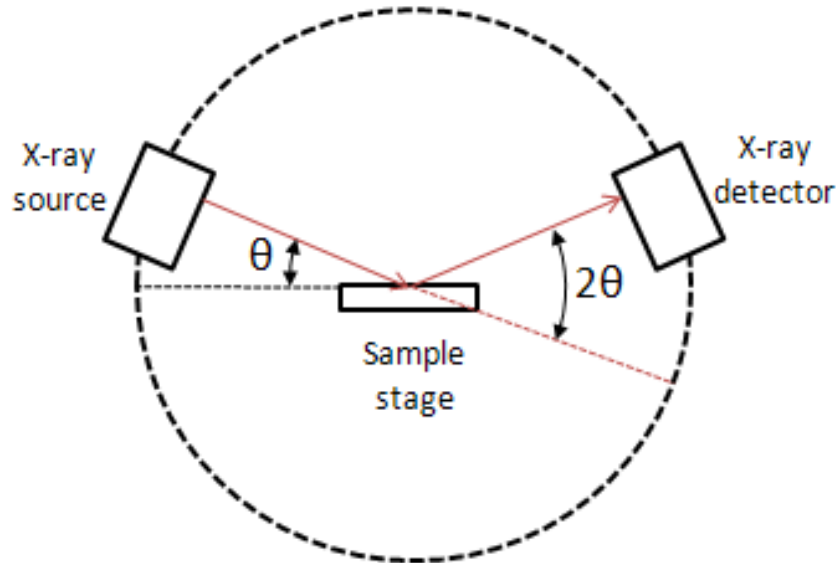**Figure 3.4:** The schematic diagram shows the operation of XRD .

Each crystalline material has a unique x-ray diffraction pattern. The number of observed peaks is related to the symmetry of the unit cell (higher symmetry generally means fewer peaks). The locations of observed peaks are related to the repeating distances between planes of atoms in the structure. And finally, the intensities of the

peaks are related to what kinds of atoms are in repeating planes. The scattering intensities for X-rays are directly related to the number of electrons in the atom. Hence, light atoms scatter X-rays are directly related to the number of electrons in the atom. Hence, light atoms scatter X-rays weakly, while heavy atoms scatter X-rays more effectively. These three features of a diffraction pattern: the number of peaks, the positions of the peaks, and the intensities of the peaks, define a unique, fingerprint X-ray powder pattern for every crystalline material.

X-ray powder diffraction is a powerful tool for characterizing the products of a solid state synthesis reaction. At the simple level, diffraction patterns can be analyzed for phase identification, it can determine what crystalline substances present in a given sample. More quantitatively, the peak positions can be used to refine the lattice parameters for a given unit cell. Unit cells in three-dimensional repeating structures have different shapes based upon the symmetry of the structure. In all cases, the unit cells are parallelepipeds, but the different shapes arise depending on restrictions placed on the lengths of the three edges (*a, b*, and *c*) and the values of the three angles (α, β, and γ) as showed in fig.
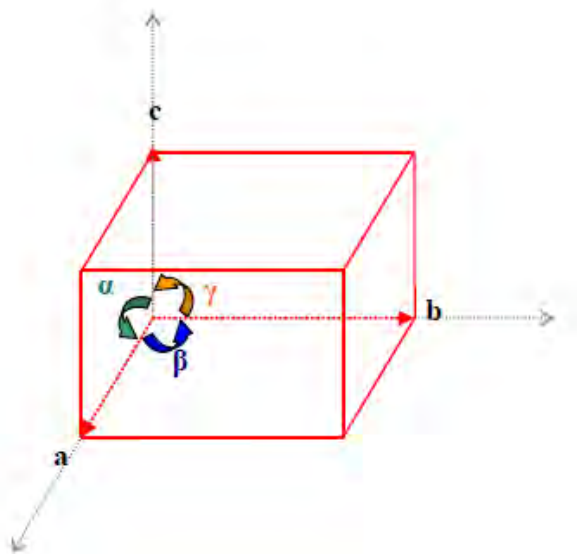

Figure 3.5: Sub unit of crystal lattice.

3.4   Morphological Studies

3.4.1 Scanning Electron Microscope (SEM)

SEM is a type of electron microscope that creates various images (surface morphology) by focusing a high energy beam of electrons onto the surface of a sample and detecting signals from the interaction of the incident electron with the sample's surface. The type of signals gathered in a SEM varies and can include secondary electrons, characteristic x-rays, and back scattered electrons. In a SEM, these signals come not only from the primary beam impinging upon the sample, but from other interactions within the sample near the surface. The SEM is capable of producing

Figure 3.6: Photograph of Scanning Electron Microscope (SEM).

high resolution images of a sample surface in its primary use mode, secondary electron imaging. Due to the manner in which this image is created, SEM images have great depth of field yielding a characteristic three-dimensional appearance useful for understanding the surface structure of a sample. This great depth of field and the wide range of

magnifications are the most familiar imaging mode for specimens in the SEM. Characteristic x-rays are emitted when the primary beam causes the ejection of inner shell electrons from the sample and are used to tell the elemental composition of the sample. The back-scattered electrons emitted from the sample may be used alone to form an image or in conjunction with the characteristic x-rays as atomic number contrast clues to the elemental composition of the sample.

The microstructure of the surface of the sintered pellets was observed using a field emission scanning electron microscope (FESEM, JEOL, JSM 5800).

3.4.1.1 Scanning process and image formation

In a typical SEM, an electron beam is thermionically emitted from an electron gun fitted with a tungsten filament cathode. Tungsten is normally used in thermo ionic electron guns because it has the highest melting point and lowest vapor pressure of all metals, thereby allowing it to be heated for electron emission, and because of its low cost. The electron beam, which typically has an energy ranging from a few 100 eV to 40 keV, is focused by one or two condenser lenses to a spot about 0.4 nm to 5 nm in diameter. The beam passes through pairs of scanning coils or pairs of deflector plates in the electron column, typically in the final lens, which deflect the beam in the x and y axes so that it scans in a raster fashion over a rectangular area of the sample surface.

When the primary electron beam interacts with the sample, the electrons lose energy by repeated random scattering and absorption within a teardrop-shaped volume of the specimen known as the interaction volume, which extends from less than 100 nm to around 5 μm into the surface. The size of the interaction volume depends on the electron's landing energy, the atomic number of the specimen and the specimen's density. The energy exchange between the electron beam and the sample results in the reflection of high-energy electrons by elastic scattering, emission of secondary electrons by inelastic scattering and the emission of electromagnetic radiation, each of which can be detected by specialized detectors. The beam current absorbed by the specimen can also be detected and used to create images of the distribution of specimen current. Electronic amplifiers of various types are used to amplify the signals which are displayed as

variations in brightness on a cathode ray tube. The raster scanning of the CRT display is synchronized with that of the beam on the specimen in the microscope, and the resulting image is therefore a distribution map of the intensity of the signal being emitted from the scanned area of the specimen. The image may be captured by photography from a high resolution cathode ray tube, but in modern machines is digitally captured and displayed on a computer monitor.

3.4.2 Transmission electron microscopy (TEM)

The resolution capabilities of an optical microscope are limited by the wavelength of light in the visible range. The transmission electron microscopy technique was developed based on the idea that the interaction between the sample and electrons with wavelength smaller than visible light, provides higher resolution so as to detail features even as small as a single column of atoms. This technique usually combines the high resolution imaging with elemental microanalysis and electron diffraction, so that a complete characterization of the shape, size, chemical composition and crystalline structure of a nanostructured material is achieved. In a TEM, an electron gun, located at the top of it, emits the electrons by thermionic or field emission. These electrons travel through vacuum in the column of the microscope where electromagnetic lenses focus them into a very thin beam. The electron beam then travels through the specimen under study. At the bottom of the microscope, he image is formed on the image plane of objective lens from the unscattered electrons. Then, projector lenses form the images on a screen or CCD camera. The nanostructures (nanoparticles, nanowires, core/shell, or hollow particles) were first dispersed in a solvent, and separated by ultra-sonication. This is a very important step, because the quality of image formed in a TEM is highly sensitive to sample thickness. Hence, any agglomeration of the nanostructures will appear as an opaque object to the electrons, and will result in loss of details. One drop of the ultra-sonicated nanoparticle dispersion is then allowed to dry on a copper mesh grid with carbon lining. When the grid is completely dry, it is then exposed to the electron beam inside the TEM.

In this case, the morphology and physical structure of the nanoparticles were studied using a FEI TECNAI TEM with a 200 kV accelerated voltage

Figure 3.7: Photograph of Transmission Electron Microscope (TEM).

3.5 X-Ray Photoelectron Spectroscopy (XPS)

XPS works on the principle of photoelectric effect discovered by Heinrich Hertz in 887. Upon radiation of appropriate energy incident, electrons are emitted from the surface of metal. The relation between the energy of the excitation radiation, work function of the metal and the maximum kinetic energy of the emitted electron as proposed by Einstein in 1905 is:

$$h\nu = \phi + KE_{max} \tag{3.8}$$

„Φ" is the work function of the metal, „hυ" is the energy of the radiation, „KE_{max}" is the maximum kinetic energy of the emitted electron. For analysing the core electronic structure (0 – 1300 eV) of elements, radiation of high energy were used like X-rays, hence the corresponding spectroscopy is termed X-ray Photoelectron Spectroscopy (XPS) (Figure 3.8). Surface analysis by XPS is accomplished by irradiating a sample with monoenergetic soft X-rays and analysing the energy of the detected electrons. Mg Kα (1253.6 eV), Al Kα (1486.6 eV), or monochromatic Al Kα (1486.7 eV) X-rays are usually used. These photons have limited penetrating power in a solid of the order of 1 – 10 μm. They interact with atoms in the surface region, causing electrons to be emitted by the photoelectric effect.
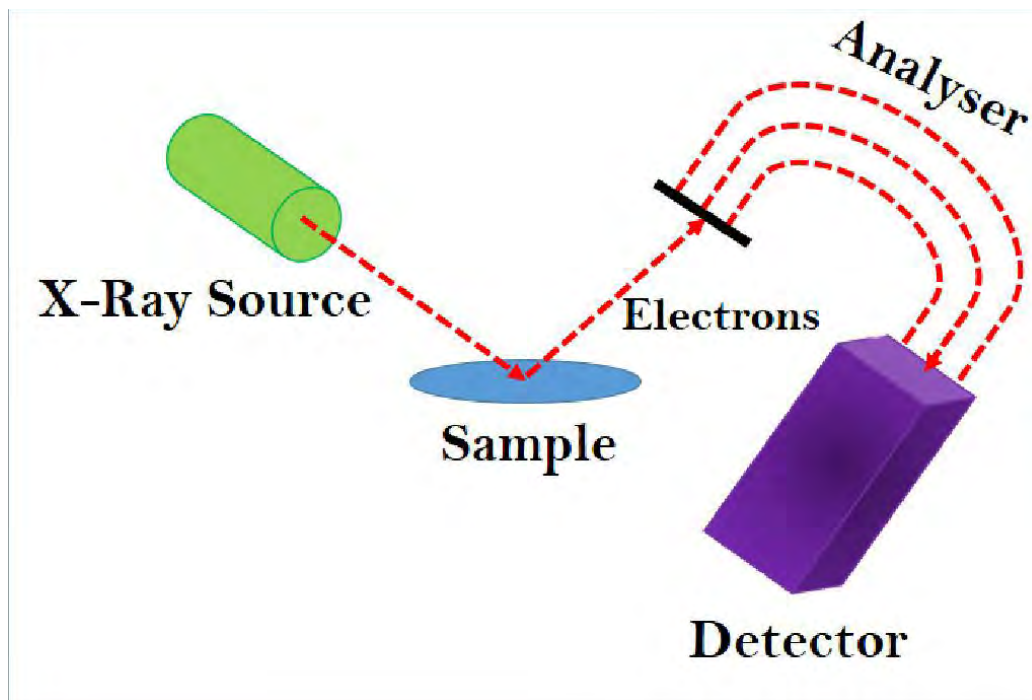
Figure 3.8: Schematic diagram of a typical X-ray photoelectron spectroscopy (XPS).

The emitted electrons have measured kinetic energies given by:

$$KE = h\nu - BE - \phi_s \tag{3.9}$$

where „hυ" is the energy of the photon, „BE" is the binding energy of the atomic orbital from which electron originates, „Φ_S" is the work function of the spectrometer. The inding energy may be regarded as the energy difference between the initial and final states after the photoelectron has left the atom. Because there are a variety of possible final states of the ions from each type of atom, there is a corresponding variety of kinetic energies of the 50 emitted electrons. Moreover there is a different probability or cross section for each final state.

Because each element has unique set of binding energies, XPS can be used to identify and determine the concentration of the elements in the surface. Variation in the elemental binding energies (the chemical shifts) arise from differences in the chemical potential and polarizability of compounds. These chemical shifts can be used to identify the chemical state of the material being analysed. In our studies, X-ray photoelectron spectroscopy (XPS, ULVAC-PHI Inc., Model 1600) analysis was carried out with a Mg-K_α radiation source.

3.6   Magnetization measurement

3.6.1   Superconducting Quantum Interference Device (SQUID)

Superconducting Quantum Interference Device (SQUID) magnetometer is one of the most effective and sensitive ways of measuring magnetic properties. In particular, it is the only method which allows to directly determine the overall magnetic moment of a sample in absolute units. The equations established by Brian David Josephson in 1962, the electrical current density through a weak electric contact between two superconductors depends on the phase difference $\Delta\varphi$ of the two superconducting wave functions [10]. Moreover, the time derivative of $\Delta\varphi$ is correlated with the voltage across this weak contact. In a superconducting ring with two (Figure 3.9a, blue) weak contacts, $\Delta\varphi$ is additionally influenced by the magnetic flux Φ through this ring. Therefore, such a structure can be used to convert magnetic flux into an electrical voltage. This is the basic working principle of a SQUID magnetometer.
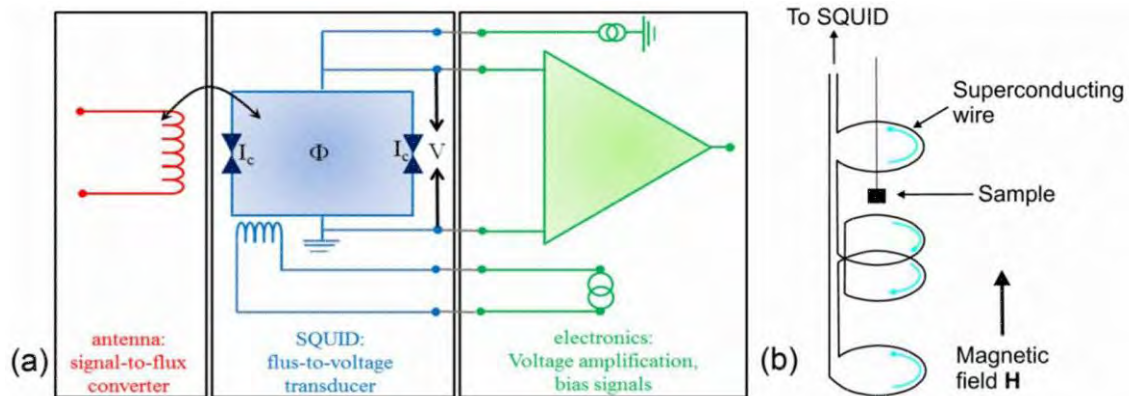

Figure 3.9: (a) Schematic diagram of the working principle of SQUID (flux to voltage converter). (b) The detection coils of the SQUID.

To measure the magnetization of a sample, a field must be applied to the sample to induce a net moment in the sample. The net moment induced in the sample induces a current in the detector coils which are made from superconducting wire, the detector coils are connected to the SQUID and the output voltage of the SQUID is directly proportional to the current induced by the magnetization of the sample. Hence the SQUID acts as flux-

to-voltage convertor and magnetization is measured from the induced voltage. In Figure 3.9b the setup of the detection coils is shown. There are coils at the top and bottom that are wound anti-clockwise and two central coils wound clockwise. This arrangement of detection coils means that variations of the magnetic field induce opposing current in the clockwise and anti-clockwise coils which cancel each other, thus minimizing noise in the detection circuit. The magnetization produced by the sample would not be uniform across the sample space, with the detection coils measuring the local changes in the magnetic flux density, in this way a current is induced in the detection coils by the sample"s net magnetization. A cutaway view of the Quantum Design MPMS XL7 SQUID 45 magnetometer used for the measurement of magnetization of materials is shown in figure 3.10
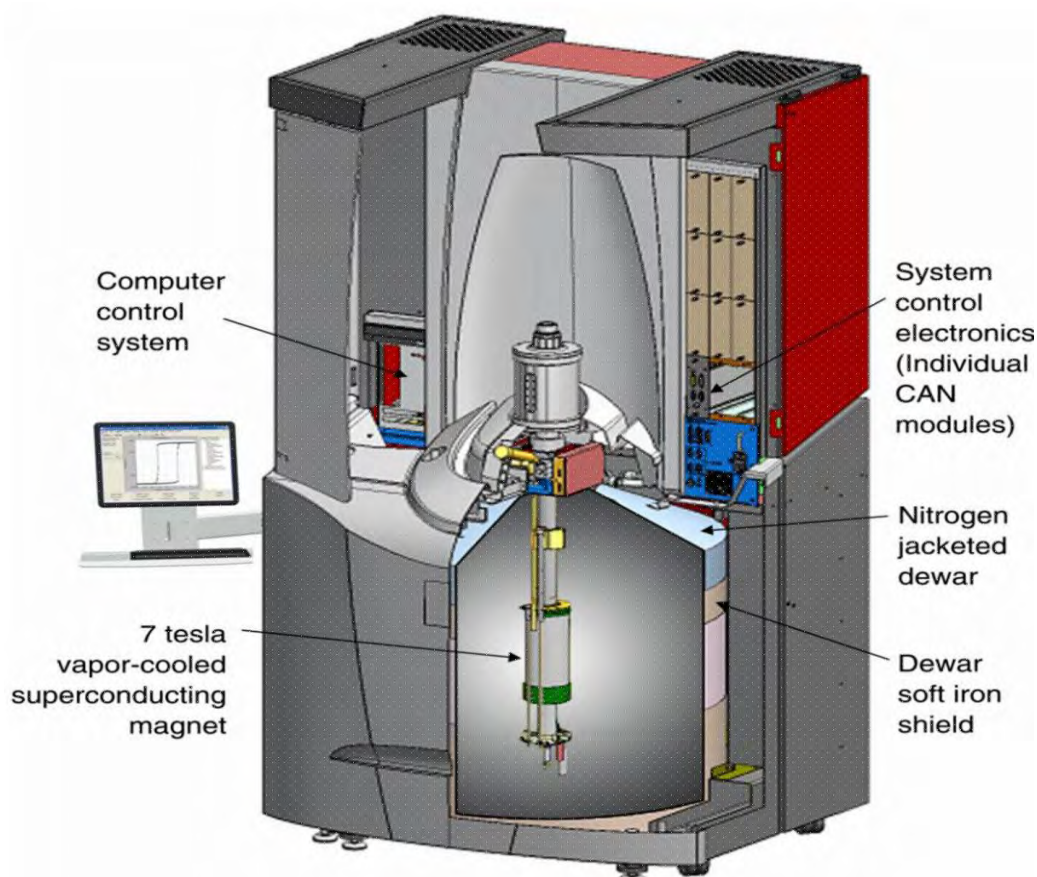

Figure 3.10: Cutaway view of the MPMS SQUID VSM.

3.6.2 Magnetic hysteresis loop

In the case of a typical ferromagnetic material the hysteresis loop as shown in Fig. 3.11, it gives the relation between the magnetization (M) and the applied field (H).

The parameters extracted from the hysteresis loop that are most often used to characterize the magnetic properties of magnetic media include: saturation magnetization (M_s), remanence (M_r), coercive field (H_c), susceptibility (χ) and Curie temperature (T_c). The formal definition of the coercive field (H_c) in the field required to reduce the
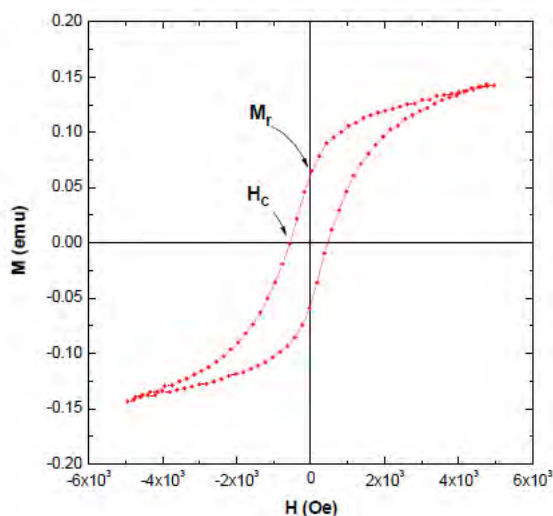

Figure 3.11: Typical hysteresis loop ferromagnetic materials.

magnetization process. It is a complicated parameter for magnetic films and is related to reversal mechanisms, microstruclture, sample shape, dimensions of the crystallites, nature of the boundaries, and also the surface and interfacial properties.

3.6.3   Technique of magnetization measurement

In this section we focus on the discussion of experimental technique used for characterizing the magnetic nanoparticles and nanocomposites.

3.6.3.1 Zero-field cooled (ZFC) / Field-cooled (FC) curve

Zero field cooled (ZFC) experiments provide a means of investigating the effects of the various magnetic interaction [11]. For small magnetic particles, the curve of

temperature dependence of magnetization has a typical shape as shown in Fig. 3.12. As the particles cool in zero applied magnetic fields, they tend to be magnetized along preferred crystal directions in the lattice, thus minimizing the magneto-crystalline energy. Since the orientation of each crystallite varies, the net moment of the system will be zero. Even when a small external field is applied, the moments will remain locked into the preferred crystal directions in the low temperature portion of the ZFC curve. As the temperature increases, more thermal energy is available to disturb the system.
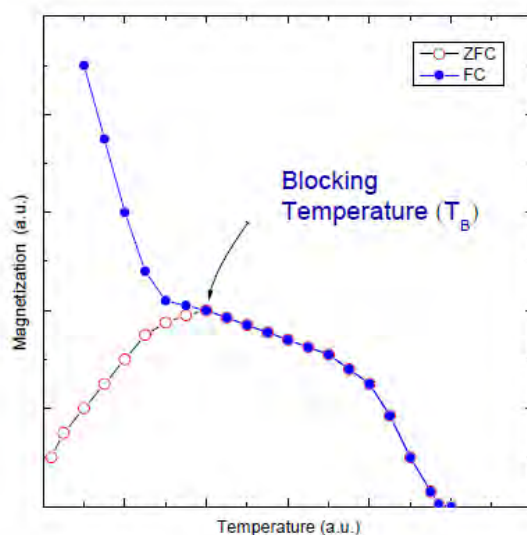

Figure 3.12: Typical ZFC and FC curves for magnetic nanoparticles with blocking temperature (T_B).

Therefore, more moments will align with the external field direction in order to minimize the Zeeman energy term. In other words, thermal vibration is providing the activation energy required for the Zeeman interaction. Eventually, the net moment of the system reaches a maximum where the greatest population of moments has aligned with the external field. The peak temperature is called the blocking temperature (T_B), which is dependent on the particle size. As temperature rise above T_B, thermal energy become strong enough to overcome the Zeeman interaction and then results of randomize the moments.

A field cooled (FC) measurement is proceed in a similar manner to zero-field cooled (ZFC) except that the constant applied field in both cooling and heating process. The net moment is usually measured while heating. However, the FC curve will diverge from the ZFC curve at appoint near the blocking temperature as shown in Fig. 3.12. This

divergence occurs because the spins from each particle will tend to align with the easy axis that is closest to the applied field direction, and remain frozen in that direction at low temperature.

The divergence of magnetization below T_B in the ZFC-FC curve is attributed to the existence of magnetic anisotropy barriers [12]. The derivation of the magnetization decay plot, *f(T)* represents the distribution of anisotropy energy barriers:

$$f(T) = \frac{d}{dT}\left(\frac{M_{ZFC}}{M_{FC}}\right)$$

where M_{ZFC} denotes only the contribution of nanoparticle, the energy barriers of which are overcame by the thermal energy at the measurement, while M_{FC} represents the contributions from all nanoparticles.

References:

[1]   Goldman A., Handbook of Modern Ferromagnetic Materials, Kulwer Acad. Pub, Boston, U.S.A , 1999.

[2]   Valenzuela R., Magnetic Ceramics, Cambridge University Press, Cambridge, 1994.

[3]   West, A. R., "Solid state chemistry and its applications", John willey sons, 1887.

[4]   Kingery W. D., Bowen H. K. and Uhlman D. R., Introduction to Ceramics, 2nd edition, Wiley Interscience, Newyork, 476 , 1976.

[5]   Coble R. L. and Burke J. E., 4th Int. Symp. On the Reactivity of Solids, Amsterdam, 38-51, 1960.

[6]   McColm I. J. and Clark N. J., Forming, Shaping and Working of high Performance Ceramics, Blackie, Glasgow, 1-338, 1988.

[7]   Basith, M. A., Kurni, O., Alam, M. S., Sinha, B. L. and Bashir Ahammad, "Room temperature dielectric and magnetic properties of Gd and Ti co-doped $BiFeO_3$ ceramics", J. Appl. Phys., 115, 024102–024107, 2014.

[8]   Basith, M. A., Ngo, D. –T., Quader, A., Rahman, M. A., Sinha, B. L., Bashir Ahmmad, Fumihiko Hirose and Molhave, K., "Simple top-down preparation of magnetic $Bi_{0.9}Gd_{0.1}Fe_{1-x}TixO_3$ nanoparticles by ultrasonication of multiferroic bulk material", Nanoscale, 6, 14336, 2014.

[9]   Kelsall, R. W., Hamley, I. W., Geoghegan, M., Nanoscale Science and Technology, 2005.

[10]   B.D. Josephson, The discovery of tunnelling supercurrents, Rev. Mod. Phys. 46, 251, 1974.

[11]   Dormann J. L., Fiorani D., and Tronc E., "Magnetic relaxation in fine-particle systems", Adv. Chem. Phys., 98, 283–494, 1997.

[12]   Hou, Y. L., Yu, J. F., Gao, S., "Solvothermal reduction synthesis and characterization of superparamagnetic magnetite nanoparticles", J. Mater. Chem., 13, 8, 1983-1987, 2003.

CHAPTER 4

RESULTS AND DISCUSSION

4.1 XRD analysis of $Gd_{0.7}Sr_{0.3}MnO_3$ materials

First of all, to determine the structural properties of the manganites system the powder X-ray diffraction experiments were carried out. The XRD patterns of $Gd_{0.7}Sr_{0.3}MnO_3$ bulk materials sintered at 1300 ^0C, nanoparticles prepared by ultrasonication and ball milling techniques are shown in figure 4.1 [(a), (b) and (c)]. The
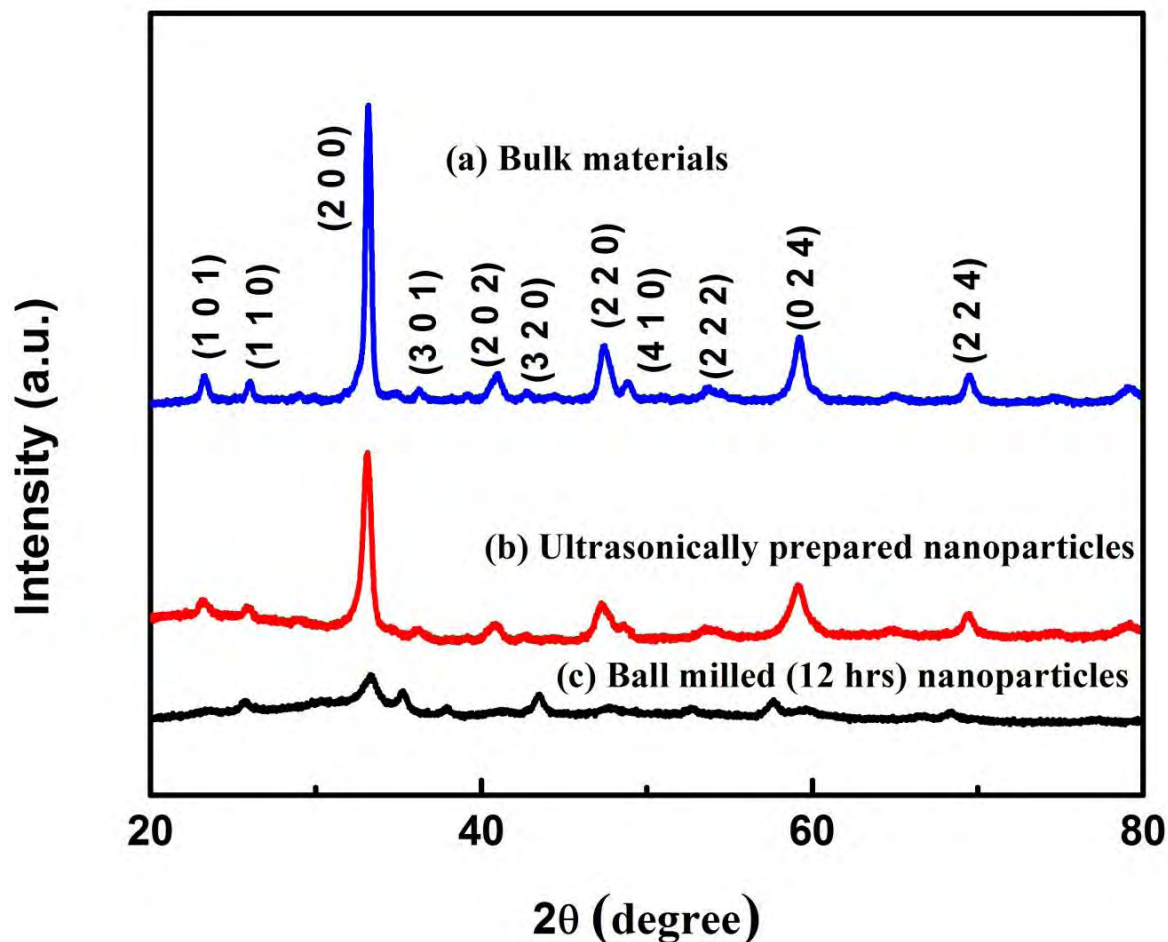

Figure 4.1: Powder X-ray diffraction patterns of $Gd_{0.7}Sr_{0.3}MnO_3$ (a) bulk materials sintered at 1300 ^0C, (b) nanoparticles prepared by ultrasonication of their bulk powder materials for 60 minutes and (c) nanoparticles prepared by ball milling of bulk powder materials for 12 hrs. The observed reflections were indexed on the basis of an orthorhombic crystal system.

reflections of bulk powder materials and nanoparticles prepared by ultrasonication were indexed on the basis of an orthorhombically distorted perovskite structure [1,2]. The lattice parameters for the bulk polycrystalline sample are: a = 5.4291 Å, b =5.4415 Å and c = 7.6269 Å. The lattice parameters are: a = 5.4291 Å, b = 5.4653 Å and c = 7.6022 Å for the corresponding nanoparticles prepared by ultrasonication.

The lattice parameters are in good agreement with the reported parameters of orthorhombic $Gd_{0.7}Sr_{0.3}MnO_3$ [1] manganites. The XRD patterns (figures 4.1 (a) and (b)) demonstrate the crystallinity of bulk materials as well as nanoparticles prepared by ultrasonic energy, however, a tendency of crystalline to amorphous like phase transition was observed in the nanoparticles synthesized by high energy ball milling as shown in pattern (figure 4.1 (c)).

4.2 Morphological Studies and particle size of $Gd_{0.7}Sr_{0.3}MnO_3$ materials

To investigate the microstructure of the surface of the pellets FESEM imaging was carried out. Figure 4.2(a) demonstrates the surface morphology of the pellets of $Gd_{0.7}Sr_{0.3}MnO_3$ bulk perovskite manganites. The surface of the pellets is pretty homogeneous and the average grain size is around 1 ± 0.2 μm.

The particle size of the synthesized nanoparticles was studied using TEM imaging. Figure 4.2(b) and (c), show bright field (BF) TEM image of $Gd_{0.7}Sr_{0.3}MnO_3$ particles, respectively, obtained at 60 minutes of sonication and 12 hrs of ball milling of their bulk powders. The size of the ultrasonically prepared nanoparticles estimated from this TEM image is 20-40 nm. The average size of the nanoparticle prepared by ball milling technique is ranging from 100-150 nm.
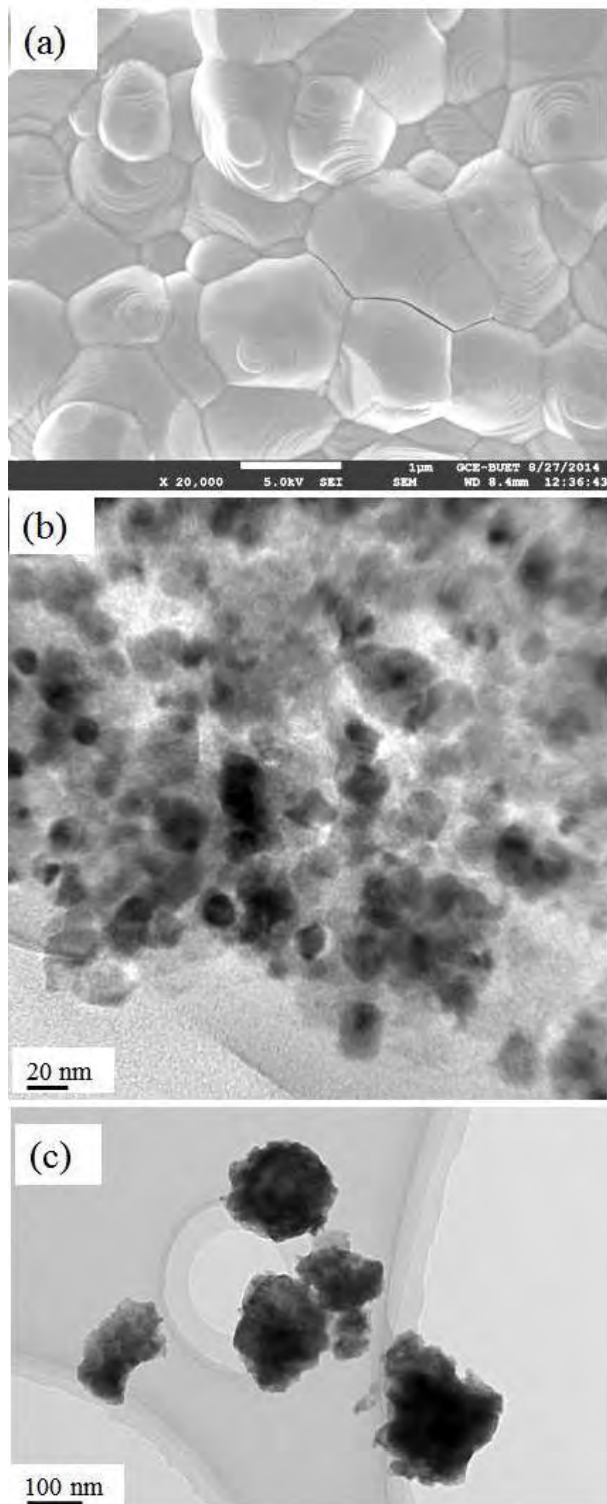
Figure 4.2: (a) FE SEM image of the surface morphology of bulk polycrystalline $Gd_{0.7}Sr_{0.3}MnO_3$ manganites sintered at 1300 ^{0}C for 6 hours. (b) Bright field TEM image of $Gd_{0.7}Sr_{0.3}MnO_3$ nanoparticles prepared by ultrasonication technique [3]. (c) TEM image of $Gd_{0.7}Sr_{0.3}MnO_3$ nanoparticles prepared by high energy ball milling.
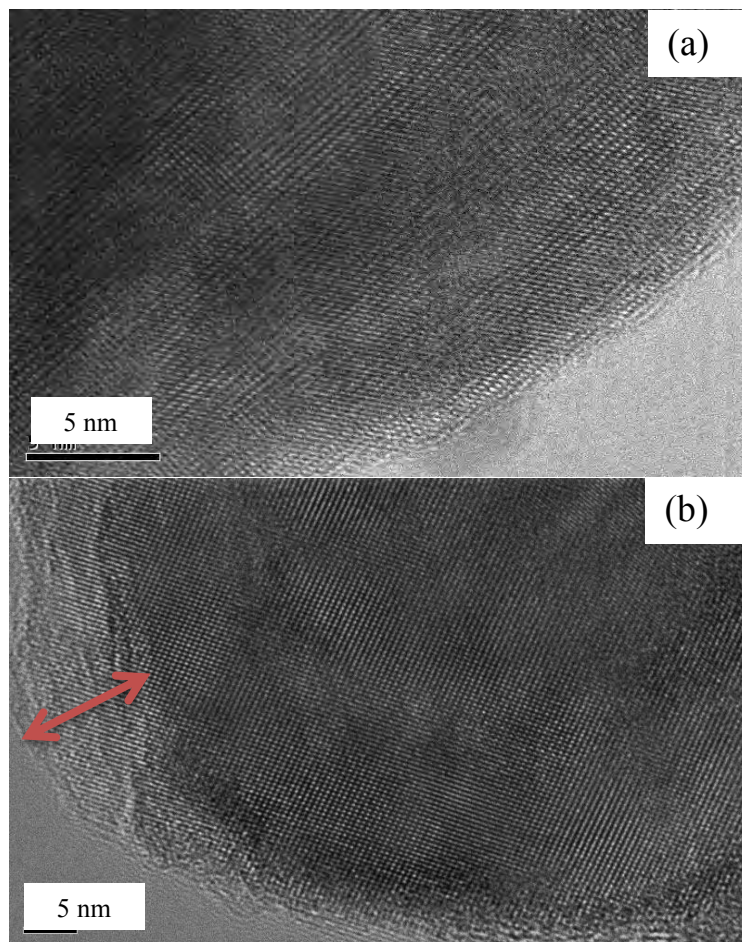
Figure 4.3: HRTEM images of the surface of $Gd_{0.7}Sr_{0.3}MnO_3$ nanoparticles prepared by (a) ultrasonication (b) by high energy milling of bulk their bulk powder materials. The surface roughness of the nanoparticles produced by 12 hrs milling is clearly visible in image (b) and marked by arrow sign.

The surface of $Gd_{0.7}Sr_{0.3}MnO_3$ nanoparticles prepared by ultrasonication and high energy milling of their bulk powder materials are shown in figures 4.3 (a) and (b), respectively. The surface roughness of the nanoparticles produced by high energy milling is clearly visible (marked by arrow sign) in HRTEM image, figure 4.3 (b) unlike the homogeneous surface of the ultrasonically prepared nanoparticles, figure 4.3 (a). This roughness in ball milled nanoparticles may behave like a nonmagnetic layer and consequentially affect the magnetic properties of the synthesized nanoparticles.

4.3 XPS Analysis of $Gd_{0.7}Sr_{0.3}MnO_3$ materials

To identify the chemical bonding in bulk materials and nanoparticles synthesized by ultrasonication technique, X-ray Photoelectron Spectroscopy (XPS) have been performed.
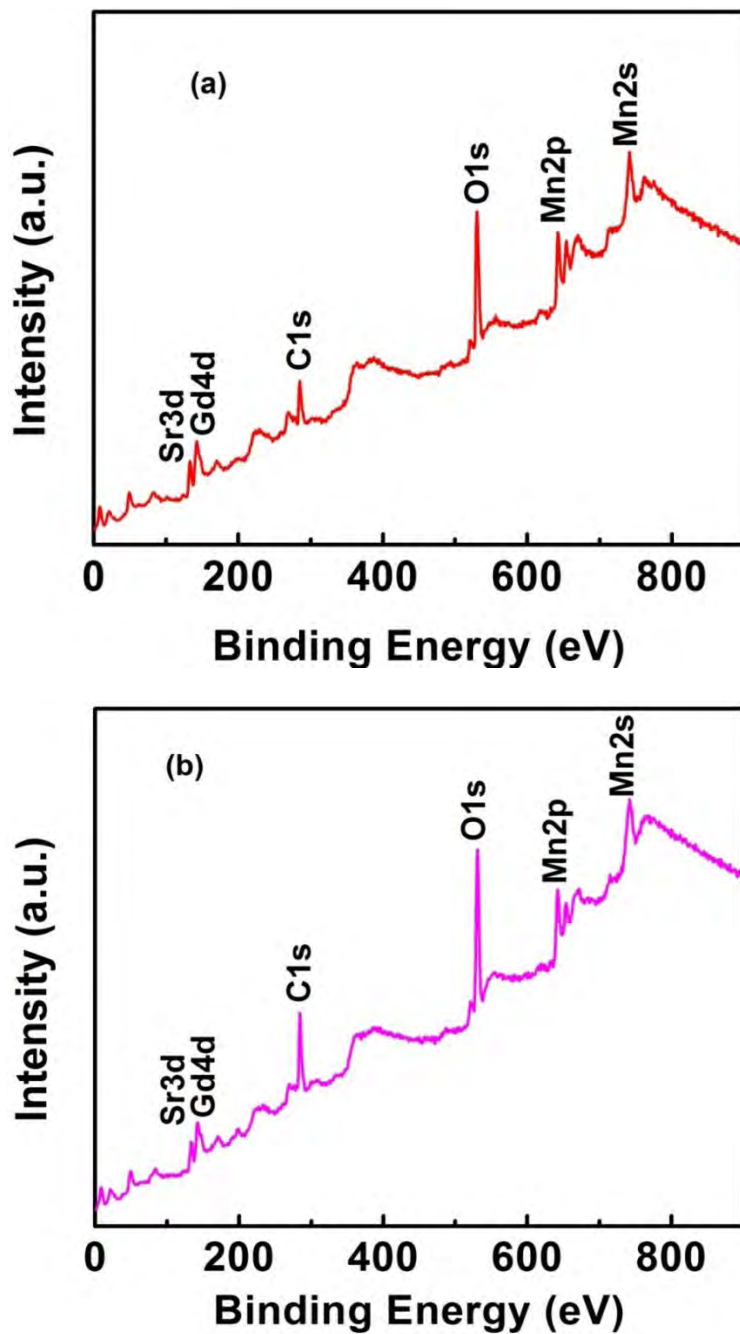

Figure 4.4: XPS spectra of all elements of (a) $Gd_{0.7}Sr_{0.3}MnO_3$ bulk materials and (b) $Gd_{0.7}Sr_{0.3}MnO_3$ nanoparticles.

Figure 4.4(a) and (b) show the XPS spectra of all elements of (a) $Gd_{0.7}Sr_{0.3}MnO_3$ bulk materials and (b) $Gd_{0.7}Sr_{0.3}MnO_3$ nanoparticles prepared by ultrasonication technique. As illustrated in the Mn2p spectra[Fig.4.4(a)] for $Gd_{0.7}Sr_{0.3}MnO_3$ bulk materials, two broad peaks at 642.30 eV and 654.08 eV are evident, corresponding to the binding energies of $Mn2p_{3/2}$ and $Mn2p_{1/2}$, respectively.

The binding energy of $Mn2p_{3/2}$ can be used to study the Mn valence state in manganese oxide [4], which are 641.5eV and 642.8 eV for Mn^{3+} and Mn^{4+} ions, respectively. The binding energies for Gd and Sr are 142.30 eV and 133.17 respectively. The measured binding energies for Gd, Sr, Mn etc. confirmed the phase purity of this compound.

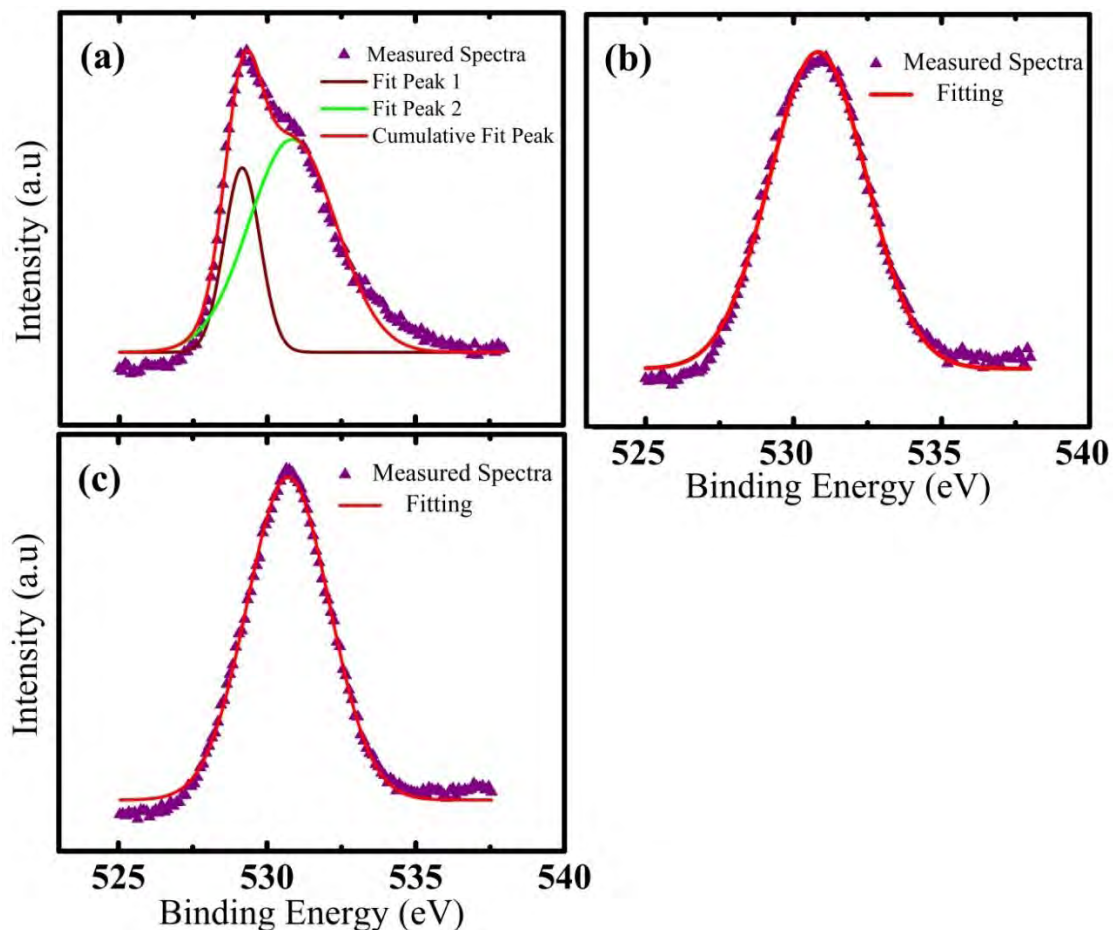
Figure 4.5: XPS spectra of the O 1s of $Gd_{0.7}Sr_{0.3}MnO_3$ (a) bulk polycrystalline powder materials sintered at 1300 ^{0}C, (b) nanoparticles prepared by ultrasonication technique and (c) nanoparticles prepared by ball milling technique.

Figures 4.5 (a), (b) and (c) demonstrate the O 1s XPS spectra of bulk polycrystalline $Gd_{0.7}Sr_{0.3}MnO_3$ manganites and their corresponding nanoparticles prepared by ultrasonication and ball milling, respectively. The O1s XPS spectra of bulk polycrystalline $Gd_{0.7}Sr_{0.3}MnO_3$ manganites show a slightly asymmetric peak very close to 529.5 eV along with an additional peak. The asymmetric curves of the bulk sample can be Gaussian fitted by two symmetrical peaks at 529.3 eV and 530.8 eV, respectively. The lower binding energy peak at 529.3 eV corresponds to O 1s core spectrum, while higher binding energy peak is attributed to the oxygen vacancies i.e. to the oxygen related defects [5-7] in the sample. Interestingly, in the case of $Gd_{0.7}Sr_{0.3}MnO_3$ nanoparticles prepared by ultrasonication have been observed a symmetrically single XPS peak (figure 4.5 (b)) of O 1S [8, 9]. This indicates the absence of oxygen vacancy in ultrasonically prepared $Gd_{0.7}Sr_{0.3}MnO_3$ nanoparticles. Similar to the ultrasonically prepared nanoparticles, the ball milled nanoparticles also did not show any peak correspond to oxygen vacancy as shown in figure 4.5 (c). It is expected that the presence and absence of oxygen vacancies [10] in $Gd_{0.7}Sr_{0.3}MnO_3$ bulk materials and their nanoparticles, respectively will affect the mixed Mn^{3+}/Mn^{4+} valence state which ultimately will influence their magnetization [11]. The absence of oxygen vacancies in the synthesized nanoparticles is a good sign to explore their multiferroic as well as transport properties in the future investigations.

4.4   Temperature dependent magnetization of $Gd_{0.7}Sr_{0.3}MnO_3$ materials using SQUID

To investigate the phase transition temperatures of bulk materials and corresponding synthesized nanoparticles, the temperature dependent magnetization measurements were carried out. Figure 4.6 (a), (b) and (c) demonstrate the temperature dependence of the magnetization (M-T) curves of $Gd_{0.7}Sr_{0.3}MnO_3$ bulk materials sintered at 1300 ^0C, nanoparticles prepared by ultrasonication of their bulk powder materials for 60 minutes and nanoparticles prepared by ball milling of bulk powder materials for 12 hrs., respectively in zero field cooled (ZFC) and field cooled (FC) processes.
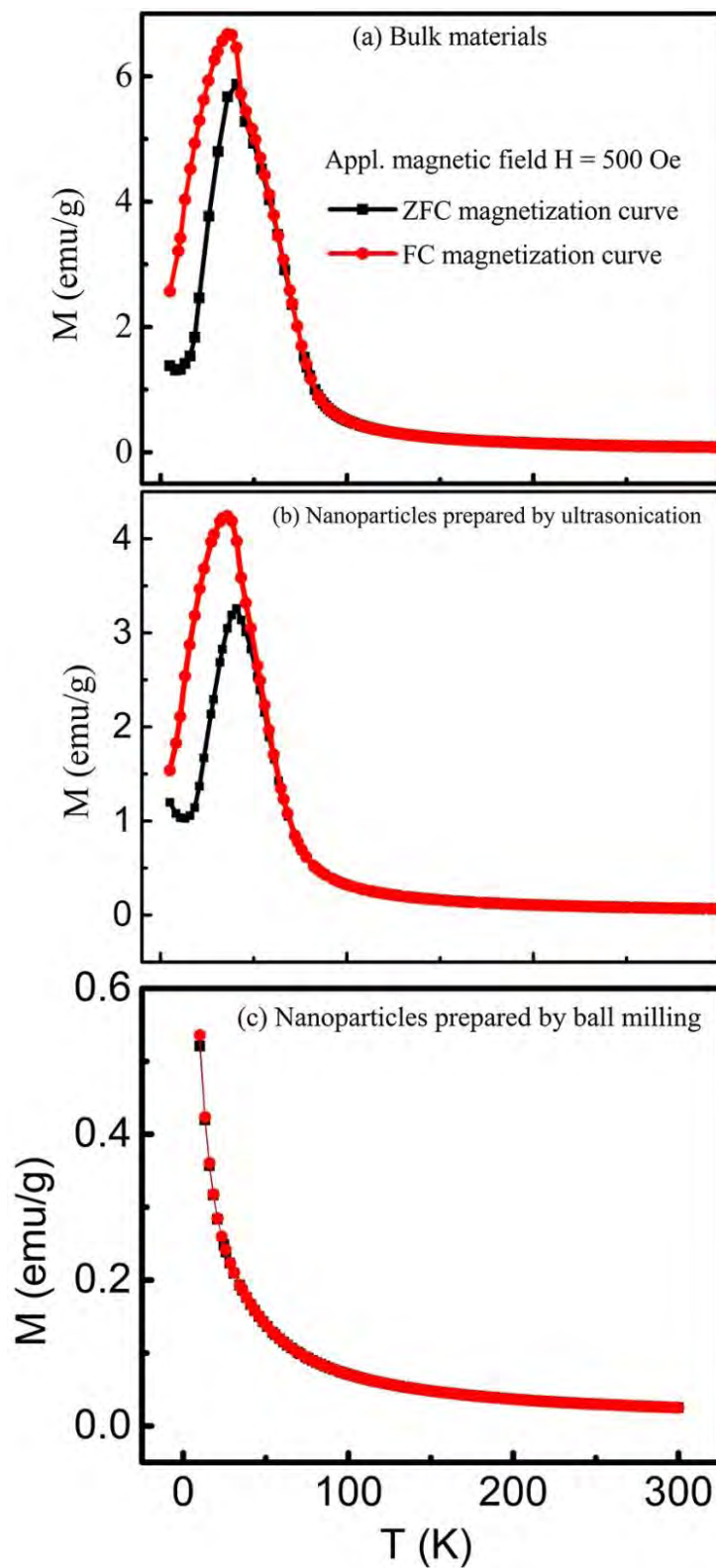
Figure 4.6: Temperature dependence of magnetization (M-T curves) of of $Gd_{0.7}Sr_{0.3}MnO_3$ (a) bulk materials sintered at 1300 ^{0}C, (b) nanoparticles prepared by ultrasonication and (c) ball milling techniques in ZFC and FC processes. In each case the applied magnetic field was 500 Oe.

To perform the experiment in the ZFC process, the sample was initially cooled from 300K to 5K and data were collected while heating in the presence of the applied field. On the other hand, in the FC mode, data were collected while cooling in the presence of 500 Oe magnetic field. In the case of bulk $Gd_{0.7}Sr_{0.3}MnO_3$ manganites (figure 4.6 (a)) as well as nanoparticles prepared by ultrasonication technique (figure 4.6 (b)), a clear splitting between ZFC and FC magnetization curves were observed below 42-47 K under the application of a magnetic field of 500 Oe.

The splitting of the ZFC and FC curves clearly suggest that $Gd_{0.7}Sr_{0.3}MnO_3$ bulk materials and their corresponding nanoparticles are in a spin-glass-like state [1, 12, 13] at temperatures below 42-47 K. Moreover, the temperature dependent magnetization curves exhibit a paramagnetic to spin-glass like transition for both bulk powder materials and ultrasonically prepared nanoparticles at temperatures T_g = 35-40 K. The value of the transition temperature is quite consistent with value reported in Ref. [13] for the same manganite system. Notably, in the case of nanoparticles prepared by ball milling technique, both ZFC and FC curves coincide with each other throughout the temperature range.

Beside this, nanoparticles prepared by ball milling did not show any phase transition, however, an upturn of magnetization was observed at low temperature which indicate their weak ferromagnetic nature. In this way, the magnetic behavior of the nanoparticles synthesized by ball milling technique is pretty different than those of bulk materials and corresponding nanoparticles prepared by ultrasonication.

To estimate whether there is any difference between the transition temperature of the nanoparticles and bulk materials, the field cooled magnetization curves for nanoparticles and bulk materials have plotted again shown in figure 4.7. There is no difference between their transition temperature i.e. the T_g value for nanoparticles as well as bulk materials was same and it is $\approx$ 37 K.
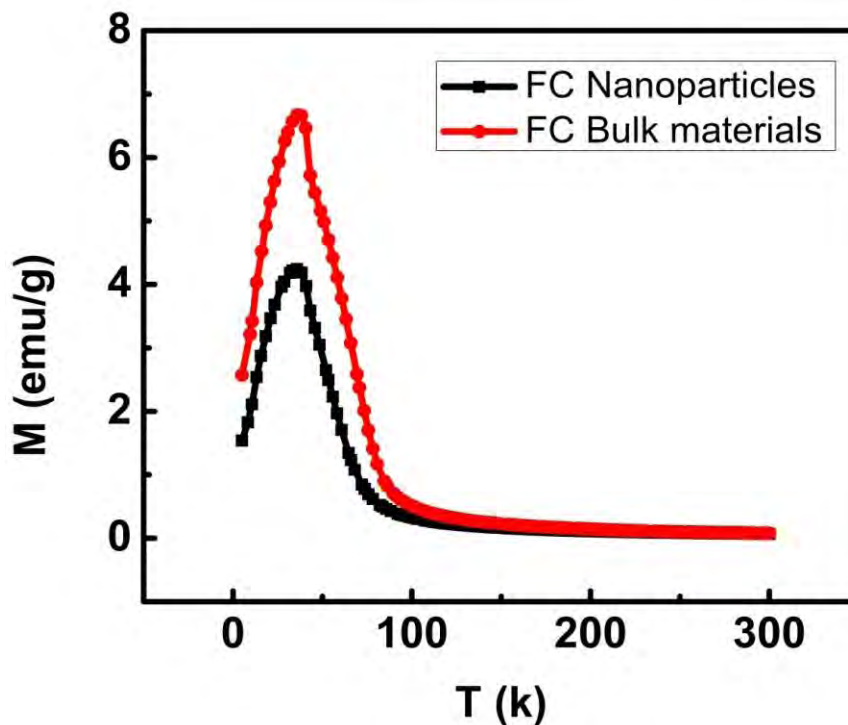
Figure 4.7: The field cooled (FC) magnetization curves exhibit the coincidence of the transition temperature of $Gd_{0.7}Sr_{0.3}MnO_3$ nanoparticles and their bulk counterparts.

4.5 Magnetic Characterization of $Gd_{0.7}Sr_{0.3}MnO_3$ using SQUID

To further clarify the difference between the magnetic properties of bulk materials and nanoparticles synthesized by two different techniques, field dependent magnetization measurements were carried out. The magnetization vs magnetic field (M-H) hysteresis loops of $Gd_{0.7}Sr_{0.3}MnO_3$ bulk materials, nanoparticles prepared by ultrasonication and ball milling techniques were carried out at 300 K and also at 20 K, figures 4.8 and 4.9, respectively.

The unsaturated linear curves without any detectable hysteresis as shown in figure 4.8 clearly indicate the paramagnetic nature of $Gd_{0.7}Sr_{0.3}MnO_3$ bulk powder materials and their corresponding nanoparticles at room temperature. However, magnetization measurement at 20 K, figure 4.9 demonstrated hysteresis with significant coercivities in bulk materials and their corresponding nanoparticles prepared by ultrasonication technique.
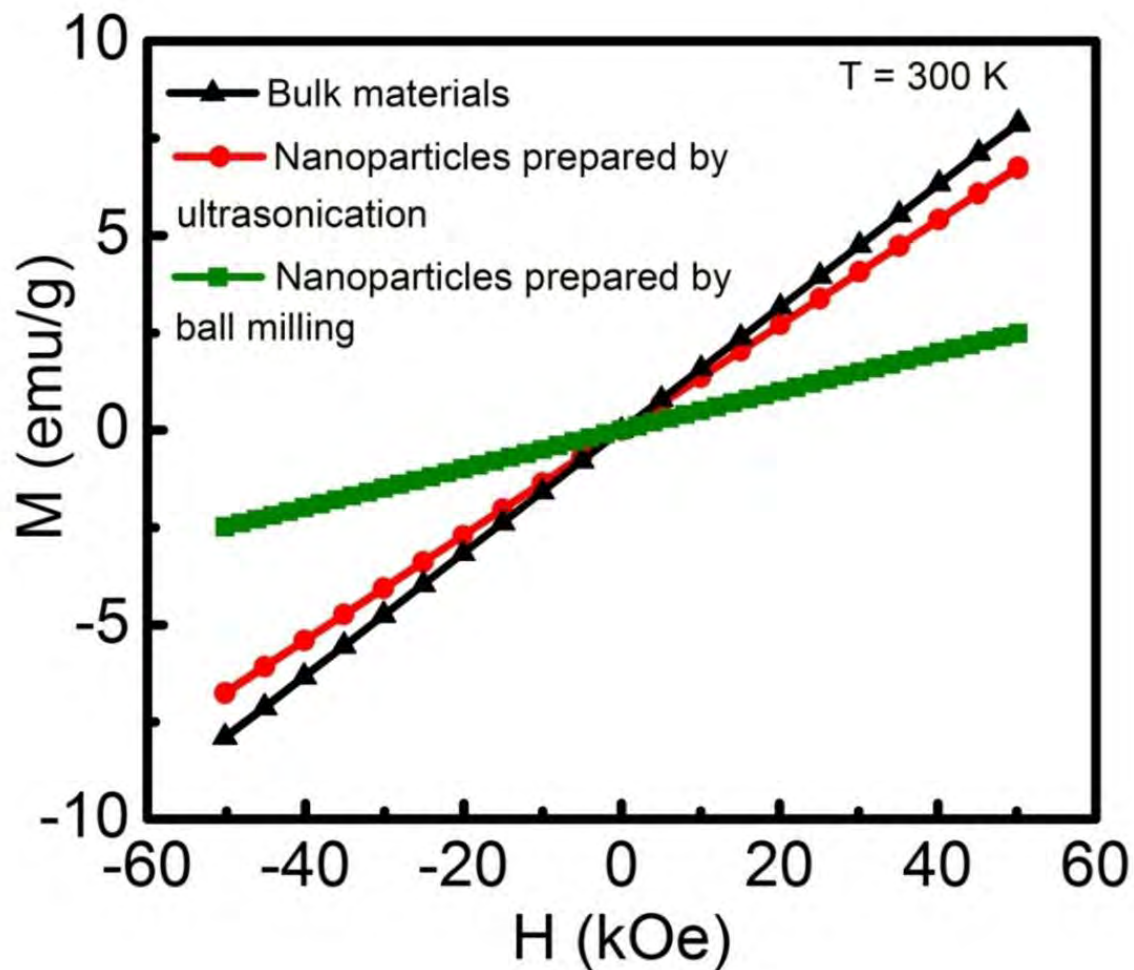
Figure 4.8: The room temperature M-H curves of $Gd_{0.7}Sr_{0.3}MnO_3$ (a) bulk materials, (b) nanoparticles prepared by ultrasonication and (c) ball milling techniques. The linear curves demonstrate the paramagnetic nature of bulk materials and corresponding nanoparticles at 300 K.

The coercive fields (Hc) can be quantified as $H_c = (H_{c1} - H_{c2})/2$ [14] where H_{c1} and H_{c2} are the left and right coercive fields, respectively. In this investigation, at 20 K, the H_c values are 1500 Oe for ultrasonically prepared nanoparticles and 910 Oe for the corresponding bulk materials (in figure 4.10) whereas the coercivity was zero at 300 K.
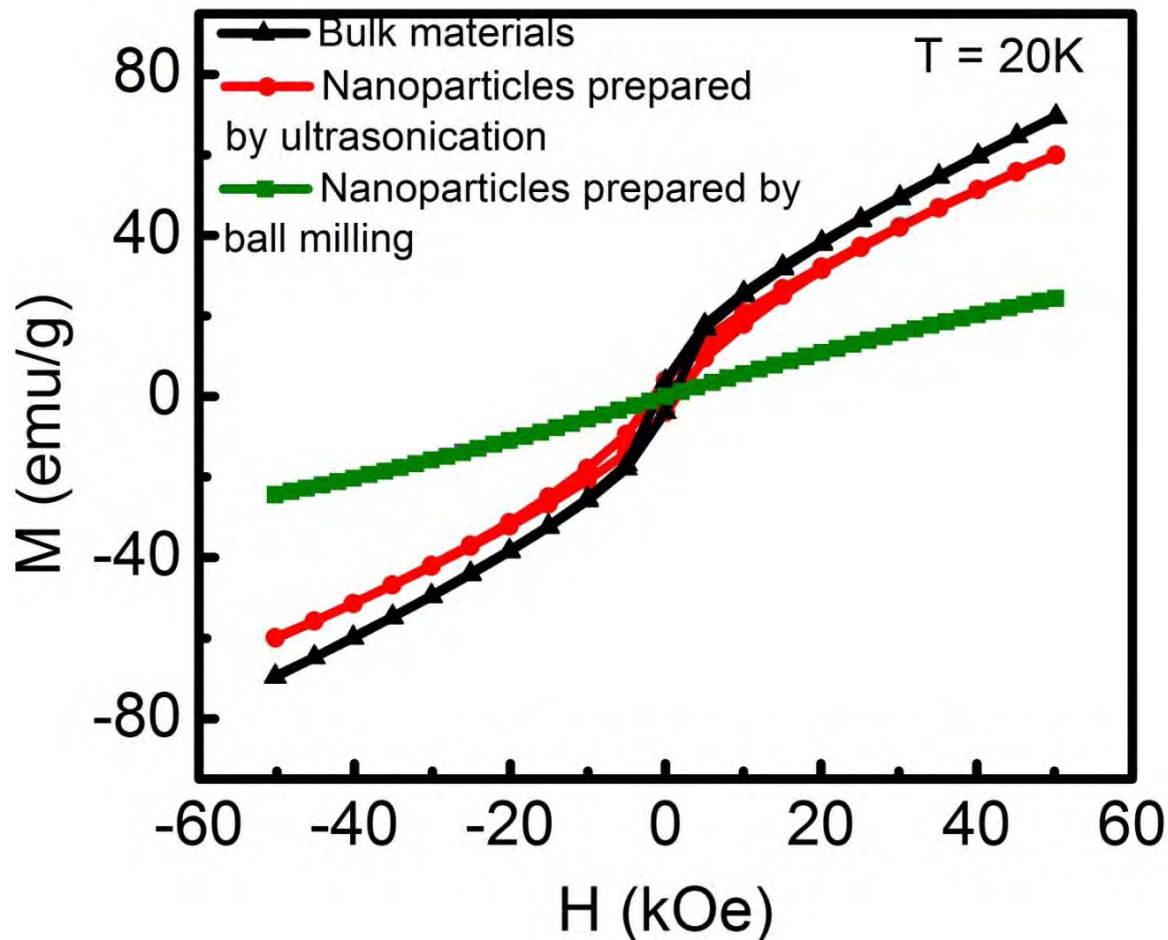
Figure 4.9: M-H hysteresis loop of $Gd_{0.7}Sr_{0.3}MnO_3$ (a) bulk materials, (b) nanoparticles prepared by ultrasonication and (c) ball milling techniques at 20 K.

In fact, the coercive fields are temperature dependent and increase with decreasing temperatures [15]. With decreasing particle size, the surface to volume ratio of the nanoparticles increases and the overall increase of surface anisotropy may cause coercivity enhancement [16]. It should be noted that, in the case of nanoparticles prepared by ball milling technique, the M-H curve was just a straight line with zero coercivity both at 20 K and 300 K.

It is worth mentioning that the nanoparticles of a similar class of $La_{0.8}Sr_{0.2}MnO_{3-\delta}$ [16] and $La_{0.7}Ca_{0.3}MnO_3$ [17] manganites were prepared by using high-energy ball milling started
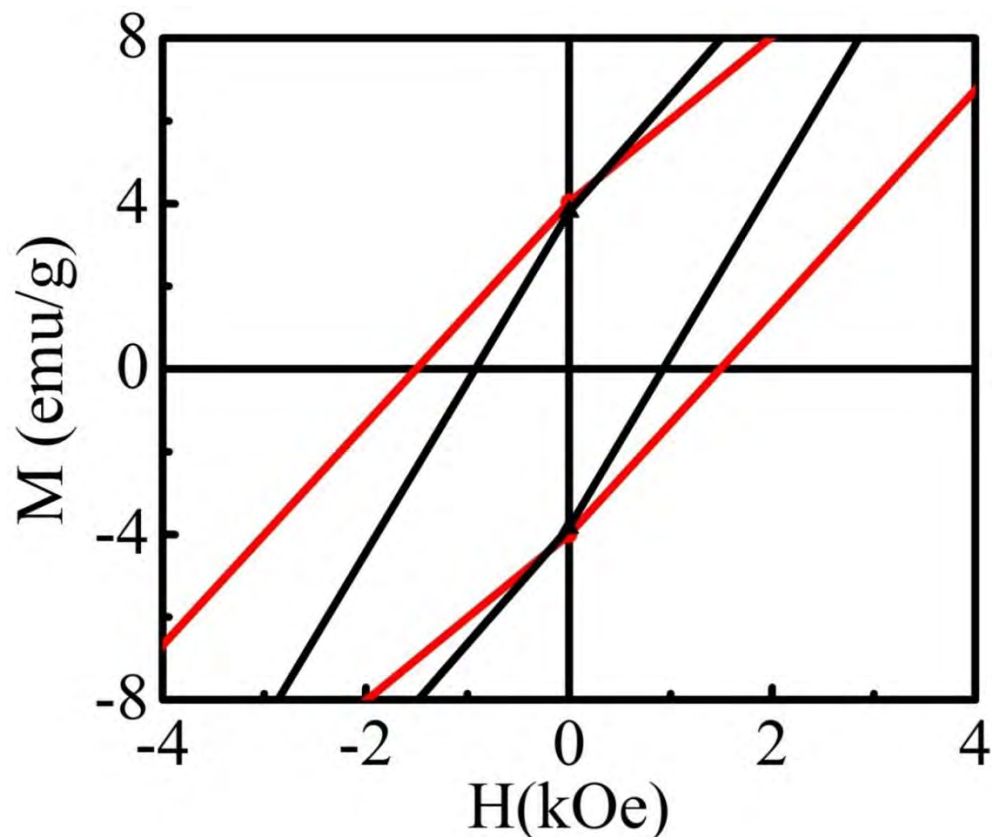
Figure 4.10:   An enlarged view of M-H hysteresis loops showing the enhancement of the coercivity of the ultrasonically synthesized nanoparticles (red line).

from bulk polycrystalline samples as were prepared in this investigation. The particle size was found to decrease with milling time. For a longer milling time (>8 hours), the particle size was reduced to around 12 nm measured from XRD pattern. However, the ferromagnetic to paramagnetic transition temperatures, i,e, T_c values of $La_{0.7}Ca_{0.3}MnO_3$ nanoparticles [17] were found to decrease compared than those of unmilled bulk polycrystalline powder materials [17]. Moreover, magnetization of the synthesized nanoparticles was decreased dramatically compared to the bulk polycrystalline samples [16, 17]. In the present investigation, instead of ball milling we did ultrasonication of micron-size powder materials for 60 minutes and we obtained nanoparticles of sizes ranging from 20-40 nm. Moreover, the transition temperatures of the ultrsonically synthesized nanoparticles and their bulk materials was same (35-40 K) as shown in figures 4.6 (a) and (b). The maximum magnetizations M_s of $Gd_{0.7}Sr_{0.3}MnO_3$ at 50 kOe

for bulk materials, nanoparticles prepared by ultrasonication and ball milling techniques were inserted in Table I.

TABLE I: The table shows the maximum magnetization Ms of $Gd_{0.7}Sr_{0.3}MnO_3$ at 50 kOe for bulk materials, nanoparticles prepared by ultrasonication and ball milling techniques.

T(K)	Maximum magnetization M_s (emu/g) at 50 kOe		
	Bulk materials	Nanoparticles prepared by ultrasonication	Nanoparticles prepared by ball milling
20	70 (emu/g)	60 (emu/g)	25 (emu/g)
300	7.8 (emu/g)	6.7 (emu/g)	2.5 (emu/g)

As shown in Table I, at 20 K, the maximum value of magnetization 70 emu/g at 50 kOe for bulk materials was reduced to 60 emu/g and 25 emu/g for ultrasonically prepared and ball milled nanoparticles, respectively. Hence, both at 20 K and 300 K, the net value of the magnetization of ultrasonically prepared nanoparticles was reduced compared to that of the bulk sample, however, here the reduction was nominal compared to the drastic decrease of magnetization for nanoparticles prepared by high energy ball milling. The reduction in magnetization is in good agreement with values reported in Refs. [16, 17] for manganite nanoparticles prepared also by high energy ball milling. The degradation of the magnetic properties of nanoparticles prepared by high energy ball milling than those of bulk materials and ultrasonically prepared nanoparticles might be associated with contamination and amorphization of the nanoparticles due to 12 hours ball milling. The dramatic decrease of the magnetization in nanoparticles prepared by ball milling may be also related with formation of the nonmagnetic layer [16] at the surface of the ball milled nanoparticles as was evident from HRTEM image, figure 4.3 (b).

References :

[1]   Garca-Landa, B., De Teresa, J. M. and Ibarra, M. R., Ritter, C., Drost, R., Lees, M. R., "Colossal magnetoresistance in $Gd_{1/2}Sr_{1/2}MnO_3$", J. App. Phys., 83, 7664, 1998.

[2]   Sagar, S., Ganesan, V., Joy, P. A., Senoy Thomas, Liebig, A., Albrecht, M. and Anantharaman, M. R., "Investigations on the Multiferroic and Thermoelectric properties of Low and Intermediate band width Manganites", EPL, 91, 17008, 2010.

[3]   Basith, M. A., Ngo, D. –T., Quader, A., Rahman, M. A., Sinha, B. L., Bashir Ahmmad, Fumihiko Hirose and Molhave, K., "Simple top-down preparation of magnetic $Bi_{0.9}Gd_{0.1}Fe_{1-x}TixO_3$ nanoparticles by ultrasonication of multiferroic bulk material", Nanoscale, 6, 14336, 2014.

[4]   Carver, J. C., Schweitzer, G. K., Carlson, T. A., "Use of X-Ray Photoelectron Spectroscopy to Study Bonding in Cr, Mn, Fe, and Co Compounds", J. Chem. Phys., 57, 973, 1972.

[5]   Fang, L. A., Liu, J. A., Ju, S. Zheng, F. G., Dong, W., Shen, M. R., "Experimental and theoretical evidence of enhanced ferromagnetism in sonochemical synthesized $BiFeO_3$ nanoparticles", Appl. Phys. Lett., 97, 242501, 2010.

[6]   Das, R., Sarkar, T. and Mandal, K., "Multiferroic properties of Ba^{2+} and Gd^{3+} co-doped bismuth ferrite: magnetic, ferroelectric and impedance spectroscopic analysis", J. Phys. D: Appl. Phys., 45, 45500212, 2012.

[7]   Elke Beyreuther, Stefan Grafstrm, Lukas, M., Eng, Christian Thiele and Kathrin Drr, "XPS investigation of Mn valence in lanthanum manganite thin films under variation of oxygen content", Phys. Rev. B, 73, 155425, 2006.

[8]   Dutta, D. P., Mandal, B. P., Mukadam, M. D., Yusuf, S. M., Tyagi, A. K., "Improved magnetic and ferroelectric properties of Sc and Ti co-doped multiferroic nano $BiFeO_3$ prepared via sonochemical synthesis", Dalton Trans., 43, 7838-7846, 2014.

[9]   Dutta, D. P., Mandal, B. P., Naik, R., Lawes, G., Tyagi, A. K., "Magnetic, Ferroelectrc and Magnetocapacitive Properties of Sonochemically Synthesized Sc-Doped $BiFeO_3$", J. Phys. Chem. C, 112, 2382-2389, 2013.

[10]   Wang, Z. L., Kang, Z. C., Functional and Smart Materials, Structural Evolution and Structure Analysis, Plenum Press, New York, Chapter 8, 441, 1998.

[11]   Coey, J. M. D., Viret, M., "Mixed-Valence manganites", Advances in Physics, 48, 2, 167, 1999.

[12]   Aditya, A. Wagh, Anil Kumar, P. S., Bhat, H. L. and Suja Elizabeth, "An investigation of first-order transition across charge ordered and ferromagnetic phases in $Gd_{0.5}Sr_{0.5}MnO_3$ single crystals by magnetic and magnetotransport studies", J. Phys.: Condens. Matter, 22, 2, 026005, 2010.

[13]   Terai, T., Sasaki, T., Kakeshita, T., Fukuda, T., Saburi, T., Kitagawa, H., Kindo, K., Honda, M., "Electronic and magnetic properties of $R_{0.5}A_{0.5}MnO_3$ Compounds (R=Gd, Dy, Ho, Er; A=Sr, Ca)", Phys. Rev. B, 61, 5, 3488-3493, 2000-I.

[14]   Basith, M. A., Khan, F. A., Bashir Ahmmad, Fumihiko Hirose, Ngo, D. –T., Tran, Q. H., and Molhave, "Tunable exchange bias effect in magnetic $Bi_{0.9}Gd_{0.1}Fe_{0.9}Ti_{0.1}O_3$ nanoparticles at temperatures up to 250 K", J. App. Phys., 118, 023901, 2015.

[15]   Zhou, J. P., McDevitt, J. T., Zhou, J. S. Yin, H. Q., Goodenough, J. B., Gim, Y. and Jia, Q. X., "Effect of tolerance factor and local distortion on magnetic properties of kkthe perovskite manganites", Appl. Phys. Lett., 75, 1146, 1999.

[16]   Roy, S., Dubenko, I., Edorh, D. D. and Ali, N. J., "Size induced variations in structural and magnetic properties of double exchange $La_{0.8}Sr_{0.2}MnO_{3-\delta}$ nano-ferromagnet", J. Appl. Phys., 96, 1202, 2004.

[17]   Phan, T.-L. , "An Effective Route to Prepare $La_{0.7}Ca_{0.3}MnO_3$Nanoparticles: Structural Characterization and Magnetic Properties", New Phys.: Sae Mulli, 63, 557–561, 2013.

CHAPTER 5

CONCLUSIONS

5.1 Conclusions

By using ultrasonication technique $Gd_{0.7}Sr_{0.3}MnO_3$ nanoparticles were produced directly from their bulk powder materials and the chemistry of the particles were likely unaltered. Hence, bulk and nanoparticle materials were directly compared in terms of magnetic properties than materials produced by two different synthesis techniques [1]. The nanoparticles were also synthesized by using high energy ball milling (milling time 12 hours) of bulk powder materials prepared by solid state reaction technique. The magnetization of the nanoparticles prepared by high energy ball milling was found to decrease drastically than those of ultrasonically prepared nanoparticles and their bulk materials. Compared to the high energy ball milling for a longer time, here sonication of bulk powder materials for 60 minutes produced rare-earth based manganite nanoparticles without altering their phase transition temperature. At low temperature, the coercivity of the nanoparticles produced by ultrasonication technique was enhanced than that of their bulk materials. We believe that the demonstrated ultrasonication technique may be promising for fabrication of other rare-earth based manganite nanoparticles and can be further developed as a versatile technique for the preparation of nanoparticles of a wide range of materials.

5.2 Future work

In the present investigation, the higher value of magnetization at 20 K (figure 4.9) compared than that at room temperature (figure 4.8) may be due to the ordering of heavy rare-earth ions like Gd^{3+} [2,3]. The paramagnetic contribution of the ions also play role to enhance magnetization at temperatures [4] and therefore, to know the exact alignment of spins and the magnetic contribution of Gd^{3+} further investigations are required. Magnetoresistance effect of this material system may be measured by applying a suitable magnetic field. Investigations may also be carried out on similar magnetic system like $(La, Nd)SrMnO_3$ manganites.

References:

[1]   Zhang, T., Wang, X. P. and Fang, Q. F., "Evolution of the Electronic Phase Separation with Magnetic Field in Bulk and Nanometer $Pr_{0.67}Ca_{0.33}MnO_3$ Particles", J. Phys. Chem. C, 115, 19482-19487, 2011.

[2]   Zhang, T., Wang, X. P., Fang, Q. F. and Li, X. G., "Magnetic and charge ordering in nanosized manganites", Applied Physics Reviews, 1, 031302, 2014.

[3]   Rao, S. S. and Bhat, S. V., "Preparation, Characterization, and Magnetic Studies of $Bi_{0.5}X_{0.5}(X = Ca, Sr)MnO_3$ Nanoparticles", J. Nanosci. Nanotechnol., 7, 2025–2028, 2007.

[4]   Wang, J., *et al*, "Epitaxial $BiFeO_3$ Multiferroic Thin Film Heterostructures", Science, 299, 1719, 2003.